IntechOpen

Laser Technology and its Applications

Edited by Yufei Ma

LASER TECHNOLOGY AND ITS APPLICATIONS

Edited by **Yufei Ma**

Laser Technology and its Applications
http://dx.doi.org/10.5772/intechopen.75224
Edited by Yufei Ma

Contributors

Simona Delia Nicoara, Yachen Gao, Degui Kong, Zhen Yang, Xin Yu, Jiangbo Peng, Jianlong Zhang, Amir Reza Sadrolhosseini, Babar Ibrahim Muhammad, Mingjun Chi, Ole Jensen, Anders Hansen, Paul Petersen

Notice

Statements and opinions expressed in the chapters are these of the individual contributors and not necessarily those of the editors or publisher. No responsibility is accepted for the accuracy of information contained in the published chapters. The publisher assumes no responsibility for any damage or injury to persons or property arising out of the use of any materials, instructions, methods or ideas contained in the book.

First published in London, United Kingdom, 2019 by IntechOpen
eBook (PDF) Published by IntechOpen, 2019
IntechOpen is the global imprint of INTECHOPEN LIMITED, registered in England and Wales, registration number: 11086078, The Shard, 25th floor, 32 London Bridge Street
London, SE19SG – United Kingdom
Printed in Croatia

British Library Cataloguing-in-Publication Data
A catalogue record for this book is available from the British Library

Additional hard and PDF copies can be obtained from orders@intechopen.com

Laser Technology and its Applications
Edited by Yufei Ma

p. cm.

Print ISBN 978-1-78984-917-2

Online ISBN 978-1-78984-918-9

eBook (PDF) ISBN 978-1-83881-817-3

Meet the editor

Yufei Ma received his PhD degree in Physical Electronics from the Harbin Institute of Technology, China, in 2013. From September 2010 to September 2011 he spent time as a visiting scholar at Rice University, USA. Currently, he is an associate professor at the Harbin Institute of Technology, China. His research interests include optical sensors, trace gas detection, laser spectroscopy, and optoelectronics. Up to now he has published more than 100 peer-reviewed papers. He has served as an academic editor for two SCI-indexed journals.

Contents

Preface

The laser has become more and more important in scientific research and industrial applications with the merits of excellent monochromaticity, coherence, and directivity. Now, the laser wavelength can cover the range from ultraviolet to terahertz and output laser performance has significantly progressed in recent years. Therefore, due to the characteristics of non-invasiveness and high-power intensity, applications based on laser techniques have become more extensive. The aim of this book is to introduce and present the latest advancements in the field of laser techniques and their applications.

In this book, two chapters are focused on the advanced diode laser and fiber laser. A high-power tunable GaN diode laser using external-cavity configuration with emission in the visible spectral range is shown first. Subsequently, a thulium–ytterbium short pulse fiber laser by cladding pumping is reported. In the application section, there are four chapters on laser ablation, laser-introduced fluorescence, laser treatment, and nonlinear optical response of nanoparticles.

Yufei Ma
Harbin Institute of Technology
China

Section 1

Laser Technology

Chapter 1

Tunable High-Power External-Cavity GaN Diode Laser Systems in the Visible Spectral Range

Mingjun Chi, Ole Bjarlin Jensen,
Anders Kragh Hansen and Paul Michael Petersen

Additional information is available at the end of the chapter

http://dx.doi.org/10.5772/intechopen.79703

Abstract

In this chapter, both blue and green high-power tunable diode laser systems based on GaN broad-area diode laser (BAL) in Littrow external cavity are demonstrated. For blue diode laser system, for high-power application, an output power around 530 mW over a 1.4 nm tunable range is obtained; for wide tunable range application, an output power around 80 mW over a 6.0 nm tunable range is obtained. For the green diode laser system, for high-power application, an output power around 480 mW with a tunable range of 2.1 nm is achieved; for wide tunable range application, an output power of 50 mW with a tunable range of 9.2 nm is achieved. The tuning range and output power optimization of an external-cavity diode laser system is investigated based on the experimental results obtained in the blue and green external-cavity GaN diode laser systems. The obtained results can be used as a guide for selecting gratings for external-cavity diode lasers for different requirements. The temporal dynamics of the green diode laser system is studied experimentally, and pulse package oscillation is observed, for the first time to our knowledge, in a BAL with an external-cavity grating feedback.

Keywords: diode lasers, GaN, external cavity, tunable, instabilities and chaos

1. Introduction

Since the first demonstration of a room temperature continuous wave (CW) GaN violet diode laser by Nakamura et al. [1], great progress has been achieved on the GaN-based diode lasers in the violet to green spectral range. Nowadays, high-power GaN diode lasers with CW output power of a few watts are commercially available in the blue to green spectral range [2].

The spectral bandwidth of the high-power devices is around 1.0 nm, and the devices are not tunable. Although single longitudinal mode GaN diode laser around 405 nm has been achieved with the laterally coupled distributed feedback (DFB) technique [3]; this technique is under development and not available for commercial devices, especially not available for high-power GaN diode lasers.

Tunable, high-power, narrow spectral bandwidth light sources based on semiconductor lasers from the violet to green spectral range are attractive for many applications, such as high-resolution spectroscopy, holographic data storage, laser cooling, laser holographic display, biophotonics and as pump sources for nonlinear frequency conversion and for titanium-sapphire lasers [4–10]. The broad emission bandwidth limits the usage of the high-power GaN diode lasers in some of these applications. There are two main techniques to achieve high-power, narrow-bandwidth blue and green laser emission based on semiconductor devices. The first one is based on nonlinear frequency conversion, including second harmonic generation and sum frequency generation of GaAs lasers emitting from 800 to 1100 nm [11, 12]. The second approach is external-cavity feedback technique used to improve the spectral quality of the high-power GaN diode lasers and make the lasers tunable [13, 14]. The laser systems developed based on the first method are relatively complex, and the laser systems are not tunable, or the tunable range is narrow. Thus, the second approach is applied in this chapter to achieve narrow bandwidth, tunable blue and green diode laser systems.

In this chapter, we first demonstrate two tunable, narrow bandwidth high-power GaN diode laser systems; one system is emitting around 455 nm in the blue spectral region, the other is emitting around 515 nm in the green spectral region. Secondly, the tuning range and output power optimization of an external-cavity diode laser (ECDL) system is investigated based on the experimental results. Finally, the dynamics of the green external-cavity diode laser system is studied.

2. Experimental setup

The experimental setup for the Littrow external-cavity feedback system is schematically shown in **Figure 1**. The high-power GaN diode lasers (2 W for blue or 1 W for green devices) used in our experiment are broad-area diode lasers. The laser beam is TE-polarized for both devices. The laser beam emitted from the front facet is collimated by an aspherical lens of 4.0 mm focal length with a numerical aperture of 0.6. The collimated beam is incident on a bulk diffraction grating mounted in Littrow configuration and oriented with the lines in the grating parallel to the slow axis of the diode laser.

The first-order diffracted beam from the grating is the feedback beam, thus the external cavity is formed between the diode laser and the grating. A beam splitter is inserted in the external cavity and reflects part of the beam as a diagnostic beam in which the spectral bandwidth and tunability of the laser system are measured. The zeroth-order diffracted beam of the grating is the output beam of the ECDL system, and a power meter is used to record the power of the output beam. The ECDL system is tuned by rotating the grating along the groove direction.

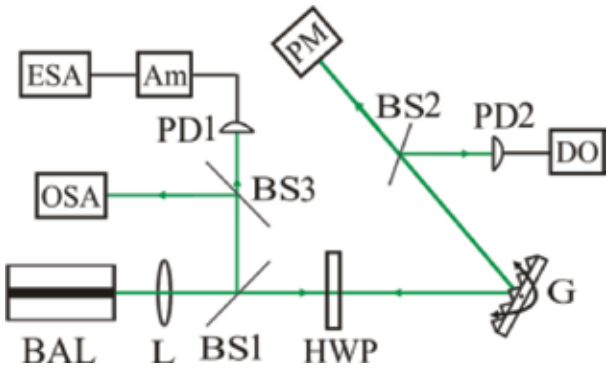

Figure 1. Experimental setup of the ECDL system. BAL, broad-area diode laser; L, lens; BS1, BS2 and BS3, beam splitter; HWP, half-wave plate; G, bulk grating, PD1 and PD2, photodiode; DO, digital oscilloscope; OSA, optical spectrum analyzer; Am, amplifier; ESA, electrical spectrum analyzer; PM, power meter.

3. Experimental results

3.1. Blue GaN external-cavity diode laser system

In this subsection, the results of blue ECDL system are presented [15]. Two bulk diffraction gratings are used in the blue ECDL system, one is a holographic diffraction grating with a groove density of 2400 lines/mm (Thorlabs, GH13-24 U), and the zeroth- and first-order diffraction efficiencies are 78.8 and 8.3%. The other is a ruled diffraction grating that is ruled with 1800 lines/mm and has a blaze wavelength of 500 nm (Thorlabs, GR13-1850), the zeroth- and first-order diffraction efficiencies are 29.6 and 53.5%, respectively. The length of the external cavity is around 110 mm.

In the freely running condition, the threshold current of the laser device is around 0.12 A, and the slope efficiency is around 1.62 W/A. With an injected current of 1.4 A, a 2 W output power is obtained. The diode laser is operating in multiple Fabry-Perot (FP) modes. The spectrum is centered around 456 nm with a spectral bandwidth around 1.2 nm. The longitudinal mode spacing of the FP modes is around 28.5 pm.

The blue ECDL system is characterized by measuring the spectrum at different wavelengths with these two different gratings. **Figure 2** shows the spectra of the blue ECDL system with an output power around 85 mW for both gratings. For the ECDL system with the holographic diffraction grating at an injected current of 0.2 A, **Figure 2(a)** shows seven normalized spectra from 453.4 to 456.5 nm. The bandwidth of the spectrum (FWHM) is around 9 pm in the 3.1 nm tunable range; it is much less than the 28.5 pm mode space of the FP laser resonator; this means the laser is forced to operate in a single longitudinal FP mode by the external feedback. **Figure 2(b)** shows eight normalized spectra from 452.8 to 458.8 nm for the ECDL system with the ruled diffraction grating at an injected current of 0.3 A. The spectral bandwidth is less than 20 pm for wavelengths longer than 456 nm in the 6.0 nm tunable range; for shorter wavelengths, the spectral bandwidth is less than 42 pm, that is, two FP modes oscillate simultaneously. The amplified spontaneous emission (ASE) is more than 20 dB suppressed in the tunable ranges for both diffraction gratings.

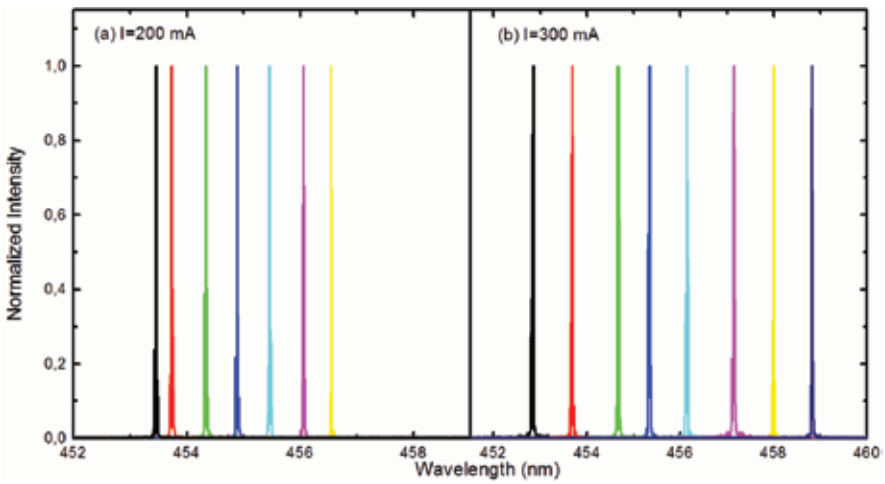

Figure 2. Optical spectra of the output beam from the blue ECDL system with (a) a holographic grating and (b) a ruled grating. The output power is around 85 mW.

Figure 3 shows the spectra of the blue ECDL system with an output power around 200 mW with both gratings. **Figure 3(a)** shows seven normalized spectra from 453.7 to 456.5 nm with the holographic grating, at an injected current of 0.3 A. The spectral bandwidth is around 35 pm in the tunable range, that is, two FP modes oscillate simultaneously. **Figure 3(b)** shows the normalized spectra of the ECDL from 453.5 to 459.0 nm with the ruled grating, the injected current is 0.6 A. The bandwidth is less than 67 pm in the tunable range. The ASE suppression is more than 24 dB for the holographic grating feedback and more than 17 dB for the ruled grating feedback.

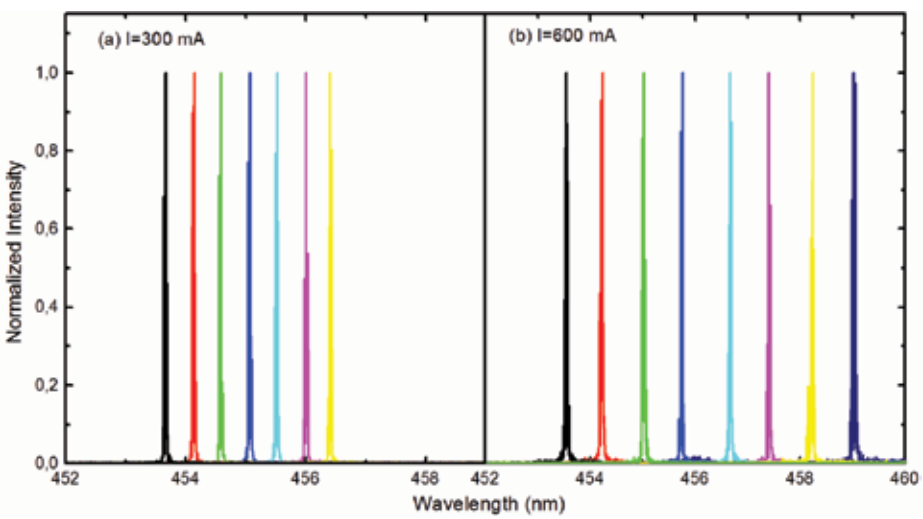

Figure 3. Optical spectra of the output beam from the blue ECDL system with (a) a holographic grating and (b) a ruled grating. The output power is around 200 mW.

Figure 4 shows the spectra of the blue ECDL system with an output power around 350 mW. The laser system is tunable from 454.1 to 456.5 nm for the holographic grating feedback. The bandwidth is around 35 pm in the tunable range, and the ASE is more than 24 dB suppressed. The laser system is tunable from 455.3 to 459.4 nm for the ruled grating feedback; the ASE is more than 18 dB suppressed. The bandwidth (FWHM) is less than 70 pm in the tunable range, but side peaks appear in some spectra as shown in **Figure 4(b)**.

With the ruled grating, a further increase of the current increases the spectral bandwidth to a few hundred picometers, and two peaks are present in the spectrum. With the holographic grating, the current can be increased to 0.6 A, where the diode laser is tuned from 455.0 to 456.4 nm with an output power of around 530 mW. The bandwidth is around 63 pm in the tunable range, and the ASE is more than 20 dB suppressed. Further increase of the current also increases the bandwidth to a few hundred picometers for the ECDL with the holographic grating.

The output power of the blue ECDL system at different wavelengths is shown in **Figure 5** with these two different gratings. When the holographic grating is applied, the maximum output powers are 85, 198, 368 and 531 mW with injected current of 0.2, 0.3, 0.45 and 0.6 A, respectively. When the ruled grating is applied, the maximum output powers are 90, 222, and 340 mW with injected current of 0.3, 0.6 and 0.9 A, respectively. For both gratings, the output power is relatively constant in the tunable range at each injected current. With the highest output power of the ECDL, that is, 531 mW for the holographic grating feedback and 340 mW for the ruled grating feedback, around 68 and 27% of the output power of the freely running laser are extracted in the ECDL system for the two gratings, respectively. Thus, the efficiency of the ECDL with the holographic grating is much higher than that of the ECDL with the ruled grating. The reason is the higher first-order diffraction efficiency of the ruled grating (53.5%) limits the output power.

The tunable range of the blue ECDL system with the ruled grating is much broader than that of the blue ECDL system with the holographic grating when the output power of the diode

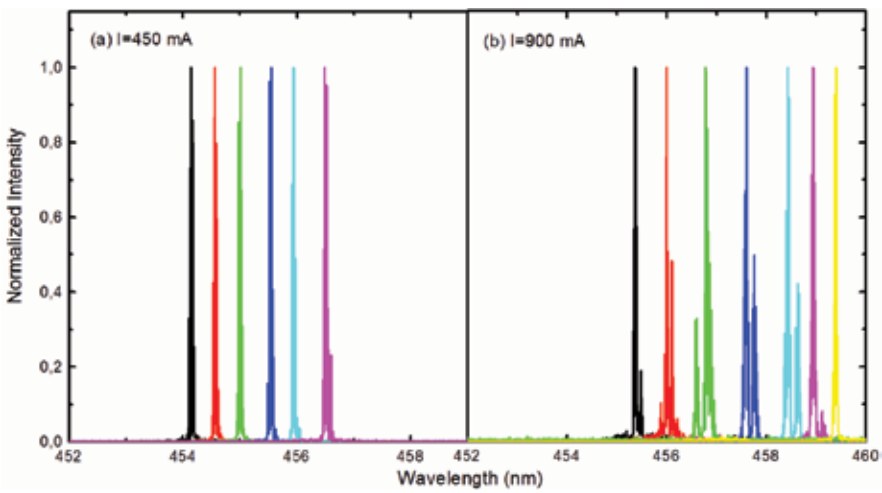

Figure 4. Optical spectra of the output beam from the ECDL system with (a) a holographic grating at an injected current of 0.45 A and (b) a ruled grating at an injected current of 0.9 A.

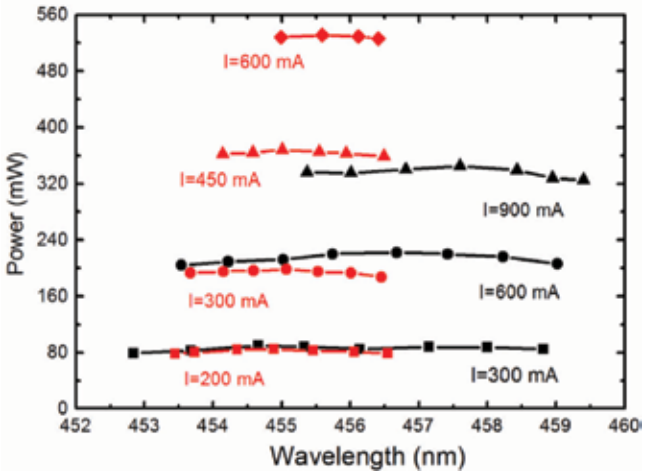

Figure 5. Output power of the blue ECDL at different wavelengths and operating currents with the holographic grating (red signs) and the ruled grating (black signs).

laser system is comparable. The reason is that the first-order diffraction efficiency of the ruled grating is much higher compared with that of the holographic grating, that is, 53.5 versus 8.3%. The higher the feedback strength from the grating, the more effective the suppression of the freely running lasing modes.

In summary, a high-power, tunable, narrow-bandwidth ECDL system based on a GaN diode laser around 455 nm is demonstrated. The laser system can be tuned over 1.4 nm with an output power around 530 mW when the holographic grating is applied; the laser system can be tuned over 6.0 nm with an output power of 80 mW when the ruled grating is applied. The results show the efficiency of the ECDL with holographic grating is higher, but the tunable range of the ECDL with ruled grating is broader.

3.2. Green GaN external-cavity diode laser system

In this subsection, the results of a green ECDL system are presented [16]. For the green ECDL system, only the holographic grating (Thorlabs, GH13-24 U) is applied. A half-wave plate is inserted in the external cavity to turn the polarization direction of the laser beam. Thus, the green laser system can be operated in both *s*-polarized mode (the laser beam is polarized along the lines of the grating) and *p*-polarized mode (the laser beam is polarized perpendicular to the lines of the grating). The zeroth- and first-order diffraction efficiencies of the grating are around 81 and 7% for the *s*-polarized beam, and around 48 and 29% for the *p*-polarized beam, respectively. The length of the external cavity of the laser system is around 140 mm, corresponding to a 0.95 pm external-cavity mode spacing.

The threshold current of the freely running green diode laser is around 0.25 A, and the slope efficiency is around 1.0 W/A. With an injected current of 1.4 A, 1.1 W output power is obtained. The laser diode is operating in multiple FP modes centered around 515 nm, with a spectral bandwidth of 1.3 nm. The mode spacing of the FP modes is around 39 pm.

The tunability of the green ECDL system operated in both *s*- and *p*-polarized modes is characterized by measuring the optical spectrum of the output beam at different wavelengths. The spectra of the ECDL for both operating modes with an operating current of 330 mA are shown in **Figure 6**. The output power of the green ECDL system for the *s*-polarized and *p*-polarized mode operation are around 70 and 50 mW, respectively. **Figure 6(a)** shows eight normalized spectra from 511.1 to 516.0 nm for *s*-polarized mode operation. The spectral bandwidths of these spectra are around 8 pm. Compared with the 39 pm mode spacing of the FP modes, the ECDL in the *s*-polarized mode operates in single FP mode. **Figure 6(b)** shows 10 spectra from 508.8 to 518 nm for *p*-polarized mode operation. The bandwidth is less than 9 pm in the tunable range. The ASE is more than 15 and 17 dB suppressed for *s*- and *p*-polarized mode operation, respectively.

Figure 7 shows the optical spectra of the green ECDL system for both operation modes with the output power around 290 mW. To achieve the 290 mW output power, 600 and 850 mA injected currents are needed for *s*- and *p*-polarized mode operation, respectively. Six normalized spectra from 513.1 to 515.7 nm are shown in **Figure 7(a)** for *s*-polarized mode operation. Two peaks are observed in the spectra and the spectral bandwidth is less than 0.25 nm. Five spectra from 512.9 to 517.5 nm are shown in **Figure 7(b)** for *p*-polarized mode operation. The spectral bandwidth (FWHM) is less than 50 pm in the tunable range, however side modes appear in the spectra. The ASE is more than 15 dB suppressed in the tunable ranges for both *s*- and *p*-polarized mode operation. In the *s*-polarized mode, the injected current can be further increased to 850 mA, and the output power is increased to 480 mW. The ECDL system can be tuned from 514.1 to 516.2 nm, the emission bandwidth is less than 0.5 nm in the tunable range, and the ASE is more than 15 dB suppressed.

Figure 8 shows the output power of the ECDL system at different wavelengths and injected currents for both operating modes. In the *s*-polarized mode, the maximum output powers

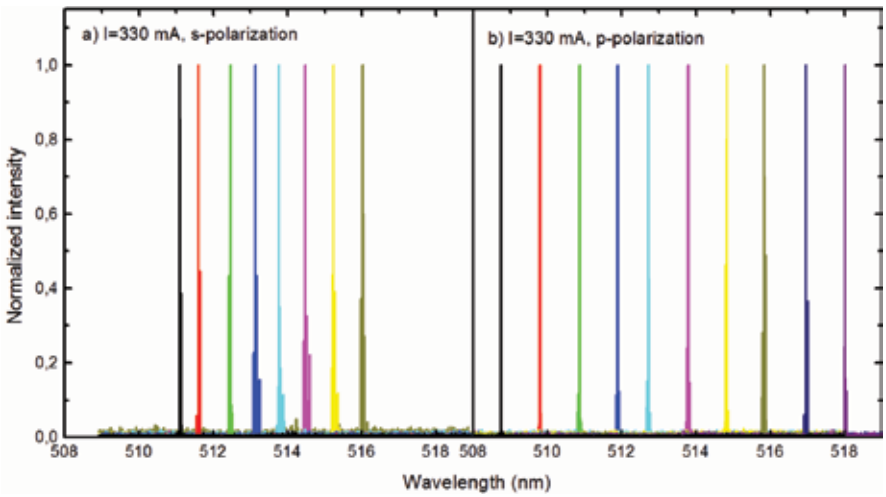

Figure 6. Optical spectra of green ECDL system operates in (a) *s*-polarized mode and (b) *p*-polarized mode. The injected current is 330 mA for both conditions.

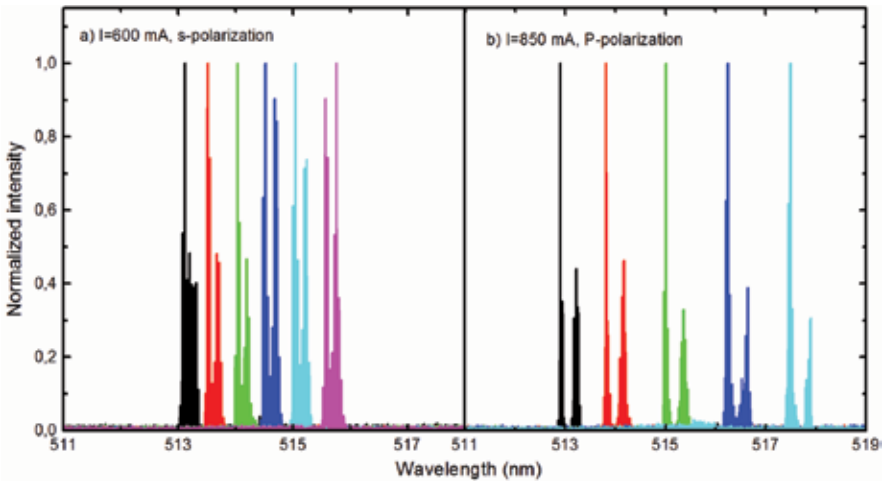

Figure 7. Optical spectra of the green ECDL system operates in (a) *s*-polarized mode and (b) *p*-polarized mode. The output power is around 290 mW for both operation modes.

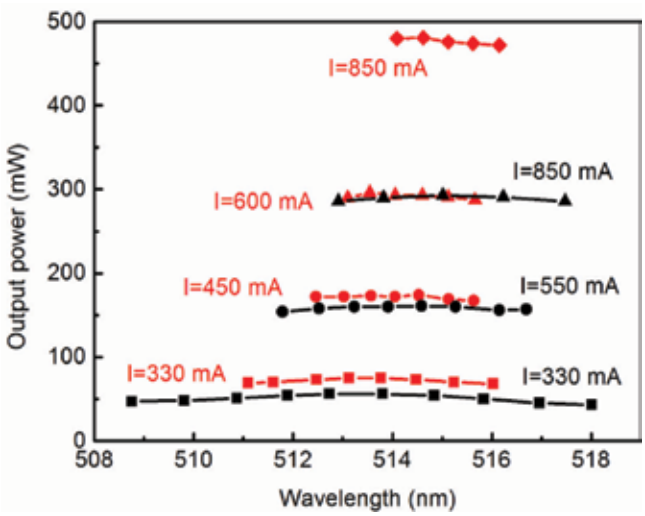

Figure 8. Output power of the ECDL at different wavelengths and operating currents, operated in *s*-polarized mode (red signs) and *p*-polarized mode (black signs).

of the ECDL are 75, 173, 296 and 481 mW with injected current of 330, 450, 600 and 850 mA, respectively. In the *p*-polarized mode, the maximum output powers are 56, 161 and 293 mW with injected current of 330, 550 and 850 mA, respectively. The output power is relatively constant in the tunable range at each injected current for both operating modes.

With the highest injected current, that is, 850 mA, the maximum output powers for the *s*- and *p*-polarized mode operation are 481 and 293 mW. This means that 75 and 46% of the output power in freely running condition is extracted in the ECDL system for the *s*- and *p*-polarized

mode operation. However, **Figure 8** shows the tunable range of the ECDL in *p*-polarized mode operation is much broader than that of the ECDL in the *s*-polarized mode operation. The main reason for this difference is the higher zeroth-order diffractive efficiency of the holographic grating for the *s*-polarized beam compared with that for the *p*-polarized beam, that is, 81 versus 48%. The higher zeroth-order diffraction efficiency of the grating for *s*-polarized beam means a high output coupling efficiency, that is, high output power. However, the first-order diffractive efficiency for the *p*-polarized beam is much higher than that for the *s*-polarized beam, that is, 29 versus 7%. The higher the feedback strength from the grating (the higher first-order diffraction efficiency), the more effective the suppression of the freely running lasing mode, thus the tunable range of the green ECDL system operated in the *p*-polarized mode is broader.

In summary, a high-power, tunable, narrow-bandwidth ECDL system based on a GaN device around 515 nm is demonstrated. The laser system can be tuned over 2.1 nm with an output power around 480 mW in the *s*-polarized mode operation; the laser system can be tuned over 9.0 nm with an output power of 50 mW in the *p*-polarized mode operation. We can choose different operating modes for different priorities, that is, high-power or broad tuning range, using only one ECDL system.

3.3. Selection of diffraction grating for ECDL

Both the blue and green tunable ECDL systems show the efficiency (output power) of the ECDL system is higher when the zeroth-order diffraction efficiency of the grating used in the laser system is higher, such as the conditions for the holographic grating in the blue diode laser system and the *s*-polarized mode operation for the green diode laser system. However, the tunable range of the ECDL system with higher efficiency is narrower since a higher first-order diffraction efficiency of the grating is needed to achieve a wider tunable range. Thus, there is a compromise between the output power and the tunable range of the ECDL system since the sum of the zeroth- and first-order diffraction efficiencies is around unity.

To understand this compromise between the efficiency (output power) and tunable range further, a theoretical analysis is given below based on rate equations of the diode laser. The rate equations describing the carrier density N and the photon density N_{ph} in the diode laser cavity are given as [15, 17]:

$$\frac{dN}{dt} = \frac{\eta_i j}{qd} - \frac{N}{\tau} - v_{gr} g(N) N_{ph}, \tag{1}$$

$$\frac{dN_{ph}}{dt} = v_{gr} \Gamma g(N) N_{ph} - \frac{N_{ph}}{\tau_{ph}} + \alpha_m v_{gr} K N_{ph}(t - t_0), \tag{2}$$

where j is the inject current density, η_i is the internal efficiency, q is the elementary charge of an electron, d is the thickness of the active region, τ is the carrier lifetime, v_{gr} is the group velocity of the photons, $g(N)$ is the material gain, Γ is the confinement factor, τ_{ph} is the photon lifetime, α_m is the mirror loss, K is the feedback strength of the grating (the first-order diffraction efficiency in our case, here the other loss in the cavity is neglected.), t_0 is the time delay of

the external cavity. In particular $1/\tau_{ph} = v_{gr}(\alpha_i + \alpha_m)$, where α_i is the internal loss; and the gain $g(N) = g_N(N-N_{tr})$, g_N is the differential gain coefficient and N_{tr} is the transparency carrier density. When the diode laser system is steady-state operated, rearrange Eqs. (1) and (2), we obtain:

$$dN/dt = \eta_i j/qd - N/\tau - v_{gr} g_N (N - N_{tr}) N_{ph}, \tag{3}$$

$$dN_{ph}/dt = v_{gr} \Gamma g_N (N - N_{tr}) N_{ph} - v_{gr}[\alpha_i + (1 - K)\alpha_m] N_{ph}. \tag{4}$$

Eq. (4) shows the effect of the feedback is to reduce the mirror loss from α_m to $(1-K)\alpha_m$.

The steady-state solution of Eqs. (3) and (4) can be obtained as:

$$N = N_{tr} + \frac{1}{\Gamma g_N \tau_{ph} v_{gr}} - \frac{K\alpha_m}{\Gamma g_N} = N_{th}(0) - \frac{K\alpha_m}{\Gamma g_N}, \tag{5}$$

$$N_{ph} = \frac{\eta_i \Gamma \tau_{ph}}{qd}[j - j_{th}(K)] \frac{1}{1 - K\alpha_m/(\alpha_i + \alpha_m)}, \tag{6}$$

$$j_{th}(K) = j_{th}(0) - qdK\alpha_m/\eta_i \tau \Gamma g_N, \tag{7}$$

where $N_{th}(0)$ is the threshold carrier density without feedback, and $j_{th}(0) = qdN_{th}(0)/\eta_i\tau$ is the threshold current density without feedback. Eq. (7) shows the threshold current density $j_{th}(K)$ is decreased with the feedback strength K. Eq. (6) shows the photon density increases with K.

In our experiment, when we rotate the grating further to operate the laser system outside of the tunable ranges, the freely running emission appears and dominates the laser output, this means the competition of the freely running lasing at the gain center λ_0 and the lasing at wavelength λ (with a distance from the gain center) with feedback determines the tunable range of the external-cavity diode laser system. **Figure 9** shows a schematic diagram of the gain and the threshold of the diode laser system; the grating feedback profile is also shown. The grating feedback decreases the threshold current density at λ from $j_{th}(\lambda, 0)$ to $j_{th}(\lambda, K)$. When $j_{th}(\lambda, K)$ is less than the freely running threshold current density at λ_0, that is, $j_{th}(\lambda_0, 0)$, the laser system lases at λ, and vice versa. Since the decrease of the threshold current density by the feedback is proportional to K, a higher value of K causes a wider tunable range of the external-cavity diode laser system.

The output power P of an external-cavity diode laser system can be expressed as:

$$P \propto N_{ph}(1 - K) = \frac{\eta_i \Gamma \tau_{ph}}{qd}[j - j_{th}(K)] \frac{1 - K}{1 - K\alpha_m/(\alpha_i + \alpha_m)}. \tag{8}$$

The slope efficiency of the laser system decreases with the feedback strength K due to the last term in Eq. (8). Thus, the output power decreases with K, when the laser system is operated far above the threshold; although the threshold of the laser system also decreases with the feedback strength K.

http://dx.doi.org/10.5772/intechopen.79703

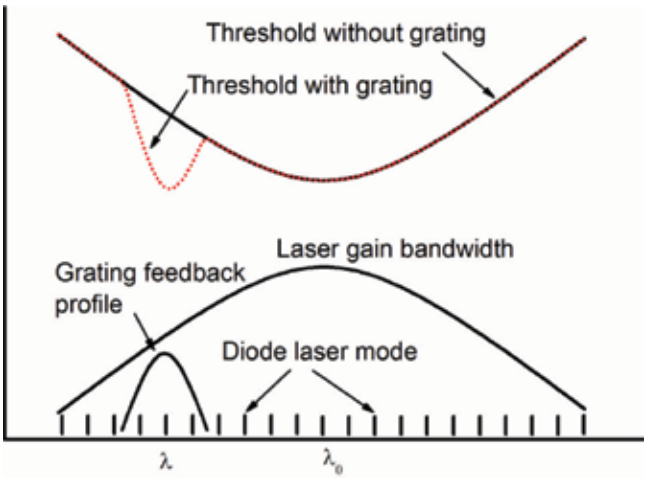

Figure 9. Schematic diagram of the gain and threshold with and without grating feedback. The grating feedback profile is also shown.

The theoretical analysis above mentioned is in agreement with our experimental results obtained from the blue and green ECDL systems; where the green laser system in *p*-polarized mode (high first-order diffraction efficiency) has a much wider tunable range but less output power compared with the laser system in *s*-polarized mode (low first-order diffraction efficiency). The experimental results in Refs. [18, 19] also show that wider tunable ranges and low output powers of the ECDLs were achieved with gratings with higher first-order diffraction efficiencies. From both the theoretical and experimental results, we can conclude that the compromise between the output power and the tunable range of an ECDL is a general condition and irrelevant to the geometry of the external cavity.

Considering the results obtained from the blue ECDL system using two different diffraction gratings, the ECDL system with the holographic grating has a narrower spectral bandwidth and a larger suppression of ASE when the output power of the ECDL with the two gratings are comparable. We believe the reason is that the holographic grating has a larger groove density compared with ruled grating, that is, 2400 lines/mm for the holographic grating versus 1800 lines/mm for the ruled grating, meaning that the holographic grating has a higher spectral resolution.

Both the experimental results and the theoretical analysis here provide a general guide to the selection of gratings for ECDL systems. Two main parameters of a diffraction grating are considered when a grating is used to build an ECDL system: the groove density and the first-order diffraction efficiency. A grating with a larger groove density leads to a narrower spectral bandwidth and a higher suppression of ASE compared with a grating with a small groove density. If a higher output power of a laser system is prioritized, a grating with a lower first-order diffraction efficiency should be selected. If a wider tunable range of a laser system is the high priority, a grating with a higher first-order diffraction efficiency should be selected. Thus, there is a compromise between the output power and the tuning range of an ECDL system. This is the main consideration for selecting a diffraction grating to build an ECDL system.

3.4. Dynamics of the green ECDL system

When external-cavity feedback is applied to a diode laser, complex temporal dynamics may take place [20, 21]. Thus, it is important for us to investigate the dynamics of the developed visible ECDL systems based on the GaN devices. In this subsection, we study the dynamic behaviors of the green ECDL system operated in *p*-polarized mode [22].

The complex dynamic behaviors have been studied intensively for both narrow-stripe diode lasers [23–26] and BALs [27–36] with external feedback. The dynamics of BALs have been investigated with short-cavity feedback [27–29], long-cavity feedback [30–32], tilt mirror feedback [33, 34] and lateral-mode-selected feedback [35, 36]. The feedback elements include ordinary mirrors [29–34], phase-conjugate mirrors [30] and spatially filtered mirrors [27, 28, 35, 36]. Different dynamic behaviors, such as low-frequency fluctuations (LFFs) [30, 31], self-pulsation [35], periodic oscillations [33, 36], pulse package oscillation (PPO) [28, 29, 36] and chaos [32], have been observed in the BALs with different external feedback. External grating feedback is widely used to achieve tunable high-power BAL systems [13–16]. However, the dynamics of such systems have only been studied in a very few cases [37].

As shown in **Figure 1**, the beam splitter, BS1, inserted in the external cavity reflects part of the beam to a silicon PIN photodiode, PD1, after a high-frequency amplifier; the amplified electronic signal is sent to an electrical spectrum analyzer to measure the intensity noise spectrum. The second beam splitter, BS2, reflects part of the output beam to the second photodiode, PD2, and a digital oscilloscope is used to measure the time series of the generated electronic signal. Since the green ECDL system is operated in *p*-polarized mode, the first-order diffraction efficiency is around 29%. Assuming a coupling efficiency of the feedback beam into the laser cavity is 50%, the feedback strength is around 14.5%, a moderate feedback strength for BALs [29, 35]. The physical length of the external cavity is around 33 cm.

The threshold current of the BAL is decreased from 250 to 205.5 mA by the external grating feedback. The wavelength is around 511.9 nm. We keep the feedback grating untouched during the experiment, meaning both the length of the external cavity and the wavelength of the green ECDL system are unchanged.

We investigate the dynamic behaviors of the green ECDL system by increasing the injected current from just above the threshold to more than two times threshold. **Figure 10(a)** shows the time series of the output beam with an operating current of 206.9 mA; a low-frequency periodic oscillation with a period around 220 ns is observed. The inset of **Figure 10(a)** shows the details of the time series in short time scale, an oscillation with a period around 2.4 ns is observed, the period of this oscillation is equal to the external-cavity delay time. This high-frequency oscillation is named as external-cavity oscillation with single-round-trip external-cavity frequency ν_{EC} [28, 35]. **Figure 10(b)** shows the intensity noise spectrum of the output beam. Besides the peak at ν_{EC}, a peak round 4.5 MHz and its harmonics for the low-frequency oscillation (LFO) shown in **Figure 10(a)**, ν_{LFO}, are observed. Additionally, some peaks around ν_{EC} with the frequency difference of ν_{LFO} are also visible. **Figure 10** shows that the output of the green ECDL manifests a typical dynamic state named regular PPO, which mainly takes place in short cavity feedback condition [28, 29], where the external-cavity loop oscillation is modulated by a periodic LFO.

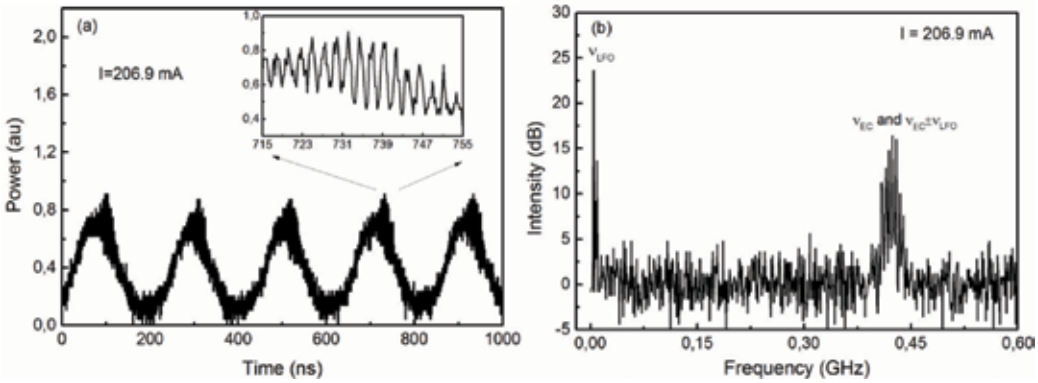

Figure 10. (a) Time series and (b) intensity noise spectrum of the output beam from the green ECDL system with an operating current of 206.9 mA. The inset in (a) shows a close-up of the peak of one of the pulse packages.

Figure 11 shows the time series of the output beam of the green ECDL system with operating currents of 211 and 213 mA. We can observe the periodic LFO for both injected currents. The corresponding oscillation frequencies are around 20 and 29 MHz with 211 and 213 mA injected currents, respectively. For both injected currents, we can observe the pulse packages consisted of pulses occurring at the external-cavity delay interval, this means the regular PPO takes place for both injected currents. The oscillation frequency of the regular PPO, ν_{LFO}, observed in **Figures 10** and **11** show its increase with the current injected to the laser device. This phenomenon was also observed in an integrated semiconductor laser with short-cavity feedback [38]. The intensity noise spectra with these two injected currents are also measured; the results are similar to the results shown in **Figure 10(b)** and consistent with the time series shown in **Figure 11**.

The operating current is increased until to 420 mA, that is, more than twice the threshold of the ECDL system. The measured time series and intensity noise spectra at injected currents of

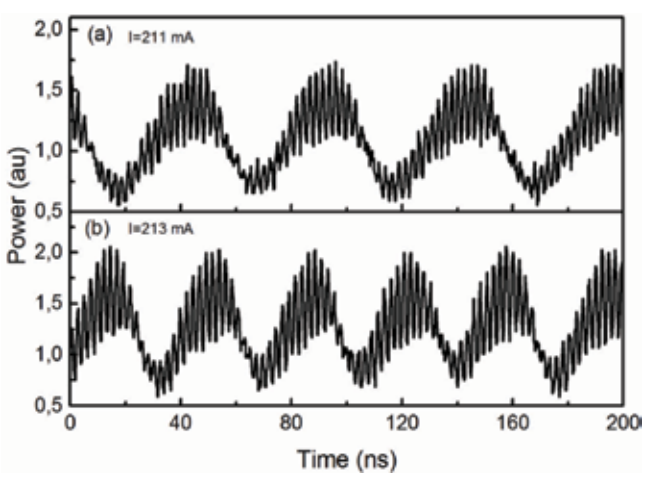

Figure 11. Time series of the output beam from the green ECDL system with an injected current of (a) 211 mA and (b) 213 mA.

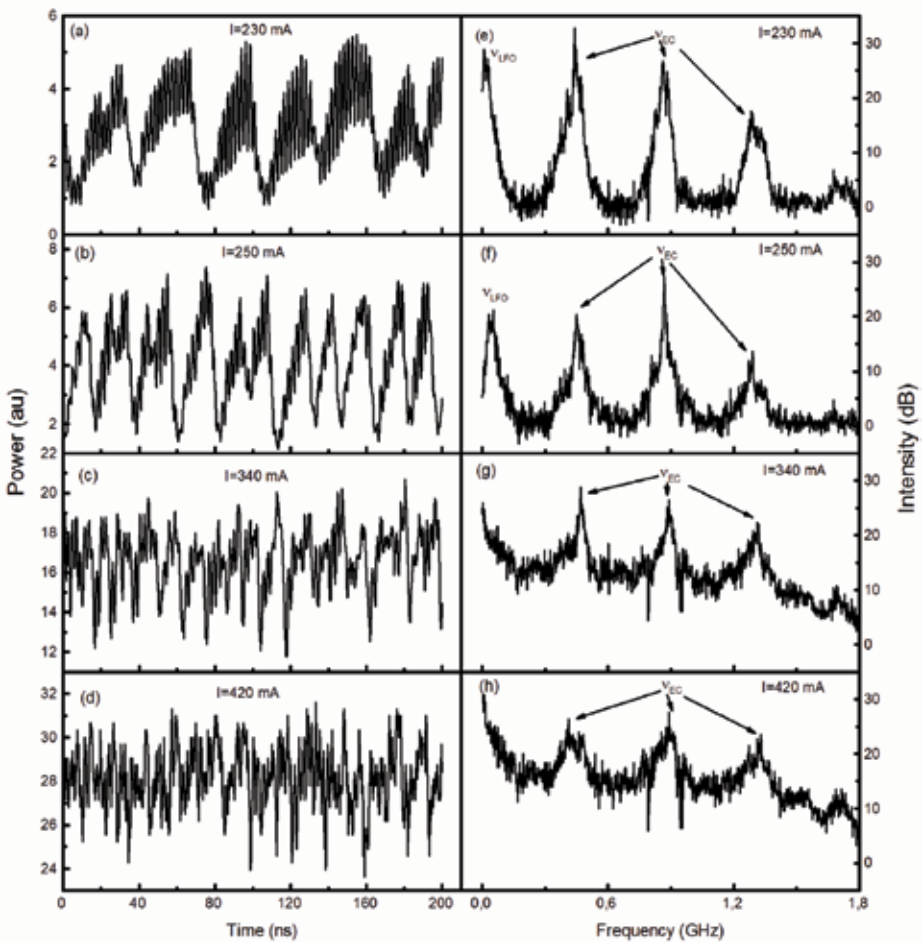

Figure 12. Time series and intensity noise spectra of the output beam from the green ECDL with the injected current of (a, e) 230 mA, (b, f) 250 mA, (c, g) 340 mA and (d, h) 420 mA.

230, 250, 340 and 420 mA are shown in **Figure 12**. The pulse packages first oscillate irregularly, as shown in **Figure 12(a**, **e)** with an injected current of 230 mA. The time series in **Figure 12(a)** shows the pulse packages consisting of the pulse train with the period of external-cavity delay time oscillate irregular. The intensity noise spectrum in **Figure 12(e)** shows the peak for LFO and peaks for external-cavity oscillation at multiples of ν_{EC}. However, the peaks at $\nu_{EC} \pm \nu_{LFO}$ originating from the mixing of external-cavity frequency ν_{EC} and LFO frequency ν_{LFO}, which is the indication of regular PPO are not observed. The broad peaks for ν_{EC} and ν_{LFO} mean that the intensity noise is increased strongly, and the dynamics of the laser system is more complex. When the operating current is increased to 250 mA, the time series in **Figure 12(b)** shows irregular PPO, and the high-frequency external-cavity oscillation is not as clear as in the condition of low injected current. The average duration of the pulse package is less than 20 ns. The broad peaks for ν_{EC} and ν_{LFO} mean the dynamic behavior of the laser system is more complex. The pulse package is not clear with the operated current of 340 mA, and the pulses

occurring at the external-cavity delay interval are almost invisible, as shown in **Figure 12(c)**. Finally, the time series shows a chaotic behavior with an injected current of 420 mA. The corresponding intensity noise spectra for the injected currents of 340 and 420 mA are shown in **Figure 12(g, h)**. The peak for LFO is not observed, and the broad intensity noise spectra from low to high frequency indicate typical chaotic dynamics of the output beam.

The external-cavity feedback is classified into two regimes: short- and long-cavity regimes. When the relaxation oscillation frequency of the solitary diode laser, ν_{RO}, is lower than ν_{EC}, the feedback is in short-cavity regime; otherwise, it is in long-cavity regime [26, 38, 39]. Regular PPO was first observed in 2001 by Heil et al. in short-cavity feedback narrow-strip diode laser systems [26]. With moderate feedback strength, the previous study shows that the PPO mainly takes place in the diode laser with short-cavity feedback, while LFF and chaos take place in the long-cavity regime [29, 38]. Recently, we observed regular PPO in a BAL with a lateral-mode-selected long-cavity feedback [36]. Here, regular PPO is observed in a BAL with grating external-cavity feedback. Different routes to chaos in different ECDL systems have been found [23, 40], here, we observe the transition from regular PPO to chaos in the green GaN BAL with grating external-cavity feedback.

Normally, an external-cavity length of a few centimeters is classified into short-cavity regime, thus in this point, the 33 cm external-cavity length in our case is in the long-cavity regime. The ν_{RO} of the solitary diode laser is proportional to the square root of the difference between the injected current and the solitary laser threshold current [38, 39]. This means the definition of ν_{RO} is valid only when the injected current is higher than the threshold current of the solitary laser, and the classification of short- and long-cavity regime is meaningful only on such condition. In our experiment, the PPO mainly takes place with the operating current lower than the threshold of the solitary laser. In this point, this is a new regime for the ECDL system.

In summary, the dynamics of the green high-power ECDL system with grating feedback operated in *p*-polarized mode is investigated. As the increase of the injected current, different dynamic behaviors from regular PPO, irregular PPO, to chaos are observed.

4. Conclusion

Both blue and green high-power, tunable, narrow-bandwidth ECDL systems based on GaN broad-area diode lasers and external grating feedback are demonstrated. For the blue ECDL, two gratings are applied. The holographic grating is for obtaining high power, a 530 mW output power with a tunable range of 1.4 nm is obtained with this grating; the ruled grating is for achieving broad tunable range, an output power of 80 mW with a tunable range of 6.0 nm is achieved with the ruled grating. For the green ECDL, the laser system can be operated in two modes, for *p*-polarized mode operation, an output power of 50 mW with a tunable range of 9.2 nm is obtained; for *s*-polarized mode operation, an output power of 480 mW with a tunable range of 2.1 nm is achieved.

The tuning range and the output power optimization of an external-cavity diode laser system with grating feedback is investigated based on the experimental results on the blue and green

ECDL systems and diode laser theory. The obtained results can be used as a guide to select grating for an ECDL system for different applications. The dynamic behavior of the green ECDL system operated in *p*-polarized mode is studied. As the increase of the injected current, different dynamic states, such as regular PPO, irregular PPO and chaos are observed.

Acknowledgements

This work was supported in part by the Danish Energy Technology Development and Demonstration Program (EUDP) under Grant 64014-0171.

Author details

Mingjun Chi*, Ole Bjarlin Jensen, Anders Kragh Hansen and Paul Michael Petersen

*Address all correspondence to: mchi@fotonik.dtu.dk

DTU Fotonk, Department of Photonics Engineering, Technical University of Denmark, Roskilde, Denmark

References

[1] Nakamura S, Senoh M, Nagahama S, Iwasa N, Yamada T, Matsushita T, Sugimoto Y, Kiyoku H. Room-temperature continuous-wave operation of InGaN multi-quantum-well structure laser diodes. Applied Physics Letters. 1996;**69**:4056-4058. DOI: 10.1063/1.117816

[2] http://www.nichia.co.jp

[3] Kang JH, Wenzel H, Hoffmann V, Freier E, Sulmoni L, Unger RS, Einfeldt S, Wernicke T, Kneissl M. DFB laser diodes based on GaN using 10^{th} order laterally coupled surface gratings. IEEE Photonics Technology Letters. 2018;**30**:231-234. DOI: 10.1109/LPT.2017.2780446

[4] Holc K, Bielecki Z, Wojtas J, Perlin P, Goss J, Czyzewski A, Magryta P, Stacewicz T. Blue laser diodes for trace matter detection. Optica Applicata. 2010;**40**:641-651

[5] Tanaka T, Takahashi K, Sako K, Kasegawa R, Toishi M, Watanabe K, Samuels D, Takeya M. Littrow-type external-cavity blue laser for holographic data storage. Applied Optics. 2007;**46**:3583-3592. DOI: 10.1364/AO.46.003583

[6] Shimada Y, Chida Y, Ohtsubo N, Aoki T, Takeuchi M, Kuga T, Torii Y. A simplified 461-nm laser system using blue diodes and a hollow cathode lamp for laser cooling of Sr. The Review of Scientific Instruments. 2013;**48**:063101. DOI: 10.1063/1.4808246

[7] Hofmann J, Blume G, Jedrzejczyk D, Eppich B, Feise D, Kreutzmann S, Sahm A, Paschke K. Miniaturized diode laser module emitting green light at 532 nm with a power of more

than 900 mW for next-generation holographic displays. Optical Review. 2016;**23**:141-145. DOI: 10.1007/s10043

[8] Müller A, Marschall S, Jensen OB, Fricke J, Wenzel H, Sumpf B, Andersen PE. Diode laser based light sources for biomedical applications. Laser & Photonics Reviews. 2013;**7**:605-627. DOI: 10.1002/lpor.201200051

[9] Ruhnke N, Müller A, Eppich B, Maiwald M, Sumpf B, Erbert G, Tränkle G. Compact deep UV system at 222.5 nm based on frequency doubling of GaN laser diode emission. IEEE Photonics Technology Letters. 2018;**30**:289-292. DOI: 10.1109/LPT.2017.2787463

[10] Gürel K, Wittwer VJ, Hoffmann M, Saraceno CJ, Hakobyan S, Resan B, Rohrbacher A, Weingarten K, Schilt S, Südmeyer T. Green-diode-pumped femtosecond Ti: Sapphire laser with up to 450 mW average power. Optics Express. 2015;**23**:30043-30048. DOI: 10.1364/OE.23.030043

[11] Fiebig C, Sahm A, Uebernickel M, Blume G, Eppich B, Paschke K, Erbert G. Compact second-harmonic generation laser module with 1 W optical output power at 490 nm. Optics Express. 2009;**17**:22785-22790. DOI: 10.1364/OE.17.022785

[12] Hansen AK, Andersen PE, Jensen OB, Sumpf B, Erbert G, Petersen PM. Highly efficient single-pass sum frequency generation by cascaded nonlinear crystals. Optics Letters. 2015;**40**:5526-5529. DOI: 10.1364/OL.40.005526

[13] Ruhnke N, Müller A, Eppich B, Maiwald M, Sumpf B, Erbert G, Tränkle G. 400 mW external cavity diode laser with narrowband emission at 445 nm. Optics Letters. 2014;**39**:3794-3797. DOI: 10.1364/OL.39.003794

[14] Chen YH, Lin WC, Chen HZ, Shy JT, Chui HC. Single-frequency external cavity green diode laser. IEEE Photonics Journal. 2017;**9**:1507207. DOI: 10.1109/JPHOT.2017.2776284

[15] Chi M, Jensen OB, Petersen PM. Tuning range and output power optimization of an external-cavity GaN diode laser at 455 nm. Applied Optics. 2016;**55**:2263-2269. DOI: 10.1364/AO.55.002263

[16] Chi M, Jensen OB, Petersen PM. Green high-power tunable external-cavity GaN diode laser at 515 nm. Optics Letters. 2016;**41**:4154-4157. DOI: 10.1364/OL.41.004154

[17] Unger P. Introduction to power diode lasers. In: Diehl R, editor. High-Power Diode Lasers, Fundamentals, Technology, Applications. Berlin Heidelberg: Springer-Verlag; 2000. pp. 37-46

[18] Conroy RS, Hewett JJ, Lancaster GPT, Sibbett W, Allen JW, Dholakia K. Characterisation of an extended cavity violet diode laser. Optics Communication. 2000;**175**:185-188. DOI: 10.1016/S0030-4018(99)00742-7

[19] Lonsdale DJ, Willis AP, King TA. Extended tuning and single-mode operation of an anti-reflection-coated InGaN violet laser diode in a Littrow cavity. Measurement Science and Technology. 2002;**13**:488-493. DOI: 10.1088/0957-0233/13/4/310

[20] Soriano MC, García-Ojalvo J, Mirasso CR, Fischer I. Complex photonics: Dynamics and applications of delay-coupled semiconductors lasers. Reviews of Modern Physics. 2013;**85**:421-470. DOI: 10.1103/RevModPhys.85.421

[21] Sciamanna M, Shore KA. Physics and applications of laser diode chaos. Nature Photonics. 2015;**9**:151-162. DOI: 10.1038/nphoton.2014.326

[22] Chi M, Jensen OB, Hansen AK, Petersen PM. Dynamics of a green high-power tunable external-cavity broad-area GaN diode laser. Journal of the Optical Society of America B: Optical Physics. 2018;**35**:667-671. DOI: 10.1364/JOSAB.35.000667

[23] Ye J, Li H, McInerney JG. Period-doubling route to chaos in a semiconductor laser with weak optical feedback. Physical Review A. 1993;**47**:2249-2252. DOI: 10.1103/PhysRevA.47.2249

[24] Hohl A, Gavrielides A. Bifurcation cascade in a semiconductor laser subject to optical feedback. Physical Review Letters. 1999;**82**:1148-1151. DOI: 10.1103/PhysRevLett.82.1148

[25] Lawrence JS, Kane DM. Contrasting conventional optical and phase-conjugate feedback in laser diodes. Physical Review A. 2001;**63**:033805. DOI: 10.1103/PhysRevA.63.033805

[26] Heil T, Fischer I, Elsäβer W, Gavrielides A. Dynamics of semiconductor lasers subject to delayed optical feedback: The short cavity regime. Physical Review Letters. 2001; **87**:243901. DOI: 10.1103/PhysRevLett.87.243901

[27] Mandre SK, Fischer I, Elsässer W. Control of the spatiotemporal emission of a broad-area semiconductor laser by spatially filtered feedback. Optics Letters. 2003;**28**:1135-1137. DOI: 10.1364/OL.28.001135

[28] Mandre SK, Fischer I, Elsässer W. Spatiotemporal emission dynamics of a broad-area semiconductor laser in an external cavity: Stabilization and feedback-induced instabilities. Optics Communication. 2005;**244**:355-365. DOI: 10.1016/j.optcom.2004.09.058

[29] Takeda A, Shogenji R, Ohtsubo J. Dynamics and pulse-package oscillations in broad-area semiconductor lasers with short optical feedback. Applied Physics Letters. 2012; **101**:231105. DOI: 10.1063/1.4769181

[30] Lawrence JS, Kane DM. Broad-area diode lasers with plane-mirror and phase-conjugate feedback. Journal of Lightwave Technology. 2002;**20**:100-104. DOI: 10.1109/50.974824

[31] Fujita Y, Ohtsubo J. Optical-feedback-induced stability and instability in broad-area semiconductor lasers. Applied Physics Letters. 2005;**87**:031112. DOI: 10.1063/1.1999850

[32] Arahata M, Uchida A. Inphase and antiphase dynamics of spatially-resolved light intensities emitted by a chaotic broad-area semiconductor laser. IEEE Journal of Selected Topics in Quantum Electronics. 2015;**21**:1800609. DOI: 10.1109/JSTQE.2015.2422473

[33] Vasil'ev PP, White IH. Phase-conjugation broad area twin-contact semiconductor laser. Applied Physics Letters. 1997;**71**:40-42. DOI: 10.1063/1.119462

[34] Tachikawa T, Shogenji R, Ohtsubo J. Observation of multi-path interference in broad-area semiconductor lasers with optical feedback. Optical Review. 2009;**16**:533-539. DOI: 10.1007/s10043-009-0105-5

[35] Wolff S, Rodionov A, Sherstobitov VE, Doering C, Fouckhardt H. Self-pulsation in broad-area lasers with transverse-mode selective feedback. Optics Communication. 2006; **265**:642-648. DOI: 10.1016/j.optcom.2006.04.008

[36] Chi M, Petersen PM. Dynamics of a broad-area diode laser with lateral-mode-selected long-cavity feedback. Journal of Applied Physics. 2014;**116**:103101. DOI: 10.1063/1.4894628

[37] Pan M, Evans DJ, Gray GR, Smith LM, Benner RE, Johnson CW, Knowlton DD. Spatial and temporal coherence of broad-area lasers with grating feedback. Journal of the Optical Society of America B: Optical Physics. 1998;**15**:2531-2536. DOI: 10.1364/JOSAB.15.002531

[38] Toomey JP, Kane DM, McMahon C, Argyris A, Syvridis D. Integrated semiconductor laser with optical feedback: Transition from short to long cavity regime. Optics Express. 2015;**23**:18754-18762. DOI: 10.1364/OE.23.018754

[39] Heil T, Fischer I, Elsäβer W, Krauskopf B, Green K, Gavrielides A. Delay dynamics of semiconductor lasers with short external cavities: Bifurcation scenarios and mechanisms. Physical Review E. 2003;**67**:066214. DOI: 10.1103/PhysRevE.67.066214

[40] Li N, Susanto H, Cemlyn BR, Henning ID, Adams MJ. Stability and bifurcation analysis of spin-polarized vertical-cavity surface-emitting lasers. Physical Review A. 2017; **96**:013840. DOI: 10.1103/PhysRevA.96.013840

Chapter 2

Cladding Pumped Thulium-Ytterbium Short Pulse Fiber Lasers

Babar Ibrahim Muhammad

Additional information is available at the end of the chapter

http://dx.doi.org/10.5772/intechopen.81060

Abstract

This chapter describes double clad fiber along with cladding pump technique in which pump light is coupled in the inner cladding of fiber thereby interacting with doped core through total internal reflection. Lasers operating in continuous wave mode have limited output power. Their output power can be enhanced to a great extent by concentrating the available energy in a single or in a periodic sequence of optical pulses. This is achieved by Q-switch and modelock techniques. Q-switched and modelocked lasers can be realized by active and passive means. Active technique is based on active loss modulation by using mechanical, electro-optic or acousto-optic based modulators. However, such techniques require complicated electronic circuits and have limited gain bandwidth. The attention then moves towards the passive technique which is low cost, compact in size, gives reliable operation without high voltages and provides simple cavity design without need for external electronics. Passive technique employs a saturable absorber, based on materials like carbon nanotubes, graphene, molybdenum di-sulfide etc. A brief description of pulsed fiber lasers and solitons in view of modelocking are described in the text. Moreover examples of Q-switched and modelocked lasers are also presented by using Thulium-Ytterbium co-doped double clad fiber. A cladding pump technique is employed for the purpose.

Keywords: fiber laser, double clad fiber, cladding pump, Q-switched, modelocked

1. Introduction

Fiber laser is a mature technology that has become an essential tool facilitating a wide range of scientific, medical, and industrial applications. Fiber lasers are advancing rapidly due to their ability to generate stable, efficient, and diffraction-limited beams with significant peak and average powers.

In fiber optics, optical signals travel in hair thin strands of glass or plastic fiber [10]. The light propagates in the core at the center of the fiber, surrounded by an optical material called cladding that confines the light in the core employing the phenomenon of total internal reflection. There are two basic types of fibers: single-mode and multi-mode fibers. Single-mode fiber has a core diameter of 8.3–10 microns and supports only one mode of transmission. Multi-mode fiber has a core diameter of either 50 or 62.5 microns. Multimode fibers support multiple modes as shown in **Figure 1**. Due to their smaller core size, these fibers cannot support high power pump sources and therefore cannot generate high output power.

To overcome the three limitations (small core radius, larger attenuation, and dispersion) of high speed transmission, a new type of optical fiber called double clad optical fiber is proposed [2]. It consists of three layers of optical material instead of the usual two as shown in **Figure 2**. The inner-most layer is called the core, surrounded by the inner cladding, while the inner cladding is surrounded by the outer cladding. All the three layers are made of materials with different refractive indices. The typical refractive index profiles are shown in **Figure 3**. Generally, the outer cladding is made of a polymer material rather than glass. Refractive index of inner cladding is higher than the outer cladding. This enables the inner cladding to guide light by total internal reflection, but for a different range of wavelengths than the core. Also, the inner cladding has larger area and higher numerical aperture so that it can support large number of modes. This allows multi-mode laser diodes to be used as the pump source, which possess high power but low brightness.

1.1. Cladding pump

The pump light can be easily coupled into the large inner cladding and propagates through the inner cladding, while the signal propagates in the smaller core as shown in **Figure 4**. The

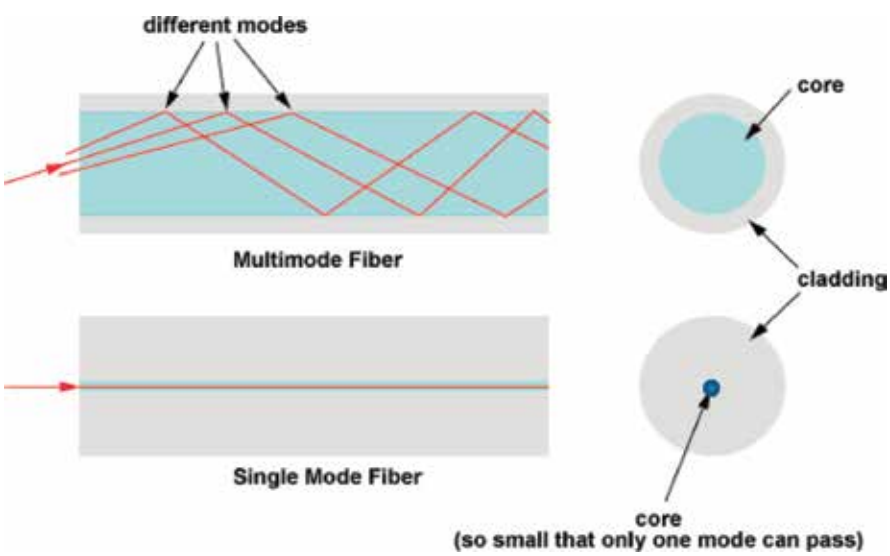

Figure 1. Mode propagation in single- and multi-mode fibers [1].

http://dx.doi.org/10.5772/intechopen.81060

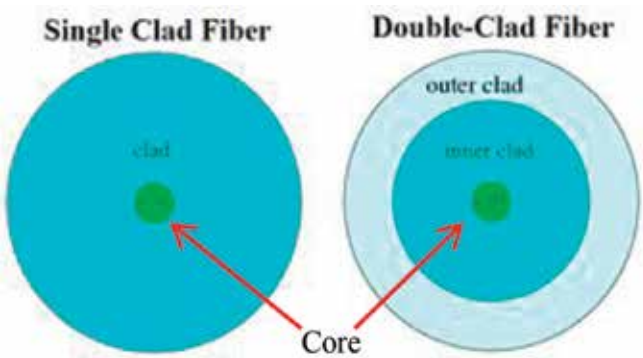

Figure 2. Structure of single and double clad fibers.

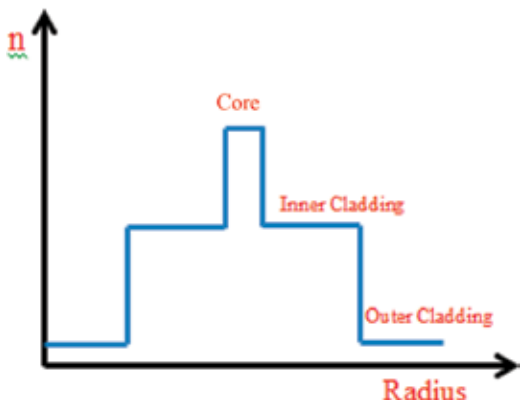

Figure 3. Typical refractive index profile of double clad optical fiber.

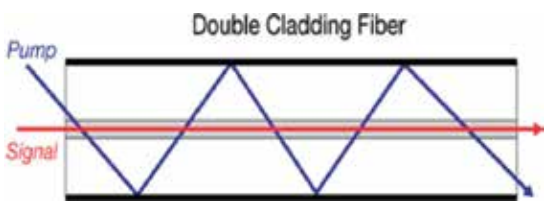

Figure 4. Cladding pump scheme.

doped core gradually absorbs light from the cladding as it propagates through the core and amplifies it [4]. This type of pumping scheme is referred as cladding pumping, an alternate scheme to the conventional core pumping, where the pump light is coupled into the small core. Cladding pumping has revolutionized the design of fiber amplifiers and fiber lasers [3]. Using this technique, contemporary fiber lasers can generate continuous power up to several kilowatts, besides allowing the signal light to maintain near diffraction limited beam quality [4].

In a double clad fiber, cladding shape is of extreme importance, particularly in case of small core diameter compared to the cladding size. Circular symmetry is considered the worst in a double clad fiber, because many modes of light in the cladding missed the core, therefore cannot pump the core [5]. Normally, claddings are noncircular, which enhance the absorption of the pump light in the doped core [7]. Different shapes of inner cladding are shown in **Figure 5** for rare earth doped fibers.

Hence, double clad cladding pumped fiber lasers are regarded as devices that can generate diffraction limited single-mode laser light using multi-mode laser diodes as the pump. Due to large size of inner cladding, high pump powers can be injected in a double clad fiber. However, the core size puts limits on the output power due to the danger of optical damage and thermal effects [7].

Different lasers operating in continuous wave or quasi-continuous wave mode have limited optical output power, linked with the maximum available pump power [10]. The peak output power of a laser can be enhanced by concentrating the available energy in a single, short optical pulse, or in a periodic sequence of optical pulses as in Q-switched and modelocked fiber lasers.

1.2. Q-switched lasers

Q-switching, also known as giant pulse formation or Q-spoiling, [8] is a powerful technique by which a laser can be made to produce a pulsed output beam. This technique is capable of producing light pulses with extremely high (gigawatt) peak power, much higher than the continuous wave mode (constant output) operation of the laser. As compared to modelocking, another technique for pulse generation with lasers, Q-switching leads to much lower pulse repetition rates, much higher pulse energies, and much longer pulse durations than it. It was in 1958 when Q-switching was proposed by Gordon Gould [9]. Practically, it was achieved in 1961 or 1962 by Hellwarth and McClung using Kerr cell shutters in a ruby laser, and these require electricity for switching [10].

A variable attenuator is required inside the laser's optical resonator to produce Q-switched laser light. When the attenuator is functioning, light which leaves the gain medium does not

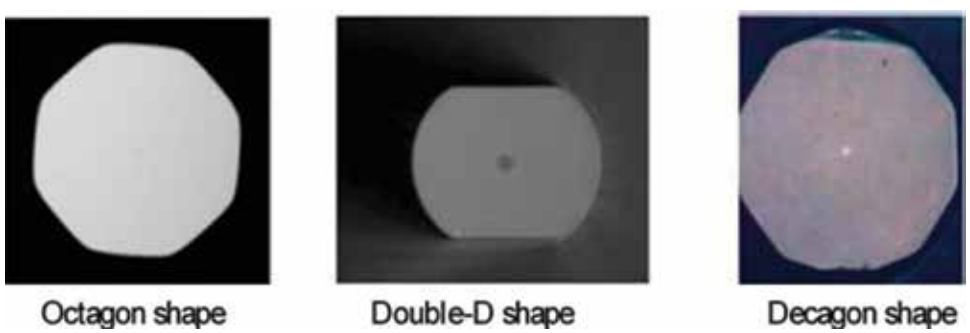

Figure 5. Cross-sectional images of a few inner cladding shapes used in double clad fiber lasers (a) octagon (b) double-D (c) decagon [6].

return or cannot travel back and forth, this restricts the lasing, putting the optical cavity in low Q factor or high loss condition. A high Q factor represents low resonator losses per round trip. The variable attenuator is commonly known as "Q-switch."

First, the laser medium is pumped, while the Q-switch is set to prevent feedback of light into the gain medium (producing an optical resonator with low Q factor). This produces a population inversion by losing pump energy through absorption by electrons, thus pumping electrons to higher energy level; this accumulates energy in the gain medium. However, the laser operation cannot yet begin, because there is no feedback from the resonator [3]. As the rate of stimulated emission depends on the amount of light entering the medium, therefore, the amount of energy stored in the gain medium increases as the medium is pumped. Due to losses from spontaneous emission along with other processes, the stored energy takes some time to reach some maximum level; the medium is said to be gain saturated. At this point, Q-switch rapidly changes from low to high Q, allowing feedback and the process of optical amplification by stimulated emission to begin [3]. Since a large amount of energy is already stored in the gain medium, the intensity of light in the laser resonator builds up very quickly; this also causes the energy stored in the medium to be depleted almost as quickly. This develops a short pulse of light output from the laser, known as a giant pulse, which may have very high peak intensity. Generally, several round trips are needed to completely depopulate the upper energy level and several more round trips to empty the optical cavity, so the duration of the pulse is greater than one round trip. The peak power (the pulse energy divided by its duration) of these lasers can be in the megawatt range or even higher. There are two main techniques for Q-switching: active and passive.

1.2.1. Active Q-switching

In active Q-switching, the losses are modulated with an active control element so-called active Q-switcher, either by using an acousto-optic or electro-optic modulator, which requires an external electrical signal to operate. The pulse is formed shortly after an electrical trigger signal arrives. There is also mechanical type Q-switchers such as spinning mirrors, used as end mirrors of laser resonators. The pulse repetition rate can be controlled by the active modulator in an actively Q-switched laser. Higher repetition rates lead to lower pulse energies.

1.2.2. Passive Q-switching

In passive Q-switching, the losses are modulated or controlled by optical cavity light, rather than some external electrical source. A saturable absorber device is normally used as a Q-switcher in this technique. The transmission of this device increases when the intensity of light exceeds some threshold. The material may be an ion-doped crystal like Cr:YAG (chromium-doped Yttrium-Aluminum garnet), which is used for Q-switching of Nd:YAG (neodymium-doped Yttrium-Aluminum garnet) lasers, a bleachable dye, graphene mechanical exfoliation and PVA thin film, semiconductor saturable absorber mirrors (SESAM), and carbon nanotubes embedded in PVA thin films. Initially, the loss of the absorber is high, once a large amount of energy is stored in the gain medium, the laser power increases, and it saturates the absorber, and light can pass through as there are no electrons in the ground state

to absorb pumped energy. As soon as the energy is depleted in the resonator, the absorber recovers to its high loss state before the gain recovers, so that the next pulse is delayed until the energy in the gain medium is fully replenished. In this way, it works as an on-off optical switch to generate pulses. The pulse repetition rate can only be controlled indirectly by varying the laser's pump power and the amount of saturable absorber in the cavity. For direct control of the repetition rate, a pulsed pump source is needed.

Passive Q switching is simpler and cost effective as compared to the active one. It eliminates the modulator and its electronics. Moreover, it is suitable for very high pulse repetition rates, but with lower pulse energies. External triggering of the pulses is not possible (except with an optical pulse from another source), and also pulse energy and duration are often more or less independent of the pump power, which only determines the pulse repetition rate [11, 12].

1.3. Modelocked lasers

In laser technology, modelocking refers to a technique by which a laser can be made to generate pulses of extremely short duration, of the order of picoseconds (10^{-12} s) or femtoseconds (10^{-15} s). This is achieved by establishing a fixed-phase relationship between the longitudinal modes of the laser's resonant cavity. The laser is then referred as phaselocked or modelocked. Interference between these modes causes the laser light to be produced as a train of pulses. In a simple laser, different modes oscillate independently, without a fixed relationship between each other, like a set of independent lasers all emitting light at slightly different frequencies. In lasers with few oscillating modes, interference between the modes produces beats in the laser output, leading to fluctuations in intensity; whereas in lasers with many thousands of modes, interference between modes tend to average to a near-constant output intensity. **Figure 6** shows the electric fields of five modes with random phase and the power of the total signal distributed in a random fashion.

On the other hand, if each mode operates with a fixed phase relationship between it and the other modes, all modes of the laser will periodically constructively interfere with one another, generating an intense burst or pulse of light instead of random or constant output intensity as shown in **Figure 7**. Such a laser is termed as modelocked or phaselocked laser. These pulses are separated in time by $\tau = 2\ L/c$, where τ is the time taken for the light to make exactly one round trip of the laser cavity, L is the length of laser cavity, and c is the speed of light. The frequency is exactly equal to the mode spacing of the laser, $\Delta\nu = 1/\tau$. The duration of each pulse is determined by the number of modes which are oscillating in phase. Suppose there are N modes locked with a frequency separation $\Delta\nu$, the overall modelocked bandwidth is $N\Delta\nu$, and the wider the bandwidth, the shorter the pulse duration of the laser [5].

The actual pulse duration is determined by the shape of each pulse, which is measured by the amplitude and phase relationship of each longitudinal mode. As an example, a laser producing pulses with a Gaussian temporal shape, the minimum possible pulse duration Δt is given by the equation

$$\Delta t = \frac{0.441}{N\Delta\nu} \tag{1}$$

http://dx.doi.org/10.5772/intechopen.81060

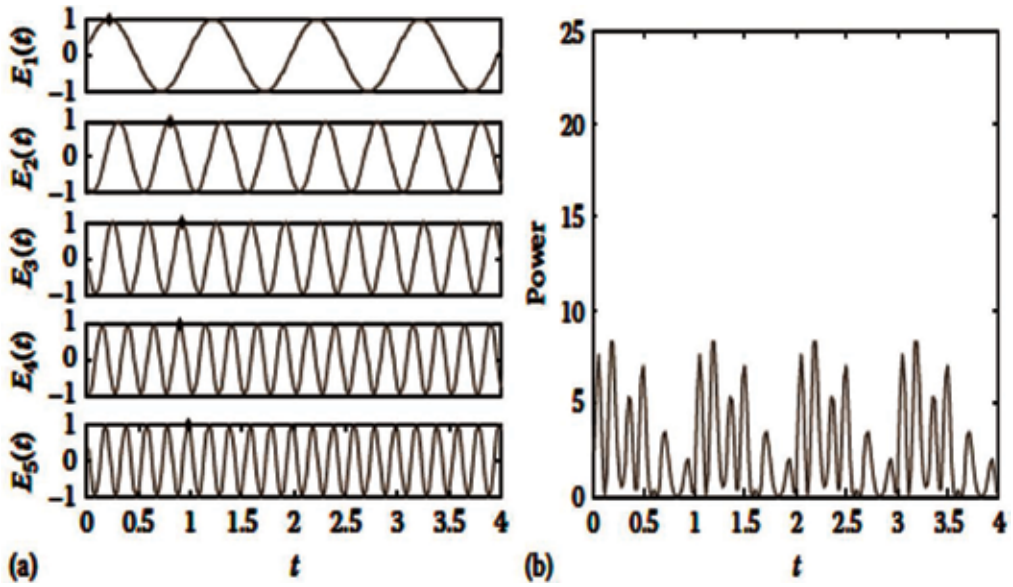

Figure 6. Plots of (a) electric field amplitudes of five individual modes of randomly distributed phases and (b) power of the total signal of a multi-longitudinal mode laser [13].

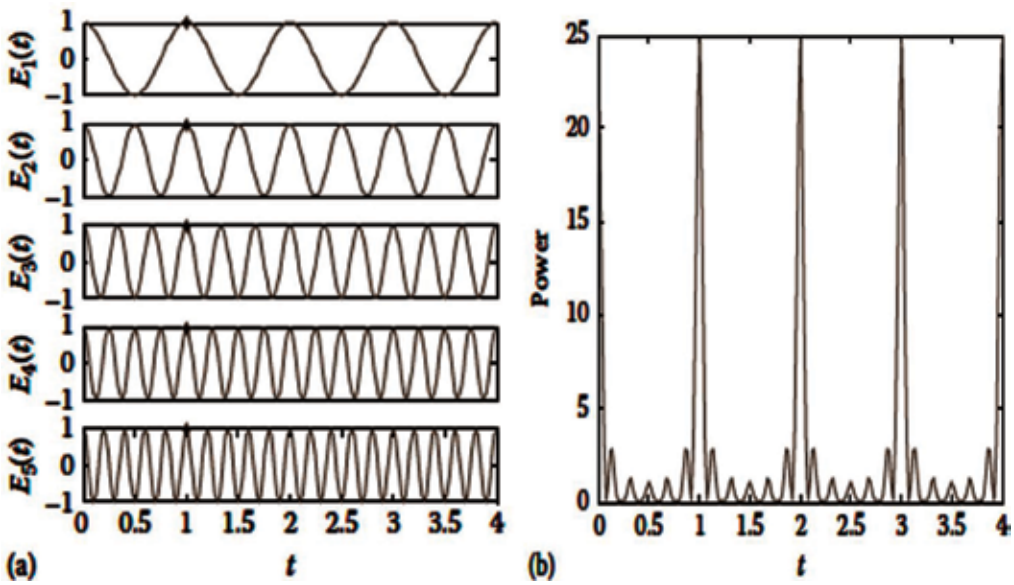

Figure 7. Plots of (a) electrical field amplitudes of five in-phase individual modes and (b) the total power of a periodic pulse train [13].

The value 0.441 is known as the "time-bandwidth product" of the pulse and varies depending on the pulse shape. Generally for ultra-short pulse lasers, a hyperbolic-secant-squared ($sech^2$) pulse shape is considered, giving a time-bandwidth product of 0.315. Using this equation,

the minimum pulse duration can be calculated consistent with the measured laser spectral width [13].

Modelocked fiber lasers are capable of producing pulses with widths from close to 30 fs to 1 ns at repetition rates, ranging from less than 1 MHz to 100 GHz. This broad range along with a compact size of optical fiber lasers is quite unique in laser technology, making them feasible for a large range of applications. As modelocked fiber laser technology was developed and these lasers became commercially available, they have been used in various fields, such as laser radar, all-optical scanning delay lines, THz generation, injection-seeding, two-photon microscopes, optical telecommunications, and nonlinear frequency conversion, just to mention the most widely publicized areas [12]. Surely, modelocked fiber lasers are a premier source of short optical pulses sharing an equal position with semiconductor and solid-state lasers [14].

1.3.1. Modelocking methods

Modelocked lasers can be produced by using either active or passive methods. In active modelocking, the optical modulator such as acousto-optic modulator is used with the help of an external electrical signal, as a modelocker. On the other hand, passive modelocking does not need an external signal to operate [15]. The modelocking is achieved by modulating an intra-cavity light using some intra-cavity elements, such as nonlinear polarization rotation and saturable absorber. Most of the passively modelocked lasers are achieved using a saturable absorber since it allows the generation of much shorter (femtosecond) pulses. This is attributed to the saturable absorber used, which can adjust the resonator losses much faster than an electronic modulator: the shorter the pulse becomes, the faster the loss modulation, if the absorber has a sufficiently short recovery time [14]. The pulse width can be even smaller than the recovery time of the absorber [6].

In addition, there are some passive modelocking schemes that do not require materials that directly display an intensity dependent absorption. These methods use nonlinear optical effects in intra-cavity components to provide a method of selectively amplify high intensity light in the cavity and attenuate low intensity light in the cavity. Among them, the most successful scheme is Kerr-lens modelocking (KLM), also sometimes referred to as "self-modelocking." This technique uses a nonlinear optical process, the optical Kerr effect, which results in high intensity light being focused differently from low intensity light. By careful arrangement of an aperture in the laser cavity, this effect can be made to produce the equivalent of an ultra-fast response time saturable absorber.

1.4. Optical solitons

A fascinating manifestation of the fiber nonlinearity is the development of optical solitons, created due to the balance between dispersive and nonlinear effects [8]. Solitons are a unique type of wave packets, capable of propagating unaltered over long distances inside a fiber.

Solitons have been discovered in many branches of physics. In the field of photonics, especially in fiber optics, solitons not only are of fundamental interest, but they have also found practical applications in the field of fiber-optic communications [16].

The pulse maintains the shape and width, along the entire length of the fiber, if the effects of SPM and GVD cancel out with each other. Such a pulse is called solitary wave pulse or soliton. The pulse that has the above property is the sech profile pulse, which is a solution of the nonlinear Schrodinger equation NLSE [13].

Figure 8 shows the spectrum of different types of modelocked fiber lasers. The conventional soliton and stretched pulse are obtained in anomalous dispersion fiber laser setup, where the pulse shaping is mainly due to the natural balance between the anomalous dispersion and the fiber nonlinearity. On the other hand, dissipative solitons (DSs) are obtained in the normal dispersion region as a result of the combined effects among the fiber nonlinearity, cavity dispersion, gain and loss, and spectral filtering [13]. Moreover, the soliton shaping is strongly dependent on the dissipative effects. Consequently, dissipative solitons have a wider pulse duration and lower peak power, compared to conventional solitons and stretched solitons [17].

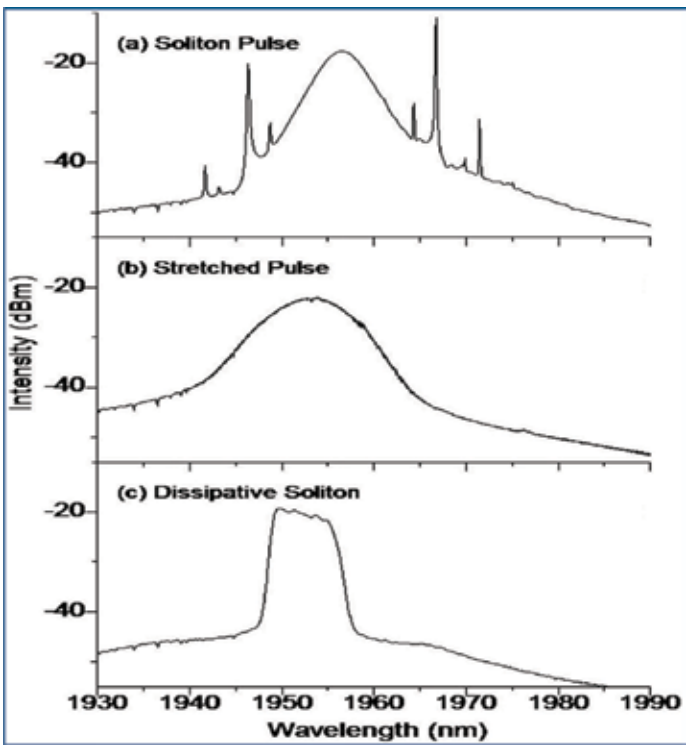

Figure 8. Different types of solitons [17].

2. Q-switched TYDFL using multi-walled carbon nanotubes passive saturable absorber

There are growing interests in compact Q-switched laser sources that operate in the mid-infrared spectral region around 2 microns. This is mainly driven by the applications in spectroscopy, communication, material processing, manufacturing, sensing, medicine, and nonlinear optical research [18, 19]. Nowadays, another type of nanotube called multi-walled carbon nanotubes (MWCNT) has been examined in the field of nonlinear optics because its production cost is 50–80% lower than SWNTs [9]. MWCNTs also have higher mechanical strength, higher photon absorption per nanotube, and higher mass density which leads to better stability [20].

We successfully demonstrated, a Thulium-Ytterbium co-doped fiber (TYDF) Q-switched laser using a laboratory made saturable absorber based on MWCNTs implanted in polyvinyl alcohol (PVA) composite for the first time [2]. A homemade double clad Thulium-Ytterbium co-doped fiber (TYDF) drawn from a preform which was manufactured based on the modified chemical vapor deposition (MCVD) and solution doping processes is used as a lasing medium. The fabricated MWCNT-PVA film (SA) is attached within the laser cavity by sandwiching it between two fiber connectors. Similarly, a modelocked TYDFL is also demonstrated using graphene PVA film as a saturable absorber.

2.1. Configuration of the Q-switched TYDFL

The schematic of the proposed Q-switched TYDFL is shown in **Figure 9**. It is constructed using a simple ring cavity, in which a 15-m long laboratory made TYDF is used for the active medium. An indigenously developed MWCNT-PVA-based SA was used as a Q-switcher. The double clad TYDF was forward pumped by a 905-nm multi-mode laser diode via a MMC.

2.2. Q-switching performance of Thulium-Ytterbium co-doped fiber laser

Initially, the continuous wave (CW) TYDFL was investigated without using the SA, and the laser threshold was found to be at 1.0 W pump power. When SA is inserted in the cavity, stable and self-starting Q-switching operation is obtained just by adjusting the pump power at a threshold value of 1.6 W, which is higher than that of the CW TYDFL because of the presence of SA in the cavity which increases the loss [2]. **Figure 10** shows the output spectrum of the Q-switched TYDFL at the threshold (1.6 W) pump power. As seen in the figure, the laser operates at 1977.5 nm with an optical to signal noise ratio (OSNR) of around 30 dB.

Figure 11(a) and **(b)** shows the temporal analysis and the corresponding single pulse envelop of a typical Q-switched pulse train, respectively, at a pump power of 1.6 W [2]. The spacing between two pulses in **Figure 11(a)** is around 53 μs, which can be translated to a repetition rate of 18.8 kHz. The corresponding pulse width is around 8.6 μs as shown in **Figure 11(b)**.

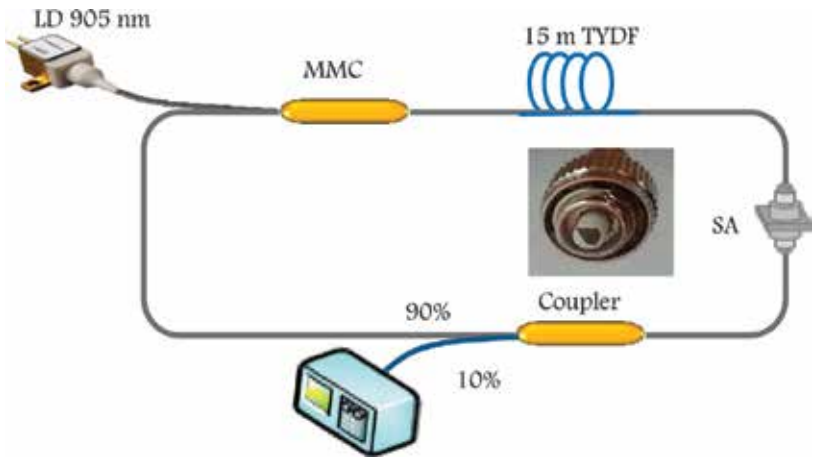

Figure 9. Setup of the proposed Q-switched TYDFL with MWCNT-PVA-based SA. Inset shows the image of the film attached onto a fiber ferule.

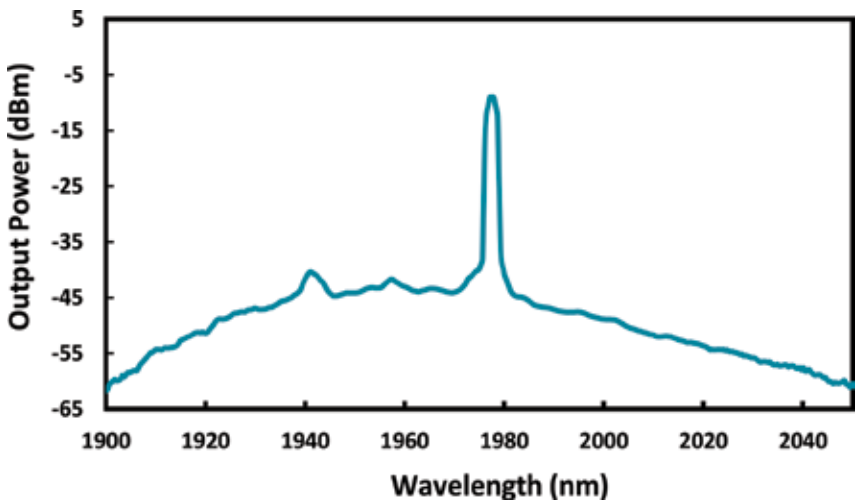

Figure 10. Output spectrum of the Q-switched TYDFL at pump power 1.6 W.

Figure 12 shows the pulse repetition rate and pulse width as a function of the pump power. As the pump power increases from 1.6 to 2.3 W, the repetition rate of the Q-switched pulses grows from 18.8 to 50.6 kHz. At the same time, the pulse duration significantly reduces from 8.6 to 1.0 μs as expected. The pulse duration could be further narrowed by optimizing the parameters, including shortening the cavity length, and improving the modulation depth of the MWCNT Q-switcher. An anomalous increase in the pulse width is observed at 1862 mW pumping, attributed to fiber nonlinearities [21].

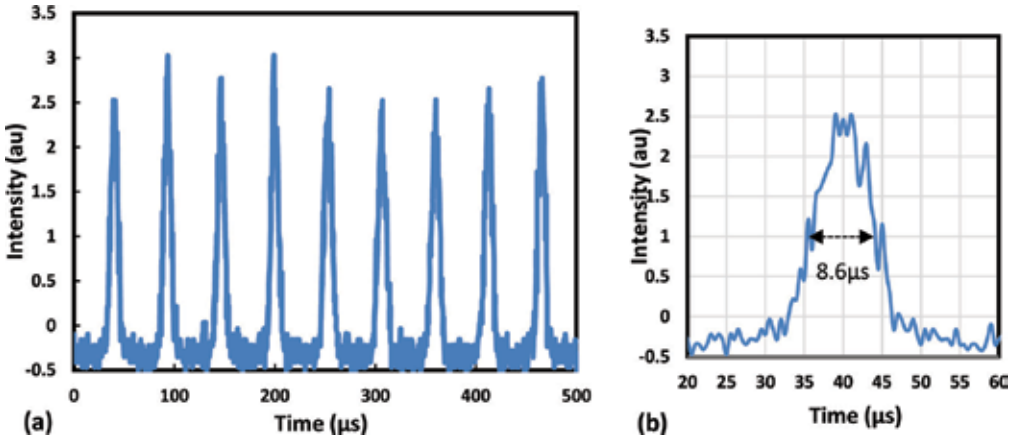

Figure 11. (a) A typical pulse trains and (b) a single pulse envelop of the proposed Q-switched TYFL at a pump power of 1.6 W. It shows a repetition rate of 18.8 kHz and a pulse width of 8.6 µs.

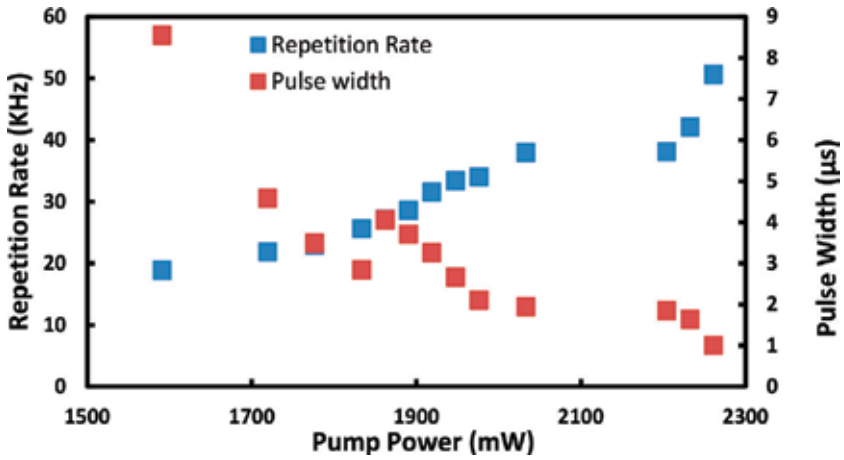

Figure 12. Repetition rate and pulse width as a function of 905-nm pump power.

3. Modelocked TYDFL using graphene PVA film as a saturable absorber

Modelocked Thulium-doped fiber lasers (TDFLs) have attracted intense interest in recent years for a number of potential applications, including atmospheric measurements, material processing, communication, laser radar, biomedical and medical applications, and longer-wavelength laser pumping [22–24]. The graphene PVA film was prepared by mixing the graphene solution in PVA solution. The graphene solution was obtained from the flakes produced using electrochemical exfoliation process. A free-standing graphene PVA film was obtained after drying in an oven and is used as SA.

3.1. Configuration of the proposed modelocked TYDFL

Experimental setup for the Thulium-Ytterbium co-doped fiber laser (TYDFL) is shown in **Figure 13** [1]. It uses a double clad Thulium-Ytterbium co-doped fiber (TYDF) as the lasing medium in ring cavity configuration. The TYDF has an octagonal inner cladding to enhance the pump light interaction with the doped core. The core has 5.96-nm diameter with an NA of 0.23. The selected fiber length of 10 m provides more than 90% pump absorption. The fiber type SA

device was constructed by inserting graphene PVA film between two ferules. The length of total cavity is set at around 17 m, so that the net cavity dispersion is anomalous for facilitating self-starting mode locked laser.

3.2. Modelocking performance of the TYDFL

Modelocking was self-started by increasing the pump power above the threshold of 1487 mW. The modelocked operation was maintained as the pump power is increased up to the maximum power of 1964 mW. **Figure 14** shows the output spectrum of the modelocked pulse train when the pump power is fixed at 1610 mW.

As shown in the figure, the spectrum was centered at 1942.95 nm with a 3-dB bandwidth of 0.08 nm. Without SA, the CW laser operates at 1943.50 nm. This shift of the operating wavelength toward the shorter wavelength is caused by the change in cavity loss by the insertion of SA [1]. Usually, lasers shift toward the shorter wavelength to acquire more gain to compensate for the insertion loss of SA. Moreover, the presence of weak sideband at 1942.5 nm confirms the existence of soliton as shown in **Figure 14**. The presence of conventional soliton confirms that the laser is operating in anomalous dispersion regime.

The typical pulse train of the passively mode-locked TYDFL at pump power of 1627 mW is shown in **Figure 15** [1]. The observed repetition rate is 11.76 MHz with a pulse-to-pulse

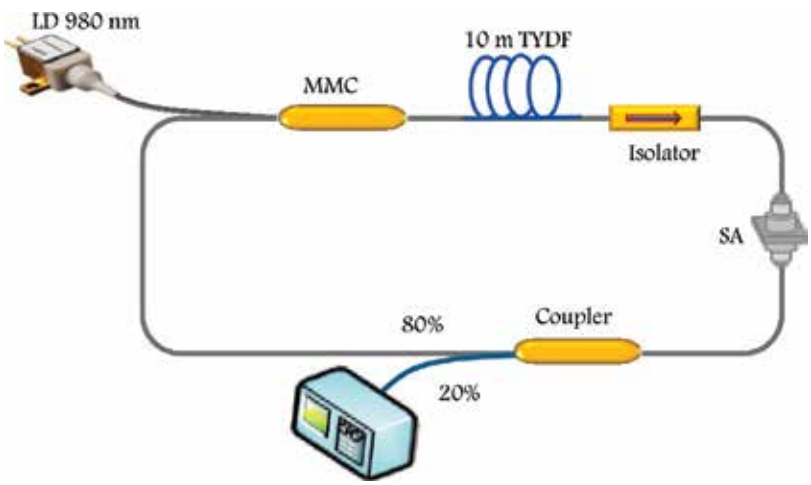

Figure 13. The schematic setup of the modelocked TYDFL employing the fabricated graphene PVA film-based SA.

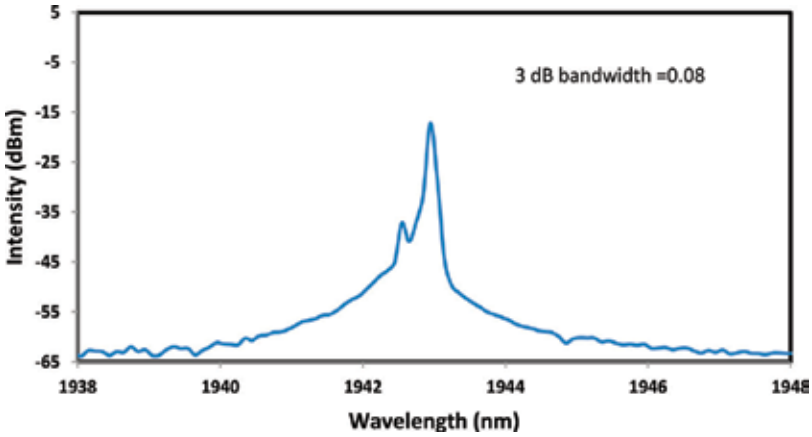

Figure 14. Output spectrum of the modelocked TYDFL.

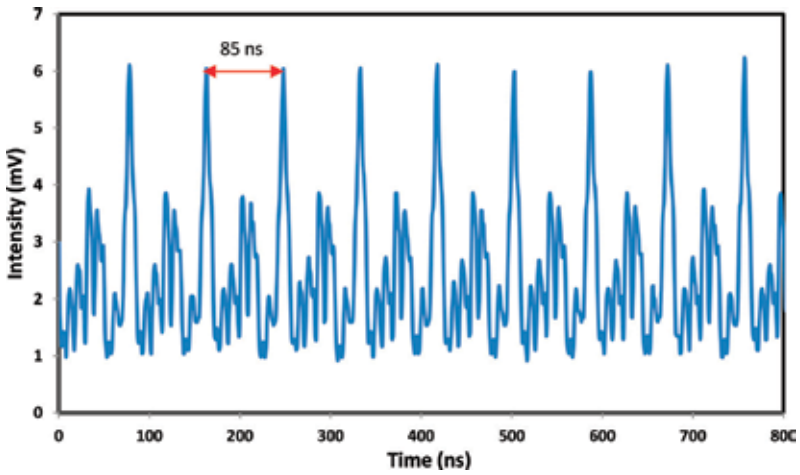

Figure 15. Typical pulse train for the modelocked TYDFL at a pump power of 1627 mW.

separation of 85 ns, which is in accordance with the cavity round trip time of a cavity length of 17 m. Thus, the well dispersed graphene in the PVA film exhibits sufficient saturable absorption for modelocking operation.

Figure 16 shows the repetition rate against the pump power. It is found that the repetition rate remained fixed at 11.76 MHz as the pump power increases from 1487 to 1964 mW [1]. The temporal analysis shows that the pulse width of the laser should be less than 9 ns. It is expected that the actual pulse width is much smaller than 9 ns, but due to the limitations of the oscilloscope resolution, it could not be accurately measured.

The total length of the laser cavity is about 17 m, and it consists of 10 m long TYDF and 7 m long single mode fiber (SMF) [1]. The estimated dispersions for TYDF and SMF are −0.083 and −0.034 ps^2/m, respectively, at 1943 nm. Therefore, it is expected that this modelocked

fiber laser operates in an anomalous dispersion regime. Moreover, the pulse width can be measured using an autocorrelator or can be calculated mathematically using time bandwidth product (TBP). Since an autocorrelator in the 2-μm range is not available, it is calculated mathematically by considering TBP of about 0.315 for $sech^2$ pulse profile. Since the 3 dB bandwidth of the optical spectrum is about 0.075 nm (5.96 GHz), the minimum possible pulse width is estimated about 52.85 ps. In addition, the repetition rate of the pulsed laser is also calculated by using the formula c/1.5 L, which gives a value of 11.76 MHz. This is in agreement with the observed repetition rate of this laser as shown in **Figure 16**. Single pulse energy is also calculated at various pump powers by using the measured values of output power of the laser. A maximum output power of 14 mW is observed at 1750-mW pump power. A linear increase in pulse energy is observed up to a pump power of 1750 mW, and with further increase in pump power, it decreases because of energy converted to noise as shown in **Figure 17**. The calculated pulse energy is in the range of 756.048–1190.476 pJ.

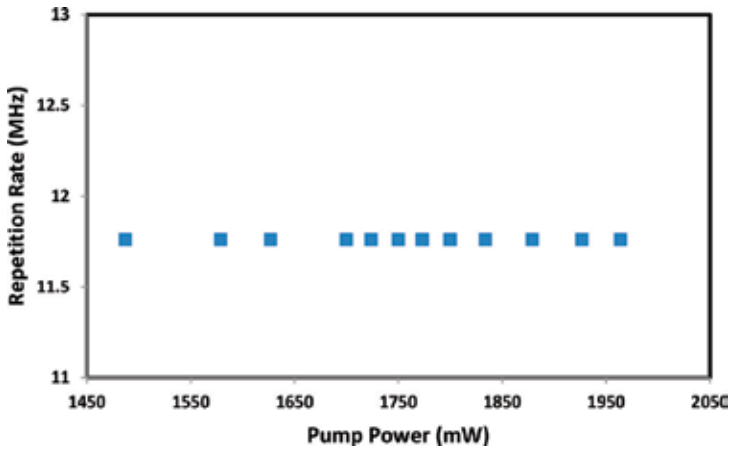

Figure 16. Repetition rate of the modelocked laser at various pump powers.

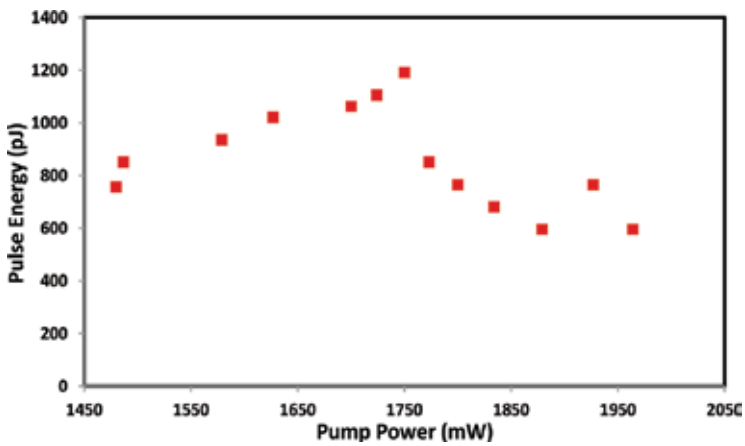

Figure 17. The calculated pulse energy against the input pump power.

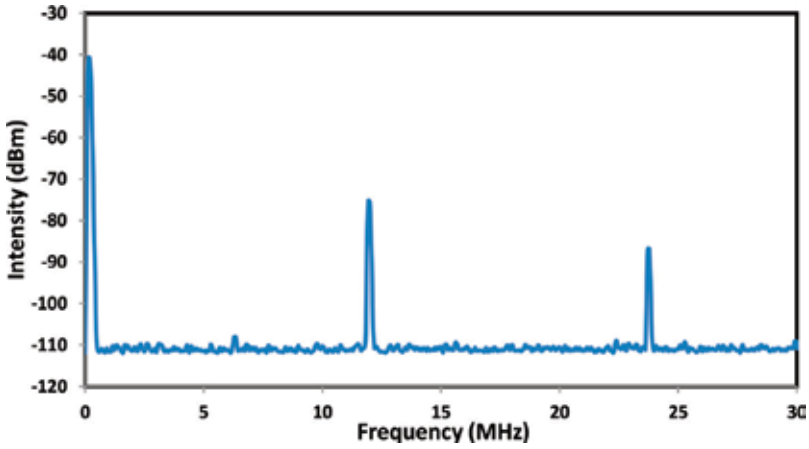

Figure 18. RF spectrum of the modelocked TYDFL.

The RF spectrum of the modelocked pulses is also measured, and the result is shown in **Figure 18**. Its fundamental mode peak locates at a frequency of 11.76 MHz and has an SNR of 36.5 dB, which confirms the stability of the modelocking operation [25].

4. Summary

This chapter describes some of the basic concepts regarding optical fibers and dynamics of Q-switched and modelocked fiber lasers with the help of the existing literature. It includes the description of double clad fiber structure and cladding pump technique. Later, it presents some details about Q-switching and its types. It also includes a detailed description of modelocked lasers, especially, passive modelocked lasers along with a brief introduction of solitons, which are an integral part of the most modelocked fiber lasers. Moreover, examples of Q-switched and modelocked fiber lasers are presented by using double clad Thulium-Ytterbium co-doped fiber. A cladding pump technique is employed with a 980-nm multi-mode laser diode. The Q-switched pulses are produced by using a saturable absorber fabricated with MWCNT-PVA film, while modelocked pulses are generated with the help of graphene-PVA film. The Q-switched laser is produced with a repetition rate in the range 18.8–50.6 kHz, whereas the modelocked laser generates pulses with a repetition rate of 11.76 MHz.

Author details

Babar Ibrahim Muhammad

Address all correspondence to: babarpksk@yahoo.com

Department of Physics, University of Karachi, Karachi, Pakistan

References

[1] Gafsi S. Highly Nonlinear Fiber Characterization for Mid-Infrared Applications. 2016

[2] Snitzer E, Po H, Hakimi F, Tumminelli R, McCollum B. Double clad, offset core Nd fiber laser. In: Paper Presented at the Optical Fiber Sensors; 1988

[3] Po H, Snitzer E, Tumminelli R, Zenteno L, Hakimi F, Cho N, Haw T. Double clad high brightness Nd fiber laser pumped by GaAlAs phased array. In: Paper Presented at the Optical Fiber Communication Conference; 1989

[4] Jeong Y, Sahu J, Payne D, Nilsson J. Ytterbium-doped large-core fiber laser with 1.36 kW continuous-wave output power. Optics Express. 2004;**12**(25):6088-6092

[5] Bedö S, Lüthy W, Weber H. The effective absorption coefficient in double-clad fibres. Optics Communications. 1993;**99**(5):331-335

[6] Sen R, Saha M, Chowdhury SD, Kumar N, Shekhar DP, Ghosh A, et al. High power fiber lasers: Fundamentals to applications. Science and Culture. 2015;**81**:319-326

[7] Upadhyaya B. High-power Yb-doped continuous-wave and pulsed fibre lasers. Pramana. 2014;**82**(1):15-27

[8] Früngel FB. Optical Pulses-Lasers-Measuring Techniques. NY, USA: Academic Press; 2014

[9] Taylor N. LASER: The Inventor, The Nobel Laureate, and The Thirty-Year Patent War. NY, USA: Simon and Schuster; 2002

[10] McClung F, Hellwarth R. Giant optical pulsations from ruby. Journal of Applied Physics. 1962;**33**(3):828-829

[11] Paschotta DR. Encyclopedia of Laser Physics and Technology, Q-Switching. https://www.rp-photonics.com/q_switching.html

[12] Webb CE, Jones JD. Handbook of Laser Technology and Applications: Laser Design and Laser Systems. Vol. 2. Boca Raton, FL, USA: CRC Press; 2004

[13] Ngo NQ. Ultra-Fast Fiber Lasers: Principles and Applications with MATLAB® Models. Boca Raton, FL, USA: CRC Press; 2016

[14] Digonnet MJ. Rare-Earth-Doped Fiber Lasers and Amplifiers, Revised and Expanded. 2nd ed. Vol. 395. NY, USA: Marcel Dekker, Inc.; 2001

[15] Fermann ME, Almantas G, Sucha G. Ultra Fast Lasers, Technology and Applications. New York, Basel: Marcel Dekker, Inc; 2003. pp. 27-29

[16] Agrawal GP. Nonlinear Fiber Optics. Fourth ed. Vol. 120. Academic Press; 2007

[17] Li D et al. Unidirectional dissipative soliton operation in an all-normal-dispersion Yb-doped fiber laser without an isolator. Applied Optics. 2015;**54**(26):7912-7916

[18] Lu B, Chen H, Jiang M, Chen X, Ren Z, Bai J. Graphene-based passive Q-switching for a 2 μm thulium-doped fiber laser. Laser Physics. 2013;**23**(4):045111

[19] Wang Q, Teng H, Zou Y, Zhang Z, Li D, Wang R, et al. Graphene on SiC as a Q-switcher for a 2 μm laser. Optics Letters. 2012;**37**(3):395-397

[20] Goze C, Vaccarini L, Henrard L, Bernier P, Hemandez E, Rubio A. Elastic and mechanical properties of carbon nanotubes. Synthetic Metals. 1999;**103**(1):2500-2501

[21] Babar IM, Sabran M, Harun SW, Ahmad H, Paul MC, Halder A, et al. Q-switched thulium-ytterbium co-doped fibre laser using newly developed octagonal shaped inner cladding double-clad active fibre and multi-walled carbon nanotubes passive saturable absorber. IET Optoelectronics. 2015;**9**(3):131-135

[22] Liu J, Wang Q, Wang P. High average power picosecond pulse generation from a thulium-doped all-fiber MOPA system. Optics Express. 2012;**20**(20):22442-22447

[23] Sorokina IT, Dvoyrin VV, Tolstik N, Sorokin E. Mid-IR ultrashort pulsed fiber-based lasers. IEEE Journal of Selected Topics in Quantum Electronics. 2014;**20**(5):99-110

[24] Polder KD, Bruce S. Treatment of melasma using a novel 1,927-nm fractional thulium fiber laser: A pilot study. Dermatologic Surgery. 2012;**38**(2):199-206

[25] Babar IM, Paul MC, Das S, Dhar A, Ahmad H, Harun SW. Mode-locked thulium ytterbium co-doped fiber laser with graphene saturable absorber. Photonics Letters of Poland. 2016;**8**(4):104-106

Section 2

Laser Applications

Chapter 3

Nonlinear Optical Response of Noble Metal Nanoparticles

Yachen Gao and Deigui Kong

Additional information is available at the end of the chapter

http://dx.doi.org/10.5772/intechopen.80841

Abstract

The special nonlinear optical response of noble metal nanoparticles (MNPs) when exposed to intense laser radiation has induced novel applications in nonlinear spectroscopy, optoelectronics, and optical switchers and limiters. In this chapter, recent results on the nonlinear optical properties of MNPs (including gold, silver, palladium, and platinum) have been discussed. Some specific optical nonlinear properties, such as nonlinear refraction, saturable absorption and reverse saturable absorption, two-photon absorption, and optical limiting, for femtosecond, picosecond, and nanosecond laser pulses, have been covered.

Keywords: metal nanoparticles, nonlinear absorption, nonlinear refraction, saturable absorption, reverse saturable absorption

1. Introduction

When the light is not strong, the optical response of a material usually scales linearly with the amplitude of optical electric field. However, at high optical powers, the optical properties of material will be changed more rapidly and are no longer linearly related to the intensity of the incident light. As result, nonlinear optical effects will occur. Nonlinear optics is the study of how intense light interacts with matter. The goal of nonlinear optics is mainly the investigation of the new phenomena and effects in the interaction process of strong laser and materials, including a deep understanding of the causes and the process regularity and their possible applications in the development of disciplines. Nonlinear optics has a great value and far-reaching scientific significance. In the past two decades, people have made significant progress in nonlinear optical materials. Many optical materials with fast nonlinear response

and large nonlinear properties have been used in various photonic and optoelectronic applications such as optical communication, optical information processing, optical data storage, pulsed laser deposition, and optical limiters.

Among various nonlinear effects, nonlinear absorption and nonlinear refraction attract more attention. Ultrafast nonlinear absorption properties are of importance since the nonlinearities considerably change the propagation of intense light through the medium, which can induce novel applications in optoelectronics, optical switchers, and limiters, as well as in optical computing, optical memories, and nonlinear spectroscopy. In fact, there is also much intrinsic interest in nonlinear refractive phenomena, particularly self-focusing and self-defocusing.

The search for new materials is one of the defining characteristics of modern science and technology. Of course, in nonlinear optics field, it is the case. Seeking and investigating new nonlinear optical materials with large nonlinear optical properties and fast nonlinear response is still one of the important works concerning nonlinear optics studies. Generally, the nonlinear optical materials should exhibit high transmission at normal light, so as not to degrade normal vision while exhibiting low or high transmission at intense light to serve as optical limiting materials for protecting human eyes and sensors or as saturable absorber for mode locking. In addition, nonlinear optical materials must exhibit fast response over a broad wavelength range and a high damage threshold.

The rapid development of nanoscience and nanotechnology has provided a number of new opportunities for nonlinear optics. A growing number of nanomaterials have been shown to possess remarkable nonlinear optical properties; this promotes the design and fabrication of nanoscale optoelectronic and photonic devices. Specially, metal nanoparticles (MNPs) have attracted considerable attention as potential nonlinear optical materials. Among them, gold and silver nanoparticles (NPs) have been paid more attention because they both exhibit a broad surface plasmon resonance (SPR) absorption band in the visible region of the electromagnetic spectrum [1–10].

In the following sections, the technologies used to measure the amplitude of nonlinear absorption and nonlinear refraction of nonlinear optical materials will be introduced. And some investigations concerning nonlinear optical properties of metal nanoparticles will be discussed.

2. Z-scan technique

There are several different methods for determining the nonlinear optical response of material. The most commonly used technology is Z-scan invented by Sheik-Bahae et al. [11, 12]. Z-scan is also one of the simplest experimental methods to be employed. Because Z-scan signal can provide information not only on the magnitude of optical nonlinearity but also on its sign, the use of the Z-scan technique for nonlinear optical measurement is increasing.

The typical Z-scan setup is shown in **Figure 1**, where the lens L is used to focus the laser beam, and the smallest section of the beam crosses at the 0 point of the Z axis. O stands for the test sample placed near the 0 of the Z axis. BS is a splitter, which splits the laser into two beams.

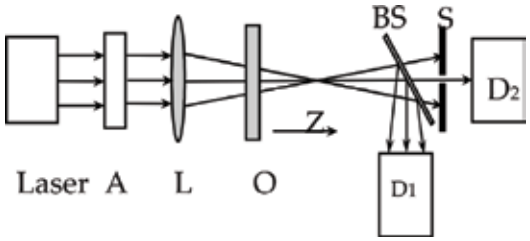

Figure 1. Setup of the Z-scan technique.

S is a small aperture used for the measurement of nonlinear refraction. D1 and D2 are photodetectors. During the test, the object to be tested moves along the Z axis, and the relationship between the light intensity and Z value is recorded.

When there is no aperture before photodetector D_1, Z-scan measurement is called open aperture Z-scan, which can provide the information about the nonlinear absorption. When there is an aperture before photodetector D_2, Z-scan measurement is called closed aperture Z-scan, which can provide the information about the nonlinear refraction of materials.

2.1. Open aperture Z-scan technique

When studying the materials' nonlinear absorption such as saturable absorption (SA) and reverse saturable absorption (RAS), we need to use open aperture Z-scan technique. Normalized open aperture Z-scan data is insensitive to beam distortion and is only a function of nonlinear absorption.

In the case of SA, the nonlinear absorption coefficient may be written as:

$$\alpha(I) = \frac{\alpha_0}{1 + (I/I_s)} \tag{1}$$

where α_0 is the linear absorption coefficient, I is the excitation intensity, and I_s is the saturation intensity. It is assumed that two-photon absorption (TPA) does not take place simultaneously with SA. The transmitted intensity is obtained from the equation:

$$\frac{dI}{dz} = -\alpha I \tag{2}$$

Here, z corresponds to the sample thickness. As shown in **Figure 2**, saturation intensity I_s can be obtained by fitting the experimental curve according to Eqs. (1) and (2). When materials show only RSA or TPA, according to open aperture Z-scan theory, the normalized transmission can be expressed as [12]:

$$T(z) = \sum_{m=0}^{\infty} \frac{[-q_0(z)]^m}{(m+1)^{3/2}} \approx 1 - \frac{\beta I_0 L_{eff}}{2\sqrt{2}(1 + z^2/z_0^2)} \tag{3}$$

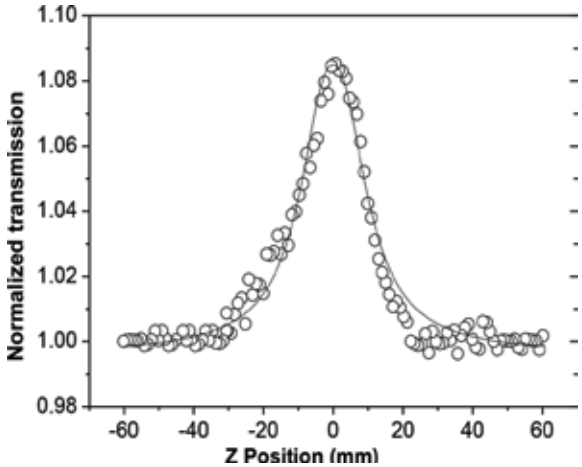

Figure 2. Theoretical and experimental result of the open aperture Z-scan for SA.

where β is the nonlinear absorption coefficient, I_0 is the on-axis peak intensity at the focus, $L_{eff} = (1 - e^{-\alpha_0 L})/\alpha_0$, L_{eff} is the effective interaction length, α_0 is the linear absorption coefficient, z is the longitudinal displacement of the sample from the focus ($z = 0$), L is the sample length, and z_0 is Rayleigh diffraction length. From Eq. (3), nonlinear absorption coefficient β can be obtained to be:

$$\beta = 2\sqrt{2}[1 - T(z = 0)]/I_0 L_{eff} \tag{4}$$

Selectively, as shown in **Figure 3**, β can also be obtained by fitting the experimental curve.

But when materials show transformation from SA to RSA, a nonlinear absorption coefficient including SA coefficient and TPA coefficient should be defined as [13]:

$$\alpha(I) = \frac{\alpha_0}{1 + (I/I_s)} + \beta I \tag{5}$$

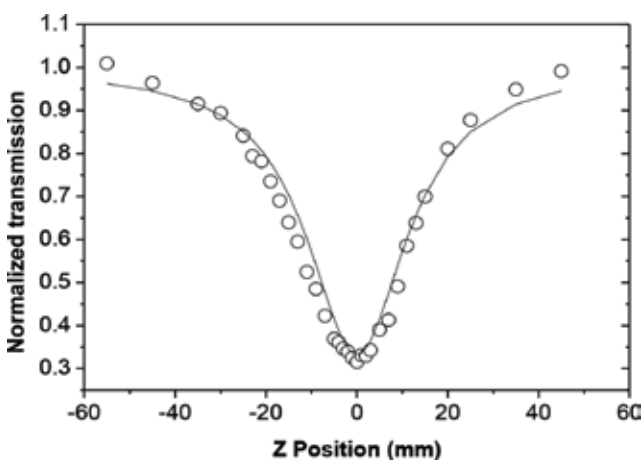

Figure 3. Theoretical and experimental result of the open aperture Z-scan for RSA.

where α_0 is the linear absorption coefficient, I is the laser intensity, I_S is the saturation intensity, and β is the nonlinear absorption coefficient. The transmission of material can be deduced to be:

$$T = 1 - \left(\frac{\alpha_0}{1 + \frac{I_0}{(1 + z^2/z_0^2) I_s}} + \frac{\beta I_0}{1 + z^2/z_0^2} \right) L \tag{6}$$

So normalized transmission can be obtained to be $T_N = T/T_0$. As shown in **Figure 4**, I_S and β can be obtained by fitting experimental data.

2.2. Closed aperture Z-scan technique

When the nonlinear refraction of materials needs to be obtained, closed aperture Z-scan experiments should be conducted. The normalized transmission of closed aperture Z-scan data can be expressed as [11]:

$$T(z) = 1 + \frac{4V \phi_0 x}{(x^2 + 1)(x^2 + 9)} \tag{7}$$

where $\Delta\phi_0 = k\Delta n_0 L_{eff}$, $k = 2\pi/\lambda$ is wave vector, $\Delta n_0 = n_2 I_0$, n_2 is nonlinear refractive index, I_0 is the on-axis peak intensity at the focus, $L_{eff} = (1 - e^{-\alpha_0 L})/\alpha_0$, L_{eff} is the effective interaction length, α_0 is the linear absorption coefficient, z is the longitudinal displacement of the sample from the focus (z = 0), L is the sample length, and z_0 is Rayleigh diffraction length.

The difference between normalized peak and valley in closed aperture Z-scan curve is $\Delta T_{P-V} = 0.406 (1 - S)^{0.25} |\Delta\phi_0|$, and S is aperture transmittance. The nonlinear refractive index values can be obtained to be:

$$n_2 = \frac{\alpha_0 \Delta T_{p-v}}{0.406 k I_0 (1 - S)^{0.25} (1 - e^{-\alpha_0 L})} \tag{8}$$

As shown in **Figure 5**, by fitting the experimental data using Eqs. (7) and (8), nonlinear refraction index of samples n_2 can be obtained.

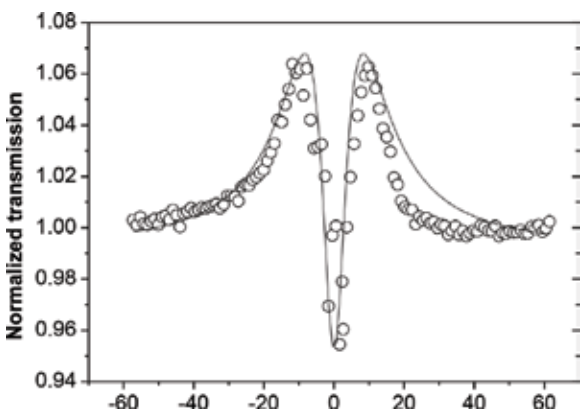

Figure 4. Normalized transmission as a function of position for open aperture Z-scan.

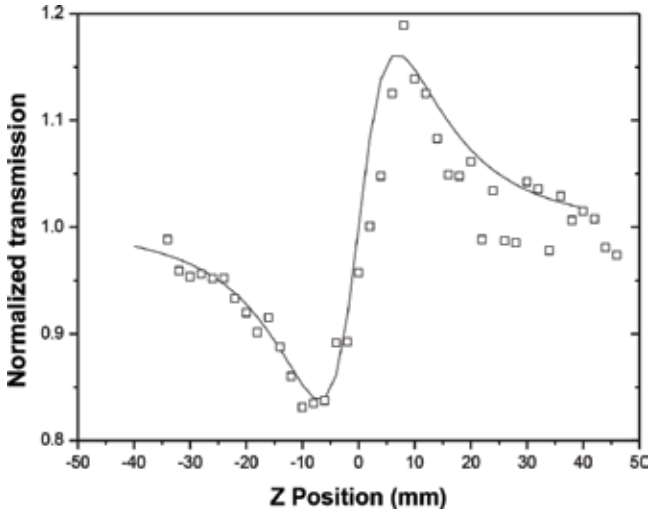

Figure 5. Normalized transmission curves of Z-scan data with an aperture divided by those without an aperture.

3. Nonlinear optical properties of metal nanoparticles

The stability combined with a large third-order susceptibility and ultrafast response means that metal nanoparticles are very promising materials for the creation of photonic devices. SPR is the main characteristics of metal nanoparticles, which strongly depend on the size, shape, and type of metal nanoparticles and the dielectric parameter of surrounding environments [14]. A huge enhancement of the nonlinear optical response in random media with metal nanoparticles is often associated with optical excitation of the SPR. Typical three metals having plasmon band in visible range are Au, Ag, and Cu. In contrast, metals such as Pt, Pd, and Cr show SPR in the wavelengths shorter than 300 nm. Therefore, large transparency and low propagation losses in the visible and infrared range are expected in Pt, Pd, and Cr nanoparticles. In many studies, composite materials with metal nanoparticles were fabricated by various methods and then generally studied using lasers operating at frequencies corresponding to the spectral range of the SPR, as listed in Ref. [15]. The review [15] has summarized the development of nonlinear optical random metal-dielectric composites based on metal nanoparticles synthesized by ion implantation.

Among the nanoparticles of noble metals, Au and Ag nanoparticles have attracted more interest and initiated more theoretical and experimental studies [1, 2, 16–31], as they both show a strong SPR band in the visible region. Moreover, their SPR absorption band can be tuned across the entire visible spectra by changing the size and shape of nanoparticles. The SPR of metal nanoparticles can lead to many interesting optical properties. For example, ultrafast nonlinear optical absorption is important since it can considerably alter the propagation of intense light in the medium, which can make metal nanoparticles be applied in optoelectronics, optical limiters and switchers, as well as in optical memories, optical computing, and nonlinear spectroscopy.

3.1. Nonlinear optical studies of Au nanoparticles

The first experimental results on the nonlinear optical effects of Au nanoparticle were obtained by Ricard et al. in 1985 [32]. They prepared the Au nanoparticle with an average diameter of 10 nm and measured the third-order nonlinear susceptibility using phase conjugation to be 1.5×10^{-9} esu at 530 nm. They traced the enhancement to the nonlinearities of the electrons in Au particles.

Among all composite materials, those made out of gold NPs embedded in a dielectric matrix are more important, because of their strong SPR absorption band in the visible region [33]. The coexistence of unique linear and nonlinear (especially third-order) optical properties makes the material be well suited for the potential applications ranging from optical limiter [20, 34], quantum information processing [35, 36], cancer treatment [37–39], on to all-optical switching [33, 40, 41]. In this direction, Au NPs embedded in dielectric media have been widely put more attention for their SPR, which depends strongly on the NPs environment and geometry [42].

Many investigations were performed in Au nanoparticles to study the nonlinear refractive index and nonlinear absorption [2, 16–22]. Moreover, the optical limiting of Au nanoparticles has also been studied widely for protection of human eyes and optical devices from laser damage. The contents studied mainly include the effects of sizes, matrices, and shapes on the nonlinear optical properties in Au nanoparticles [43].

Sánchezdena O et al. studied the size dependence of nonlinear optical response in Au metallic nanoparticles with diameters of 5.1, 13.4, and 14.2 nm synthesized and embedded in sapphire by using ion implantation [43]. Under 532-nm, 26-ps pulses, they found that the Au NPs exhibited a negative nonlinear absorption, which increases with size and size-independent positive nonlinear refraction.

For larger Au nanoparticles than those above, a systematic study of the size-related nonlinear optical properties of triangular Au particles was performed by S.H. Yoon et al. who fabricated the triangular Au nanoparticle arrays with four larger sizes of 37, 70, 140, and 190 nm on SiO_2 substrates using nanosphere lithography [44]. **Figure 6** shows the absorption spectra of the Au nanoparticles of different sizes. It can be seen that the SPR absorption peaks lie at 552, 566, 580, and 606 nm for the 37, 70, 140, and 190 nm Au nanoparticles, respectively. With the increasing particle size, the absorption peak shifts to longer wavelength.

Figure 7 shows the typical OA Z-scan experiment results of the four samples. The curve of the 37-nm sample showed a TPA with an additional SA component. For the samples with size of 70 and 140 nm, TPA component turned weaker and SA became dominant. The curve of the 190-nm sample showed only the SA component. These differences occur because the absorption in the excitation region is much weaker than that at 400 nm for the Au nanoparticles sized 37 nm, and herein, the interband transition to the TPA process plays a key role. However, the absorption at 800 nm is larger than that at 400 nm for the 190-nm Au nanoparticles; this is because the SA process becomes dominant. The curves of the samples of 70 and 140 nm showed a transition in this variation of the two nonlinear mechanism contributions.

Figure 8 shows the CA Z-scan data for four Au nanoparticles of 37, 70, 140, and 190 nm. For the 37 and 70 nm Au nanoparticles, a self-defocusing occurs, and the nonlinear refraction index

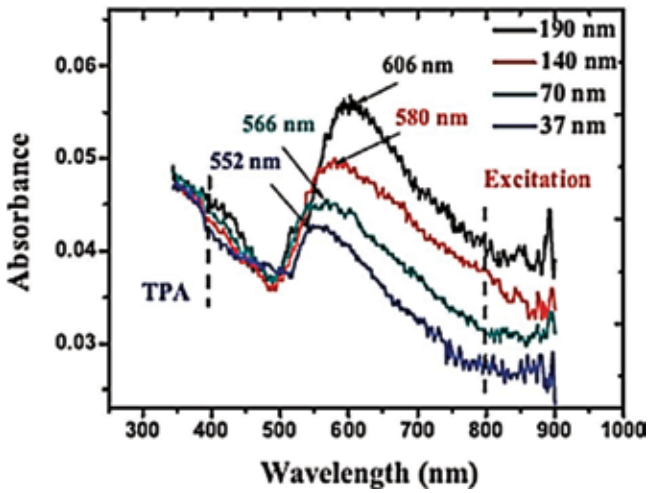

Figure 6. Absorption spectra of Au periodic particle arrays with sizes of 37, 70, 140, and 190 nm.

decreases due to the dominant interband transition caused by the TPA process. However, for the 140 and 190 nm Au nanoparticles, self-defocusing occurs. With the increase of particle size, the SA becomes dominant. The increase of refractive index is due to the excited electrons, resulting in the self-focusing.

It is obvious that the size of Au nanoparticles influences the nonlinear optical properties of Au nanoparticles. Hence, the optical limiting of Au nanoparticles should be size-dependent. Mostafavi et al. prepared gold nanoparticles with 2.5, 9, and 15 nm radii and studied the nonlinear optical response of resulting nanoparticles [8]. They found that the optical limiting threshold and the amplitude depend strongly on size. The 2.5-nm clusters do not limit light even at very high fluence, while the larger clusters do at 530 nm.

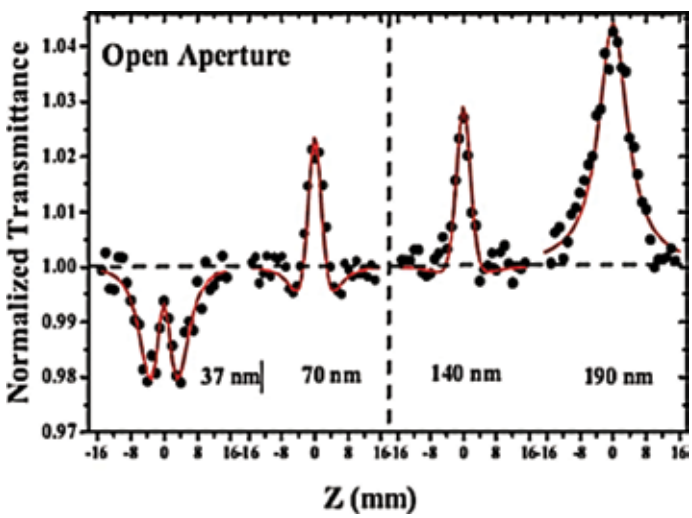

Figure 7. The OA Z-scan results of four samples with sizes of 37, 70, 140, and 190 nm.

http://dx.doi.org/10.5772/intechopen.80841

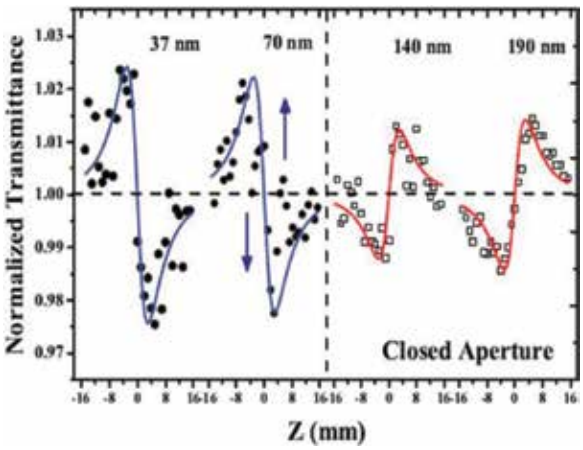

Figure 8. The CA Z-scan results of the four samples at exciting intensity $I\,0 = 55\ \ \mathrm{GW/cm\ 2}$.

But we believe that the increasing trend of optical limiting capability with size will terminate somewhere, and there should be an optimal size for optical limiting. To testify the hypothesis, we synthesized the gold nanoparticles with even larger radii of 15, 25, 50, and 70 nm and studied the optical limiting performance of the nanoparticles with different size at 532 nm for 8-ns laser pulses [45].

As shown in **Figures 9** and **10**, the optical limiting effect is found to be size-dependent. Compared with what Francois et al. have found [8], however, the results in our experiments are more complicated. When the size of gold nanoparticles increases from 15 to 25 nm, optical limiting capability increases. But when particle size increases further, optical limiting capability decreases instead. Visual description for the comparison of optical limiting ability is shown in **Figure 10**.

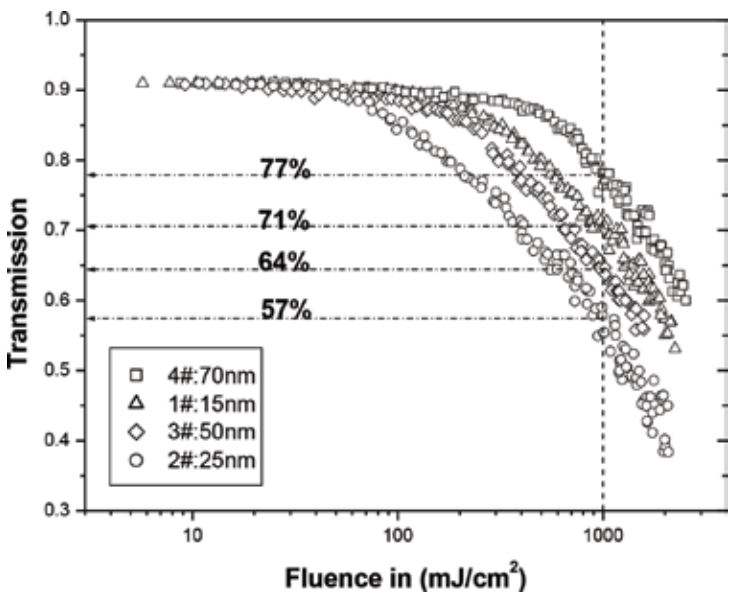

Figure 9. Optical limiting curves of gold nanoparticles with the radii of 15, 25, 50, and 70 nm.

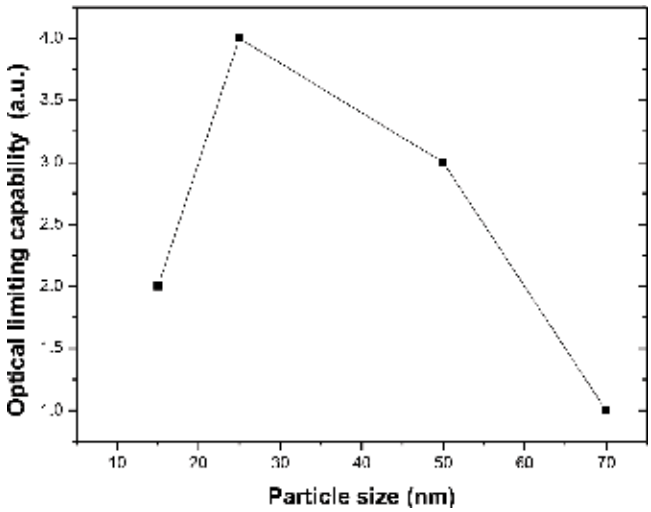

Figure 10. Optical limiting capability changing with particle size.

We analyzed the results in terms of the surface layer of nanoparticles. We assume that only surface layer of the particle can respond to outside light. We think of the thickness of the surface layer to be *ds*. The absorption region of gold nanoparticles with different sizes is shown in **Figure 11**. When gold nanoparticle has the radius less than *ds*, light energy can be absorbed by whole particle. Then, the absorbed energy transfers to surrounding solvent and leads to solvent bubbles. Moreover, the larger the size is, the stronger the nonlinear scattering is, and gold nanoparticles exhibit size-enhanced optical limiting. This is in consistent with the results in 15- and 25-nm gold nanoparticles. But when the radius of gold nanoparticle increases to be larger than *ds*, only outer layer *ds* can absorb light energy. The energy will first transfer to the core (black part in **Figure 11**) of gold nanoparticles. The transferring energy from gold nanoparticle to solvent decreases, which will obstruct the surrounding solvent to form bubbles. The obstruction makes the optical limiting weaker in larger particle.

Based on the analysis above, we found that, when the radius of nanoparticle is equal to the surface layer *ds*, the absorption-induced scattering is the strongest, correspondingly the optical limiting is most effective. That means, the optical limiting optimal size of metal nanoparticles equals to surface layer thickness *ds*. For gold nanoparticles, it is 25 nm. The investigation may be helpful for the synthesis of metal nanoparticles for optical limiting. Undoubtedly, more studies are required to find out the exact reasons for this behavior.

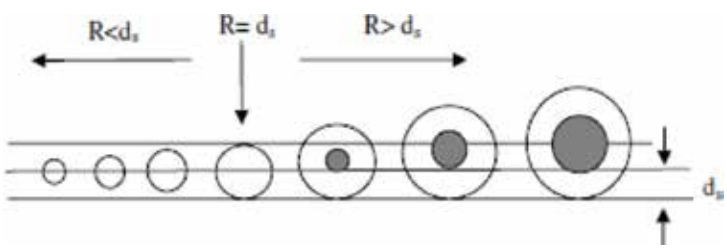

Figure 11. Absorption regions in gold nanoparticles with different sizes.

3.2. Nonlinear optical studies of Ag nanoparticles

For Au nanoparticles, there is significant overlap between the interband absorption and the plasmon resonance absorption, which decreases substantially the efficiency of plasmon excitation. In the case of Ag, however, the interband transition absorption at about 320 nm is far from its SPR wavelength of about 400 nm. This makes the plasmon excitation in Ag nanoparticles more efficient than that in Au nanoparticles. Moreover, the separation of two kinds of absorption facilitates the separate investigation of the nonlinear optical effects arising from interband transitions and those due to SPR. Hence, many groups conducted research on the nonlinear absorption and optical limiting in silver nanoparticles [1, 22–31].

For example, Gurudas et al. studied the picoseconds optical nonlinearity in silver nanodots prepared by pulsed laser deposition at 532 nm [22]. The nonlinear refraction and nonlinear absorption of these nanoparticle films were measured by using the Z-scan technique. The broad SPR absorption indicates that there are different-sized and different-shaped nanoparticles in the samples. At 532 nm, the SA and RSA are found to be dependent on sample properties. So by designing properly nanoparticles with different sizes and shapes, it may be possible to use these materials for various applications such as mode locking and optical limiter to protect sensors or eyes from the damage of high-power laser. Zheng et al. have investigated the shape-dependent NLO behaviors of nanostructured Ag nanoplates, nanowires, and nanoparticles suspensions (as shown in **Figure 12**) and their silica gel glass composites at both 532 and 1064 nm [23, 24] by using Z-scan.

NLO abilities of the nanostructured suspensions are found to be shape-dependent at 532 and 1064 nm. **Figure 13** shows the OA Z-scan experiment results of the nanostructured Ag in aqueous suspensions. All the samples exhibit typical RSA, but the deepness of the valleys differs from one to another, indicating different RSA abilities. As shown in **Figure 14**, they also investigated the NLO properties of the Ag/silica gel glass nanocomposites. In contrast to corresponding suspensions, the composites show more complicated OA Z-scan curves and the curves are insensitive to the nanostructured shapes. To a different extent, all the traces show

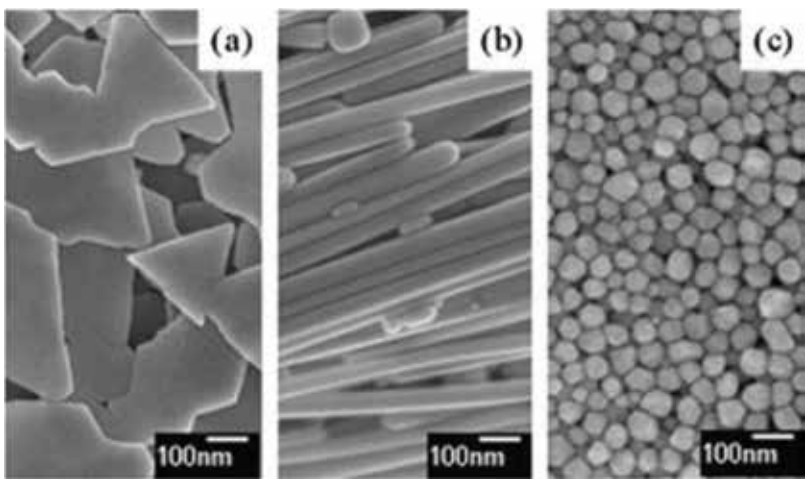

Figure 12. SEM images of the investigated Ag (a) nanoplates, (b) nanowires, and (c) nanoparticles.

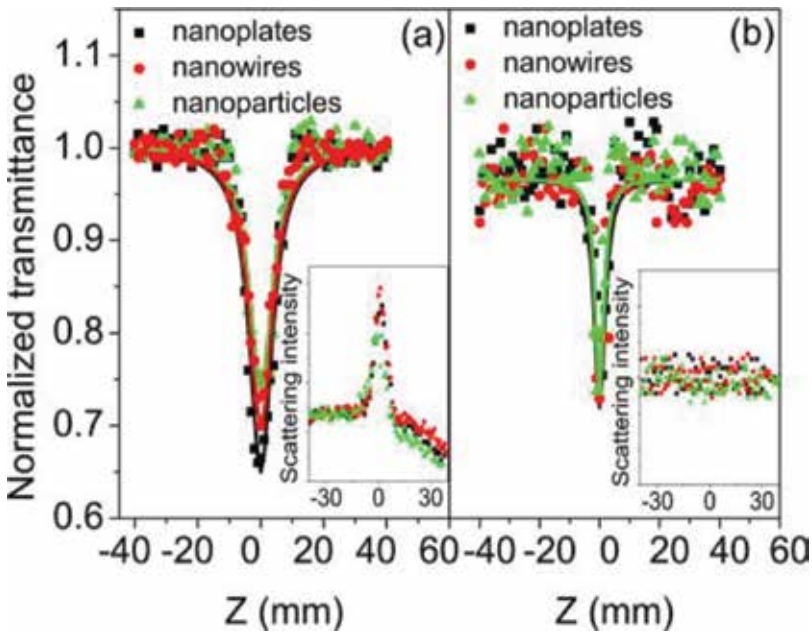

Figure 13. OA Z-scan curves of the investigated nanostructured Ag suspensions at 532 (a) and 1064 nm (b).

two symmetrical humps flanking the valley near the focus, where hump indicates SA and valley RSA. When the input energy increases gradually from 0.6 to 1.5 mJ, the NLA signals switch from SA to RSA. Besides, they have studied the NLO properties of Ag nanowire/silica

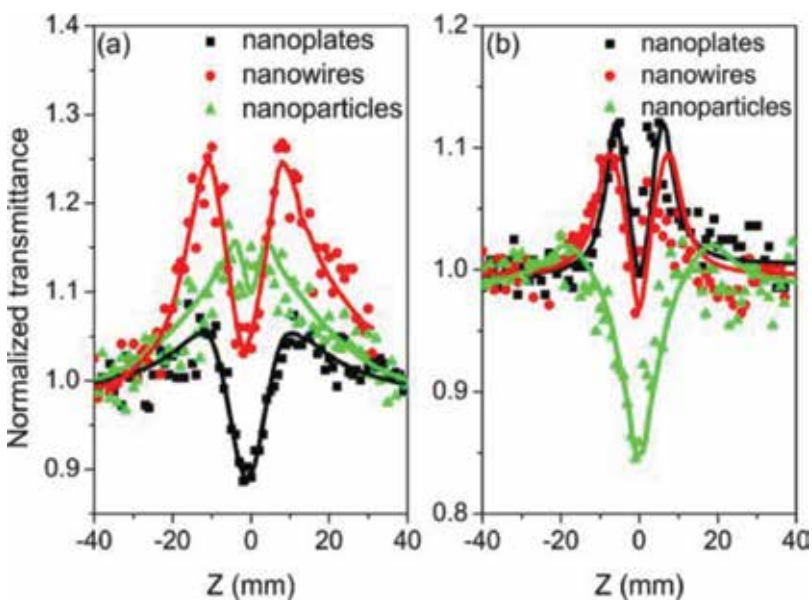

Figure 14. OA Z-scan curves of the investigated Ag/silica gel glass nanocomposites at 532 (a) and 1064 nm (b).

gel glass composite and Ag nanowires (NWs) suspension at both 532 and 1064 nm in Ref. [24]. In the Ag NWs suspension, only RSA is found, while in the Ag NWs/silica gel glass composite, a switch from SA to RSA is observed. The origin of this phenomenon was discussed from the viewpoint of electronic dynamics of Ag NWs in liquid and solid-state matrices. The solid-state environment of the gel glass composite greatly enhances the fluorescence of Ag NWs, retards the electronic relaxation process, and results in surface plasmon bleaching, which causes SA.

Unnikrishnan et al. studied nonlinear optical absorption in Ag nanosol at selected wavelengths of 456 nm (inside the SPR band), 477 nm (on the edge of SPR), and 532 nm (outside the SPR) using open aperture Z-scan technique [25]. They all found a flip over from SA to RSA behavior at higher input excitation. Similar switching behaviors have also been previously observed for Ag nanoparticles in ZrO_2 by Anija [26] and for Ag nanoparticles in PMMA by Deng [27] under nanosecond laser pulse at 532 nm.

All the above studies were conducted at 532 nm far from the SPR wavelength of 400 nm. While at resonant wavelength, Ganeev and Ryasnyansky have investigated the nonlinear optical absorption of Ag nanoparticles [28]. They found that Ag nanoparticles exhibit either SA for 1.2-ps pulsed laser or RSA for 8-ns pulsed laser. In fact, the nonlinear optical properties of materials depend strongly on wavelength and pulse width.

In 2012, we studied the nonlinear absorption of Ag nanoparticles using open-aperture Z-scan method with femtosecond laser pulses at 400 nm [29]. As shown in **Figures 15** and **16**, when laser intensities are relatively weaker, Ag nanoparticles show SA, but when laser intensities are strong, a switch from SA to RSA occurs. Moreover, when the repetition rate of pulse laser is high, open-aperture Z-scan curves become asymmetric. The switch and asymmetry were interpreted in terms of plasmon bleaching, free carrier absorption, and migration of Ag nanoparticles. The peak of the SPR of the Ag nanoparticles is at about 400 nm near the laser excitation. So the observed SA is due to the ground-state plasmon bleaching. It is the effect that causes an increase in transmission. When the laser intensity increases further,

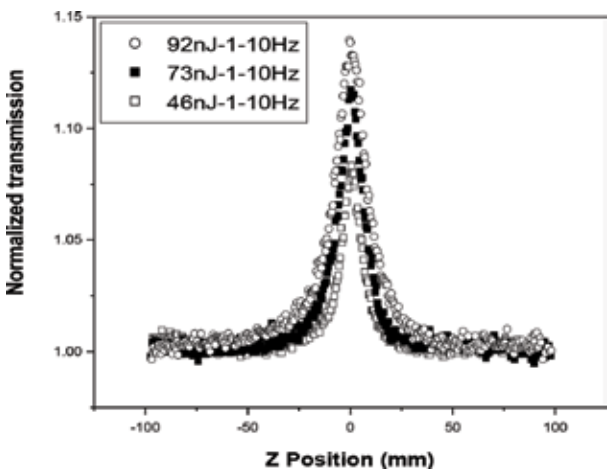

Figure 15. Open-aperture Z-scan curves at relatively low energies (46, 73, 92 nJ) using 1- and 10-Hz pulsed laser.

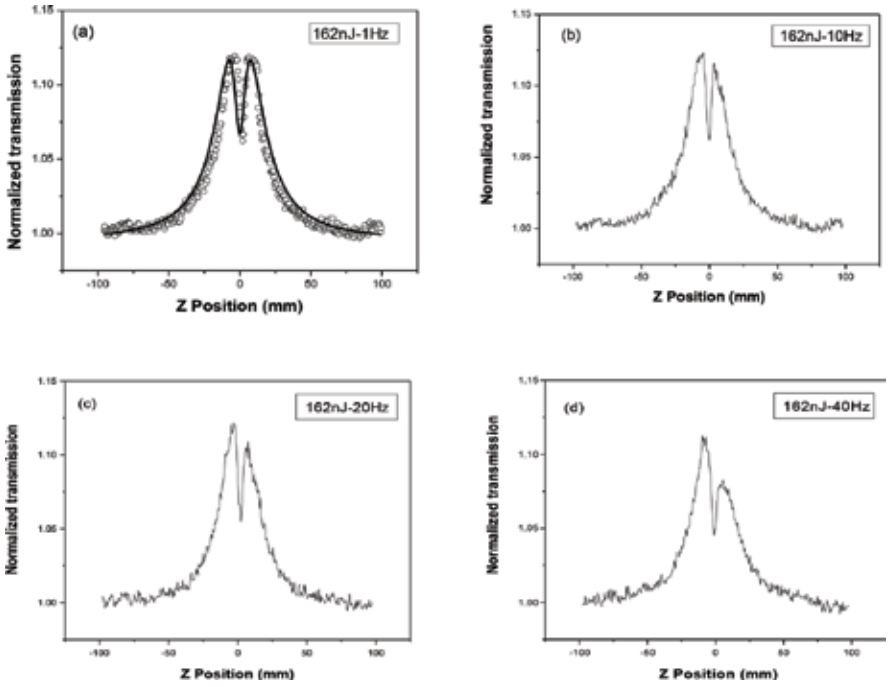

Figure 16. Open-aperture Z-scan curves obtained at energy of 162 nJ using (a) 1-, (b) 10-, (c) 20-, and (d) 40-Hz pulsed laser.

RSA begins to happen because the excitation can easily cause free carrier responsible for the RSA. This is a typical optical limiting effect, which can be applied to protect eyes and sensors from the damage of intense laser. Besides, asymmetrical open-aperture Z-scan curves were observed by using laser with higher repetition rate, which was thought to be due to the migration of nanoparticle following the impulsive optical excitation. More work is needed to study how laser causes the migration of nanoparticle and make a theoretical fit of the asymmetrical curves.

3.3. Nonlinear optical studies of Pd and Pt

It is well known, because both Au and Ag nanoparticles show a strong surface plasmon resonance (SPR) absorption band in the visible region, they have attracted more interest and initiated more theoretical and experimental studies concerning nonlinear optical properties. Though the SPR of transition metal nanoparticles is located in the ultraviolet range, the NLO response cannot be resonantly enhanced, but instead, it can be influenced by other nonlinear processes. Pd and Pt nanoparticles have also been found to exhibit interesting nonlinear optical properties such as two-photon or multiphoton processes [46–49], RSA [50] and SA [13, 51–53]. Correspondingly, Pt nanoparticles can be used in optical limiting [50, 53, 54] and mode locking [52, 53].

Even though platinum's SPR at 215 nm [55] lies away from excitation wavelength of 532 nm, as shown in **Figure 17**, we still observed SA at lower fluences, which is usually linked to SPR in gold nanoparticles [13]. Furthermore, as shown in **Figure 18**, we found the changeover from SA to RSA at higher input bump intensities.

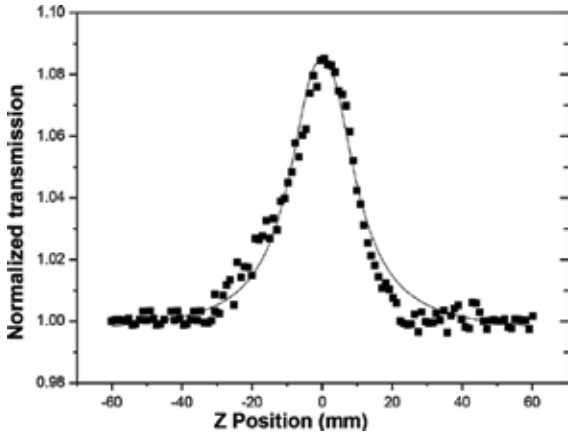

Figure 17. The normalized open-aperture Z-scan curve at lower fluences.

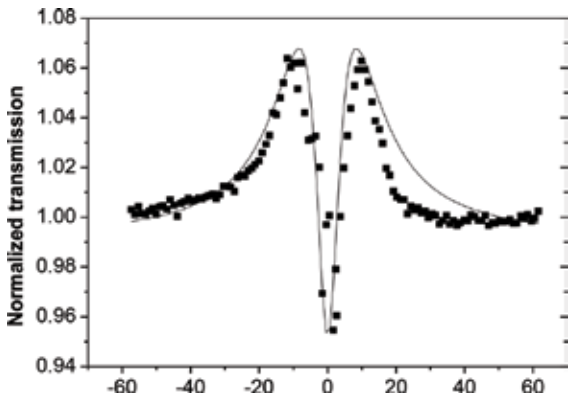

Figure 18. The normalized open-aperture Z-scan curve at higher fluences.

To interpret the flip of SA around the beam waist, we phenomenologically combine a saturable absorption coefficient and the two-photon absorption (TPA) coefficient, yielding the total absorption coefficient as shown by Eq. (5). Solid lines in **Figures 17** and **18** are the theoretical fitting. It can be found that the theoretical fit is in good agreement with the experimental results, indicating the model used is reasonable. For Pt nanoparticles, the SPR wavelength is at about 215 nm far from 532 nm, which implies that the ground plasma bleaching cannot occur in Pt nanoparticles. So we think that the SA in Pt nanoparticles has different origins from that in gold and silver nanoparticles and cannot be interpreted in terms of SPR. Although we have no ideal about the special phenomena, we think that Pt nanoparticles may be employed in not only optical limiting but also mode locking. In fact, the proposal has been proved by Qu and Ganeev et al.

4. Conclusions

In this chapter, nonlinear optical properties of metal nanoparticles were reviewed. Most of these studies were conducted in liquid matrices. However, from the viewpoint of practical

applications, it is important and indispensable to homogeneously disperse the nanostructured metals in solid-state matrices to avoid their easy agglomeration and instability in suspensions. In this case, investigation on NLO behaviors of metal nanoparticles in solid matrices becomes the most significant step toward the development of practical optoelectronic components and devices.

Conflict of interest

The author declares no competing financial interest.

Author details

Yachen Gao* and Deigui Kong

*Address all correspondence to: gaoyachen@hlju.edu.cn

College of Electronic Engineering, Heilongjiang University, Harbin, PR China

References

[1] Sun Y, Riggs JE, Rollins HW, Guduru R. Strong optical limiting of silver-containing nanocrystalline particles in stable suspensions. The Journal of Physical Chemistry. B. 1999; **103**(1):77-82

[2] Philip R, Kumar GR, Sandhyarani N, Pradeep T. Picosecond optical nonlinearity in monolayer-protected gold, silver, and gold-silver alloy nanoclusters. Physical Review B. 2000;**62**(19):13160-13166

[3] Anija M, Thomas J, Singh N, Sreekumaran Nair A, Tom RT, Pradeep T, et al. Nonlinear light transmission through oxide-protected Au and Ag nanoparticles: An investigation an nanosecond domain. Chemical Physics Letters. 2003;**380**:223-229

[4] Zhang H, David EZ, Deng LG, Liu HK, Teo BK. Optical limiting behavior of nanosized polyicosahedral gold-silver clusters based on third-order nonlinear optical effects. Journal of the American Chemical Society. 2001;**123**:11300-11301

[5] Ispasoiu RG, Balogh L, Varnavski OP, Tomalia DA, Goodson T. Large optical limiting from novel metal-dendrimer nanocomposite matericals. Journal of the American Chemical Society. 2000;**122**:11005-11006

[6] Shiliang Q, Chimin D, Song Y, Wang Y, Gao Y, Liu S, et al. Optical nonlinearities in gold nanoparticles protected by ligands. Chemical Physics Letters. 2002;**356**:403-408

[7] Gao Y, Wang Y, Song Y, Li Y, Qu S, Liu H. Strong optical limiting property of a novel sliver nanoparticle containing C60 derivative. Optics Communications. 2003;**223**:103-108

[8] Francois L, Mostafavi M, Belloni J, Delouis J-F, Delaire J, Feneyrou P. Optical limitation induced by gold clusters. 1. Size effect. The Journal of Physical Chemistry. B. 2000;**104**: 6133-6137

[9] Francois L, Mostafavi M, Belloni J, Delaire JA. Optical limitation induced by gold clusters. 2. Mechanism and efficiency. Physical Chemistry Chemical Physics. 2001;**3**:4965-4971

[10] Gao Y, Song Y, Li Y, Wang Y, Liu H, Zhu D. Large optical limiting of the [60]fullerene-substituted tripyridine palladium nanoparticles. Applied Physics B. 2003;**76**:761-763

[11] Sheik-Bahae M, Said AA, Van Stryland EW. High-sensitivity, single-beam n2 measurements. Optics Letters. 1989;**14**(17):955-957

[12] Sheik-Bahae M, Said AA, Wei TH, Hagan DJ, Van Stryland EW. Sensitive measurement of optical nonlinearities using a single bean. IEEE Journal of Quantum Electronics. 1990; **26**(4):760-769

[13] Gao Y, Zhang X, Li Y, Liu H, Wang Y, Chang Q, et al. Saturable absorption and reverse saturable absorption in platinum nanoparticles. Optics Communications. 2005;**251**(4-6): 429-433

[14] Hodak JH, Henglein A, Hartland GV. Tuning the spectral and temporal response in PtAu core–shell nanoparticles. Journal of Chemical Physics. 2001;**114**(6):2760-2765

[15] Zhang Y-x, Wang Y-h. Nonlinear optical properties of metal nanoparticles: A review. RSC Advances. 2017;**7**:45129-45144

[16] Elim HI, Yang J, Lee JY, Mi J, Ji W. Observation of saturable and reverse-saturable absorption at longitudinal surface plasmon resonance in gold nanorods. Applied Physics Letters. 2006;**88**(8):083107-083110

[17] Karthikeyan B, Anija M, Philip R. In situ synthesis and nonlinear optical properties of Au: Ag nanocomposite polymer films. Applied Physics Letters. 2006;**88**(5):053104-053107

[18] Wu DJ, Liu XJ, Liu LL, Qian WP. Third-order nonlinear optical properties of gold nano shells in aqueous solution. Applied Physics A: Materials Science & Processing. 2008;**92**(2): 279-282

[19] Polavarapu L, Xu QH. A single-step synthesis of gold nanochains using an amino acid as a capping agent and characterization of their optical properties. Nanotechnology. 2008; **19**(7):075601-075607

[20] Seo JT, Yang QG, Kim WJ, Heo J, Ma SM, Austin J, et al. Optical nonlinearities of Au nano particles and Au/Ag coreshells. Optics Letters. 2009;**34**(3):307-309

[21] Lee YH, Yan YL, Polavarapu L, Xu QH. Nonlinear optical switching behavior of Au nanocubes and nano-octahedra investigated by femtosecond Z-scan measurements. Applied Physics Letters. 2009;**95**(2):023105-023105

[22] Gurudas U, Brooks E, Bubb DM, Heiroth S, Lippert T, Wokaun A. Saturable and reverse saturable absorption in silver nanodots at 532 nm using picosecond laser pulses. Journal of Applied Physics. 2008;**104**(7):073107-073125

[23] Zheng C, Du YH, Feng M, Zhan HB. Shape dependence of nonlinear optical behavior of nanostructured silver and their silica gel glass composites. Applied Physics Letters. 2008; **93**(14):143108-143111

[24] Zheng C, Ye XY, Cai SG, Wang MJ, Xiao XQ. Observation of nonlinear saturable and reverse-saturable absorption in silver nanowires and their silica gel glass composite. Applied Physics B: Lasers and Optics. 2010;**101**(4):835-840

[25] Unnikrishnan KP, Nampoori VPN, Ramakrishnan V, Umadevi M, Vallabhan CPG. Non linear optical absorption in silver nanosol. Journal of Physics D: Applied Physics. 2003;**6**(11):1242-1245

[26] Anija M, Thomas J, Singh N, Sreekumaran Nair A, Tom RT, Pradeep T, et al. Nonlinear light transmission through oxide-protected Au and Ag nanoparticles: An investigation in the nanosecond domain. Chemical Physics Letters. 2003;**380**(1-2):223-229

[27] Deng Y, Sun YY, Wang P, Zhang DG, Jiao XJ, Ming H, et al. Nonlinear optical properties of silver colloidal solution by in situ synthesis technique. Current Applied Physics. 2008;**8**(1):13-17

[28] Ganeev RA, Ryasnyansky AI. Nonlinear optical characteristics of nanoparticles in suspensions and solid matrices. Applied Physics B: Lasers and Optics. 2006;**84**(1-2):295-302

[29] Gao Y, Wu W, Kong D, Ran L, Chang Q, Ye H. Femtosecond nonlinear absorption of Ag nanoparticles at surface plasmon resonance. Physica E: Low-dimensional Systems and Nanostructures. 2012;**45**:162-165

[30] Polavarapu L, Xu Q-H, Dhoni MS, Ji W. Optical limiting properties of silver nanoprisms. Applied Physics Letters. 2008;**92**(26):263110-263113

[31] Porel S, Venkatram N, Narayana Rao D, Radhakrishnan TP. Optical power limiting in the femtosecond regime by silver nanoparticle-embedded polymer film. Journal of Applied Physics. 2007;**102**(3):033107-033113

[32] Ricard D, Roussignol P, Flytzanis C. Surface-mediated enhancement of optical phase conjugation in metal colloids. Optics Letters. 1985;**10**(10):511-513

[33] Wang K, Long H, Fu M, Yang G, Lu PX. Intensity-dependent reversal of nonlinearity sign in a gold nanoparticle array. Optics Letters. 2010;**35**(10):1560-1562

[34] Philip R, Kumar GR, Sandhyarani N, Pradeep T. Picosecond optical limiting in monolayer protected cluster gold, silver and gold-silver alloy nanoclusters. Physical Review B. 2000;**62**:13160-13166

[35] Gisin N, Thew R. Quantum communication. Nature Photonics. 2007;**1**(3):165-171

[36] Li Y, Zhang S, Liu J, Zhang K. Quantum correlation between fundamental and second-harmonic field via second-harmonic generation. Journal of the Optical Society of America B: Optical Physics. 2007;**24**(3):660-663

[37] Hirsch LR, Stafford RJ, Bankson JA, Sershen SR, Rivera B, Price RE, et al. Nanoshell-mediated near-infrared thermal therapy of tumors under magnetic resonance guidance.

Proceedings of the National Academy of Sciences of the United States of America. 2003;**100**(23):13549-13554

[38] Lal S, Clare SE, Halas NJ. Nanoshell-enabled photothermal cancer therapy: Impending clinical impact. Accounts of Chemical Research. 2008;**41**(12):1842-1851

[39] Huang X, Neretina S, El-Sayed MA. Gold nanorods: From synthesis and properties to biological and biomedical applications. Advanced Materials. 2009;**21**(48):4880-4910

[40] Gibbs HM. Optical Bistability: Controlling Light with Light. London: Academic Press; 1985

[41] Midwinter JE. Photonics in Switching. London: Academic Press; 1993

[42] Noguez C. Surface plasmons on metal nanoparticles: The influence of shape and physical environment. Journal of Physical Chemistry C. 2007;**111**(10):3806-3819

[43] Sánchezdena O, Motasantiago P, Tamayorivera L, et al. Size-and shape-dependent nonlinear optical response of Au nanoparticles embedded in sapphire. Optical Materials Express. 2013;**4**(1):92-97

[44] Jun HS, Lee KS, Yoon SH, et al. 3rd order nonlinear optical properties of Au:SiO_2, nanocomposite films with varying Au particle size. Physica Status Solidi A: Applications and Materials Science. 2010;**203**(6):1211-1216

[45] Gao Y, Chang Q, Ye H, et al. Size effect of optical limiting in gold nanoparticles. Chemical Physics. 2007;**336**(2):99-102

[46] Papagiannouli I, Potamianos D, Krasia-Christoforou T, Couris S. Third-order optical nonlinearities of PVP/Pd nanohybrids. Optical Materials. 2017;**72**:226-232

[47] Iliopoulos K, Chatzikyriakos G, Demetriou M, rasia-Christoforou T, Couris S. Preparation and nonlinear optical response of novel palladium-containing micellar nanohybrids. Optical Materials. 2011;**33**:1342-1349

[48] Papagiannouli I, Demetriou M, Krasia-Christoforou T, Couris S. Palladium-based micellar nanohybrids: Preparation and nonlinear optical response. RSC Advances. 2014;**4**: 8779-8788

[49] Papagiannouli I, Chatzikyriakos G, Iliopoulos K, Demetriou M, Krasia-Christoforou T, Couris S. Palladium micellar nanohybrids with tunable nonlinear optical response. Optical Materials. 2014;**36**:123-129

[50] Qu S, Song Y, Liu H, Wang Y, Gao Y, Liu S, et al. A theoretical and experimental study on optical limiting in platinum nanoparticles. Optics Communication. 2002;**203**:283-288

[51] Ganeev RA, Suzuki M, Baba M, Ichihara M, Kuroda H. Low- and high-order nonlinear optical properties of Au, Pt, Pd, and Ru nanoparticles. Journal of Applied Physics. 2008; **103**(6):063102

[52] Ganeev RA, Tugushev RI, Usmanov T. Application of the nonlinear optical properties of platinum nanoaprticles for the mode locking of Nd:glass laser. Applied Physics B: Lasers and Optics. 2009;**94**(4):647-651

[53] Chehrghani A, Torkamany MJ. Nonlinear optical properties of laser synthesized Pt nanoparticles: Saturable and reverse saturable absorption. Laser Physics. 2014;**24**(1): 015901-015909

[54] Ganeev RA, Ryasnyansky AI, Kamalov SR, Kodirov MK, Usmanov T. Nonlinear susceptibilities, coefficients and refractive colloidal metals. Journal of Physics D: Applied Physics. 2001;**34**(11):1602-1611

[55] Henglein A, Ershov BG, Malow M. Absorption spectrum and some chemical reactions of colloidal platinum in aqueous solution. The Journal of Physical Chemistry. 1995;**99**: 14129-14136

Chapter 4

Laser Ablation Technique for Synthesis of Metal Nanoparticle in Liquid

Amir Reza Sadrolhosseini, Mohd Adzir Mahdi, Farideh Alizadeh and Suraya Abdul Rashid

Additional information is available at the end of the chapter

http://dx.doi.org/10.5772/intechopen.80374

Abstract

Recently, the synthesis and application of metal and ceramic nanoparticle are significant subject in science and engineering. The metal nanoparticles such as silver, gold, and copper nanoparticles have more application in material science, nanomedicine, electronic, photonic, and art. One of the green methods for preparation of metal nanoparticles is laser ablation technique that offers a unique tool for nanofabrication of nanoparticles. In this technique, the high-power laser ablates the metal plate and the nanoparticles are formed in the liquid. The properties of nanoparticles using laser ablation are unique, and they are not reproducible by any other method such as chemical methods. The important parameters to produce the metal nanoparticles are energy, wavelength, repetition rate of laser, ablation time, and absorption of an aqueous solution. Laser ablation is a simple method for fabricating the metal nanoparticles without surfactant or chemical addition. In this chapter, the mechanism of formation of metal nanoparticles in liquid, significant parameters for using the laser ablation technique to prepare the metal nanoparticles, and the preparation of silver, gold and copper nanoparticles will be reviewed.

Keywords: laser ablation, silver nanoparticles, gold nanoparticles, copper nanoparticles, mechanism of laser ablation in liquid, effect of wavelength in laser ablation, effect of temperature in laser ablation, laser ablation setup

1. Introduction

Green synthesis of metal nanoparticles in liquid solution is the regard issue in the nanotechnology and nanomedicine research. Gold, silver, and copper nanoparticles were prepared using physical and chemical methods based on chemical reaction or interaction of gamma-ray,

X-ray, or UV-ray with chemical material. Gold, silver, and copper nanoparticles have significant chemical, biological, and physical properties. They are anti-concern, anti-bacterial, and anti-inflammatory, and can improve the fluorescence properties of polymer composites. They are used to enhance the sensitivity and selectivity of biosensors based on conducting polymer. Hence, the green synthesis of metal nanoparticles is considerable in medicine and nanotechnology research. Laser ablation is a green and simple method for fabricating the metal nanoparticles without surfactant or chemical addition. Advantages of laser ablation technique are simplicity, the high purity of the nanoparticles, the ability to prepare variety metals and ceramics, and the in-situ dispersion of the nanoparticles in a variety of liquids [1]. Because the liquids have cooling effect and confinement effect and they cause the oxidation or reduction [2, 3] of particles. Metal nanoparticles have the plasmonic effect in the green and red part of the UV-visible spectrum due to scattering and absorb the photon. This effect depends on scattering cross section of metal nanoparticles which is higher than organic chromophores [4]. Some organic material can cap the metal nanoparticles [5]. Moreover, they have stable chemical and physical properties including high-temperature resistance, photo-irradiation, high acids or oxidation resistance [6–8], and catalytic properties [9, 10]. Therefore, the metal nanoparticles were used to enhance the response of biomaterial or organic material. Numerous methods including solution phase [11], photochemical [12], sonochemical [13], electrochemical synthesis [14], photolytic reduction [15], radiolytic reduction [16], solvent extraction reduction [17], microemulsion technique [18], polyol method [19], and microwave irradiation [20] were used to synthesize and disperse gold, silver, and copper nanoparticles in various mediums. These methods are based on chemical reaction or interaction of material with external field. Briefly, the photochemical method is based on absorption of light for conducting the chemical reaction. The sonochemical and microwave methods are based on concerned with application of ultrasound and microwave, respectively, for initiation of chemical reaction in liquid. Other methods, such as electrochemical synthesis photolytic reduction radiolytic reduction, solvent extraction reduction, microemulsion technique, and polyol methods, are based on chemical reaction in the liquids and reduction of another form of salted metals. But, laser ablation method is based on interaction of laser with metal plate and the nanoparticle formed and dispersed in the liquid.

Moreover, metal nanoparticles were dispersed into inorganic and organic materials including water [21], acetone [22], oil [23–26], chitosan [27], and PVA [28].

In this chapter, the significance of metal nanoparticle in art and life, the mechanism of laser ablation technique to form the nanoparticle in liquid, laser ablation setup, and the significant parameters of laser ablation for fabrication of metal nanoparticles are presented.

2. Nanomaterial influence in art and life

Nanomaterials and nanoparticles are involved in various applications such as sensor, catalysis, electronics, and plasmonic devices [5, 7]. The application of gold, silver, and copper nanoparticles is swiftly growing in biotechnology [5–8] to detect and recognize DNA and proteins [29]. They want to achieve the particular instrument and sensor for cancer diagnosis and cancer therapy [30].

Nanomaterials and nanoparticles have more application in medicine, industry, and art. The interface of art, science, and technology is nanotechnology. The effects of nanotechnology on art has been proven during Medieval perfectly, when artists unaware of this technology. The recent achievements of nanoparticles in the field of art have examined, and the techniques employed in the creation of works of art have been identified. These techniques include Medieval artisans were the first nanotechnologists. They made coloured glass or stained glass that are an important element in the ancient history and architecture [31]. The stained glass is attractive and multifunctional. On the other hand, Roman glass cage cup shows a verity of colors which are related to the direction of the light. When the light comes out from the back, it shows a red color, and it illustrates green color when the ligth reflects to different angle. Those stained glass and Roman glass cage cup [32] are attractive and multifunctional. They are good suggestion for dramatics phenomenon which have almost died, and there are no longer practices on the traditional theater stage. Artistic may give advantage to change modern performance of puppet show, which has been very popular in Malaysia as Wayang Kulit Kelantan. In addition, the stain glass windows may impact on the principle of performing the iconography, the visual images, and symbols used in the ceramic works of art and for interpretation of storytelling. Those traditional stories on ceramic works of art derived on the 'pictorial curtain' as a traditional Iranian play provided an opportunity for dramatizing situations that give way to mourning. Therefore, nanoparticles not only are able to revival some rituals but also can make a modern stage for those forgotten traditions.

The discussion on how to improve nanotechnology in science cannot be held without a general discussion on the impact of nanomaterial on human life. The impact of nano is felt in different areas, including music, particularly in the manufacturing of musical instrument, and visual art (Nanoforart), performing arts in specie in set design. More so, modern lifestyle has also experienced the introduction of nanotechnology in the production and supply of clothing and foods. Nanotechnology is regarded as a new, edge-cutting, and emerging technology with promising scientific advancement for the production of exceptional compact electronic devices, enhancing of food shelf life, medical advancement, and the production of unique cosmetics. More so, nanotechnology is a technology that is capable of enhancing the production of quality clothing, energy saving devices, and quality packaging that are capable of impacting daily living. It involves manipulating matter on near atomic scale for the production of new structures, systems, and devices [33]. Through this, healthy, efficient and sustainable systems can be created by combining science, art, and technology. In fact, the emergence of nanotechnology can be seen as the introduction of newer and more relevant topics than the ones that have gained much attention in time past, such as the techniques which were discovered by the Medieval artisans. The first nanotechnologists were the Medieval artisans who produced stained glass windows, which are significant elements of ancient history [34]. Recently, the field of art has experienced the use of nanoparticles for the production of nanowires for musical instruments such as photonic guitar. Reference to *materials by design:* the integration of proteins and music exposes the manner in which fiber rotation from proteins can be changed into music. Nanoparticles have properties that are important for use as biomaterials, for drug delivery, as composites of lightweight, and as functional coatings. Constructing hierarchical assemblies of less complex building blocks into architectures that are complex with superior properties is one of the emerging areas in the design of such materials. This approach is reviewed using a case study of silk, which is regarded as a

biomaterial that can be genetically processed and programmed. Silk inherently functions as a multipurpose protein fiber with hierarchical organization for the purpose of providing structural support, for eggs protection, and prey procurement. In addition, knowledge abstraction from the physical system enables the conversion of silk to a mathematical model through the use of category theory. This allows the translation of the mechanism of spinning fibers from protein into music, using a process which allocates a set of rules governing the system construction. The structure, properties, and mechanisms of the materials can be expressed in an entirely different domain, which is music. Science and art can be combined through the classification of structure-property relationships as a new way of creating new bioinspired materials by means of translating the mechanisms and structures from unique hierarchical systems within the framework of the integration of science and art through categorization of structure-property relationships presents a novel paradigm to create new bioinspired materials, through the translation of structures and mechanisms from distinct hierarchical systems and in the context of the inadequate number of building blocks that generally rules these systems [35]. The prototyped use of fiber strain sensors has been experienced in the area of music recording. Using this finding, a new use of low noise fiber optic strain sensors in music, especially in constructing a photonic guitar, is described in this article [36].

On the other hand, a novel category of nano-based products was developed by the FP7 projects known as MEMORI (Measurement, Effect Assessment and Mitigation of Pollutant Impact on Movable Cultural Assets—Innovative Research for Market Transfer) and NANOFORART (nanomaterials for the conservation and preservation of movable and immovable artworks); the European Union funded this project which are aimed at creating greener and safer protection from regular products. According to the EU, the beauty of artworks can be manifested through the cleaning and preservation of art, but the environment, in the long run, should not be damaged by the products and chemicals which will be used. The purpose of this project was to develop and protect cultural assets that are environmentally friendly, through the use of advanced materials and methods [37].

In order to safely clean and preserve art works, the various materials used in their creation must be uniquely adapted products of conservation. There are a number of limitations associated with the use of traditional products, and they include relying on hard-matter solvents, toxic materials, layers of incompatible coatings, or even causing damage to materials such as leather or paper, which are water-sensitive. According to the Baglioni, who is the project manager of EU, money could be saved through the use of Nanoforart's products. The project manager added that such works have longer lifespan than those developed using conventional materials and are safe enough for tourist sites not to be shut down during the work [38]. By modifying nanotechnology, the discovery of some techniques which can be used in cleaning products was made; all the methods had their own unique protection advantages which are described below:

1. Nanocontainers and micellar solutions, when compared to the conventional methods which are based on pure solvents, are better with faster performance and less health risk as well as ecotoxicity. This is as result of the use of pure organic solvents which make up less than 5% of the formulations with water being the major (95%) solvent component

of these formulations. The reduction of penetration into the immovable artwork's matrix of porosity with regard to that occurring with organic solvents is another advantage of systems that are water-based. This causes the avoidance of redissolution of polymer into the artifact. The NANOFORART project has progressed above the state-of the-art and developed into a technique for the production of new nanoparticle-based substance which can be used for plastering, stones, stucco, and wall paintings [39].

2. According to Giorgi et al. [40], it has been found that the acidity of paper can be neutralized using alcoholic dispersions of calcium and magnesium hydroxide nanoparticles. More so, this alcoholic dispersion can be used in generating carbonate alkaline reserve (after the reaction of the hydroxide with CO_2 from air) through which further degradation is prevented. There has been a positive response to this method. One of the major advantages of this method is that the penetration of nanosized particles into the paper fibers is enhanced alongside a rapid carbonation as a result of their high surface reactivity. Again, with this method, the stabilization of alkaline nanoparticles requires no surfactants. There is minimal catalytic activity of iron and copper when pH is close to being neutral. The implication of this is that a definite control of the acidity/alkalinity of paper can enhance the reduction in the rate of oxidation degradation by means of Fenton reactions (as cited in Baglioni et al. [37], p. 317) [40].

3. In addition, the toxicity and effect of the cleaning methods can appear through the use of pure organic solvents. The use of solvent gels, which was first advocated for in the 1990s, permits the solvent localization and, in some case, the decrease in penetration of solvent into underlying layers of paint. However, the removal of solvent gels as well as their residues from a paint surface is often difficult. This is one of the problems which will be addressed in the current proposal. They use precise quantities of clean liquid control directly, without damaging the image or leaving residues [41].

3. Laser ablation mechanism and metal nanoparticles formation

The mechanism of laser ablation depends on physical properties of metals and environment medium. Therefore, the ablation of metals is an intricate subject [42–44]. Ablation of metal target commences with the sorption of laser beam energy. When the laser beam interacts with the metal target, the heat can generate and the photoionization of the metal target can occur. After that, metal nanoparticles will be released from the metal plate as the different phase that depends on the absorbed energy E [42], and plasma plume expands [43–45]. Hence, if the duration of laser ablation is much higher than the laser pulse duration, the ablation depth (L_a) could be obtained as follows:

$$L_a \approx E^{\frac{2}{3}}, \quad t_a \approx E^{\frac{1}{2}}, \tag{1}$$

Where t_a, T_e, and t_1 are the time of the ablation process, the electronic temperature during the ablation process, and the laser pulse duration, respectively [6, 42].

In accordance prior report, when the energy of laser beam is high enough to generate a plasma plume, an acceptable ablation rate can be obtained. During laser ablation of metal plates, the plasma plume can be formed with the generation of photon and sound [46, 47]. This phenomenon is confined near the metal plate [44, 46, 47]. The face of the metal plate face in the plasma plume remains at high temperature and high pressure during the ablation of the metal plate [44, 46–48]. During the laser ablation of the metal plate, some thermodynamic phenomena occur near the metal target. Therefore, a face of the target in the plasma plume observes energy and the physical parameters are not constant on the whole target area [44, 49, 50]. Moreover, sometimes the deportation of particles from the metal targets due to photoionization [51]. So, the concentration and distribution of metal nanoparticles become large in the liquids by using the laser ablation of the metal plate [50]. The formation of metal nanoparticles based on laser ablation of the metal plate can be explained as bubbling of metal molecules [43, 44, 49]. Some physical properties including of size and concentration of nanoparticles in the liquid are a function of the phase homogeneity of the material released into the liquid during the irradiation of metal target. In accordance with the literature, the changes of morphology were observed around the ablated area on the surface of Au or Ag plates, when the high-power laser (110 fs to 800 nm) was used to ablate the gold and silver plate at different fluences [52]. The high-power laser with the fluence of 60 and 1000 J cm^{-2} can generate sharp and irregular craters [52]. Therefore, the variety of particle size and concentration of nanoparticles were achieved with different fluences [6, 50, 52, 53]. For example, the metal nanoparticles with small size have regular craters and low fluences [6, 50, 52]. The nanoparticles with the average size larger than 10 nm can generate the irregular craters and high fluences that related to boiling of metal plates [6].

The energy transfer to the electron on the surface of metal plates depends on the time duration of high power lasers such as femtosecond, picosecond, and nanosecond. It is time duration of laser ablation, and it is a significant factor for synthesis of nanoparticles. Hence, femtosecond laser pulses can release the electron from the metal plates faster than the thermal action of electron-photon phenomena. But, picosecond and nanosecond laser pulses can transfer the energy on a time scale longer than femtosecond laser pulse, so the thermal relaxation processes of the target [42, 54] can appear, and photothermal or photomechanical phenomena can be observed during the laser ablation of the metal plate. Hence, the ablation of the metal target will commence between 10 and 80 ps and plasma plum will form after 10 ns [42, 44, 46, 52], and the plasma appears after twice the pulse duration time [44, 46]. Therefore, when the metal plates are ablated with an ultra-short pulse laser (10^{-15} and 10^{-12} s), the delay between ejection of nanoparticles and interaction of laser beam with the metal target is not observable [42]. The concept of this delay is significant for the ablation mechanism [43, 46]. The plasma plume can absorb part of the incoming laser energy when the long laser pulse will be used for ablation of the metal target. The absorption of laser beam increases the temperature of the plasma and favors the atomization of the material contained in the plume [6, 44, 46]. Consequently, the phase materials released from the metal target are homogenized [6]. On the other hand, the laser energy absorbed by the target decreases due to the optical shielding of the plasma plume, while target ablation by interaction with the plasma plume is enhanced due to the increased plasma temperature [6, 44] and the absorption cross section of bulk metals is increased with a decreased laser wavelength [49]. Nevertheless, the ablation efficiency depends on absorption effects or the irradiation at short wavelengths. Metal nanoparticles usually have strong

plasmon resonance or inter band transitions in the UV-visible spectrum; hence, the laser beam can be interacted and absorbed by metal nanoparticles which were generated in liquid. This phenomenon occurred with two negative effects including the damping of ablation rate and altering the concentration and distribution of particle size [54]. Plasma plume has the tendency to absorb the laser beam at short wavelengths during the ablation process [44]. Therefore, the relation between the absorption coefficient and ablation efficiency appear in nonlinear, and these phenomena are minimum when the laser beam wavelength in the infrared range [54].

The nucleation of nanoparticles is formed during the plasma plume cooling. The nuclei growth and coalescence are the predominant mechanisms in the formation of metal nanoparticles using laser ablation technique [44, 55]. This procedure was confirmed with microscopy image of the polycrystalline structure of metal nanoparticles [56–59]. Consequently, during the formation of particles, ion metal and nanoparticles that formed in the liquid have interaction [44, 54, 55]. The nanoparticles can grow without any agent and ligand for some day after preparation in liquid because metal ions remain in an aqueous solution few days, and the formation of metal nanoparticles such as Pt and Ag continue with high affinity with the liquid such as water [55, 60]. As mention above, the size of metal nanoparticles depends on the density of metal atoms and temperature [44, 55], and sometimes, the atomic density and the temperature are not homogeneous in the plasma plume since two boundary regions exist with the surrounding liquid and the metal target [44, 46]. Many researchers reported that an energy threshold exists for the formation of nanoparticles using laser ablation technique [48, 50, 52, 54, 55]. The preparation of metal nanoparticle using laser ablation of metal target requires the presence of a plasma plume, and the minimum metal atom density should be provided to form the metal nanoparticles in the solvent [49, 50, 54, 55, 61]. The evidence of strong reactivity between metal and solvent in the plasma plume are consequences of the extreme pressure and temperature conditions [44]. Consequently, the plasma plume is quenched one order of magnitude faster in liquids than in gas or vacuum and the cooling process may not be considered an adiabatic process [44, 62]. This is useful for out-of-equilibrium reactions and the synthesis of metastable phases formed at high pressures and temperatures [44].

4. Laser ablation setups

Many researchers have used the laser ablation setup in different forms to syntheses the metal nanoparticles in a liquid. Basically, the laser ablation setup contains a lens, a high power pulsed laser, a liquid container, a stirrer, and a linear positioner. The metal targets such as gold, silver, or copper (99.99%) were submersed in liquid. A Nd:YAG pulsed laser beam of 532 nm or 1064 nm ablated the metal plate. **Figure 1** shows the laser ablation setup, which contains a Q-switched Nd:YAG laser, a solution container, a metal plate, a lens (f = 30 cm), a travel linear stage, and a stirrer. The duration of pulse and the laser ablation time can change from 10 to 60 Hz and 5–60 min, respectively. To prevent the absorption of energy of laser beam in the liquid solution, the path length which the laser beam passes through the liquid must be adjusted to shortest length. So, the distance between the target and entrance windows is a significant factor to achieve the best energy of laser beam on the surface of the target. In order to make sure the metal nanoparticles disperse evenly in the liquid solution, stirring of

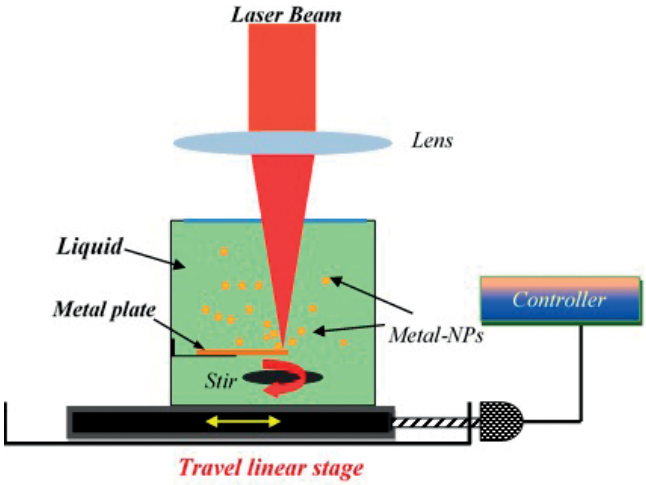

Figure 1. Laser ablation setup for the preparation of metal nanoparticles contains a travel linear stage, a high-power laser, a metal plate, and a liquid tank.

the solution is carried out during the ablation of the metal plate, and the solution container moves horizontally using travel linear stage for providing the fresh area to ablate the target.

5. The effect of thermal properties in laser ablation of metal plate

Normally, the metal nanoparticles are generated using high energy laser pulsed inside an aqueous solution with pico, nano, and femtosecond pulsed laser. Pulsed laser should be melted the target to generate the nanoparticles. If the femtosecond or nanosecond pulses are used to prepare metal nanoparticles, the main problem is the generation of heat in the sample, and the calculation of temperature is difficult. This problem can be significantly simplified based on diffusion length. Indeed, the heat diffusion length is smaller than laser spot size. Hence, the temperature can be controlled during the laser ablation of the metal plate. For example, in some typical experiments, the spot size is about 10 μm, and it is larger than diffusion length. Moreover, the laser beam has a flat-top profile, and the absorbed energy of laser beam causes the increasing of temperature in the target layer. The area of the layer that covers with the laser beam is equal to the spot size of the laser, and it surrounds by liquid that absorbs the heat and decreases the temperature of the layer. In the presence of liquid, the average temperature increases, and from thermal equilibrium, the relationship temperature and other thermodynamic parameter are obtained as follows [63, 64]:

$$T \cong \frac{Aj}{c\rho h} \tag{2}$$

where A ($A = 1 - R$, where R is the reflectivity coefficient at the laser wavelength) is the absorptivity of the metal plate at the particular wavelength, and c, ρ, and h are the heat capacity of the target material, the density of the metal target, and the thermal diffusion length in

the metal plate, respectively. The temperature has the relationship with the energy density of the laser beam, or it is fluence j. The thermal diffusion length h depends on the thermal diffusivity of the target materials [65]:

$$h \propto \sqrt{a\, t_p} \tag{3}$$

where a ($k/c\rho$, k is the thermal conductivity of the metal plate) and t_p are thermal diffusivity and the laser pulse duration, respectively, and the increasing of temperature (T) depends on absorption of laser radiation in particular wavelength as follows:

$$\alpha^{-1} \ll h, \tag{4}$$

Some part of laser power is converted to heat and it is the consequence of the evaporation of a solution near the laser beam, and this power is very weak.

6. The effect of wavelength in laser ablation of metal plate

When the laser ablation of the metals plate is considered, the wavelength of laser beam is a significant parameter. Because the optical constants of the material depend on wavelength; hence, the metal nanoparticles and metal targets can absorb the energy of laser beam at the particular wavelength. Metal clusters release in the nano-size from the metal plate and they can provide the condition for absorption of laser energy at each pulse, so the metal target can melt and the generation of nanoparticles becomes faster. Consequently, the higher repetition rate of laser pulses can provide the higher rate of generation of nanoparticles [66].

Jeon and Yeh were reported about the wavelength dependence of particle size and the formation efficiency in laser ablation [67]. They prepared the silver nanoparticle in inorganic (water) and organic solution (isopropanol) using green laser and infrared laser at nanosecond pulse. They achieved that the particle size using the green laser is larger than the particle size using the infrared laser. Hence, the formation efficiency of nanoparticles using infrared laser was lower than that using the green laser. Moreover, the laser fluence can change the size of the nanoparticle as a function of laser wavelength [65]. Hence, the fragmentation of nanoparticles can improve with enhancement of fluence. The dimension of nanoparticles prepared using infrared photon increases when the laser fluence increases. Consequently, when the wavelength of laser beam decreases, the ablation efficiency increases with the energy of laser beam.

7. The effect of light absorption with nanoparticles in laser ablation method

The absorption of laser beam with nanoparticles is the effective factor of the laser ablation process at high laser fluence to prepare the nanoparticles in an aqueous solution. When the prepared nanoparticles have not high mobility in liquid, they are aggregated near the target.

Hence, they can absorb the energy of laser beam. This effect increases with increasing laser fluence because of the increase in the number of produced nanoparticles. Therefore, the intensity of laser beam that can reach the metal target is decreased. In addition, the size of the nanoparticles that absorb the incident laser beam decreases because of the laser-induced fragmentation occurs [68, 69]. This phenomenon was reported by Prochazka et al. [9]. They achieved the size of nanoparticles decreased when the laser beam interacted with the colloids during ablation of the metal target [70]. Consequently, the colloidal absorption causes the decreasing of the formation efficiency and the size of nanoparticles. This phenomenon called secondary effect. It can produce the high concentration nanoparticles and can control the formation process, and the size of nanoparticles and especially suppression of the ablation efficiency are undesired. Another considerable parameter is a flow-cell system, which is necessary for suppressing the colloidal absorption. Two colloidal absorption processes can be considered for preparation of metal nanoparticles. One is "interpulse" absorption and other is "intrapulse" absorption. The interpulse absorption related to the generation of nanoparticles by the earlier pulses stays in the laser beam path and absorbs the latterly coming pulses. The intrapulse absorption related to particles produced by the earlier part of one pulse immediately absorbs the later part of the same pulse.

8. Laser ablation of silver nanoparticle in liquids

Many researchers reported the preparation of silver nanoparticles in organic and inorganic solutions. Silver nanoparticles have biological, thermal, optical, and electrical properties. Hence, the synthesis of silver nanoparticles was presented using chemical and physical methods. Laser ablation of silver plate is an alternative and green method to prepare the

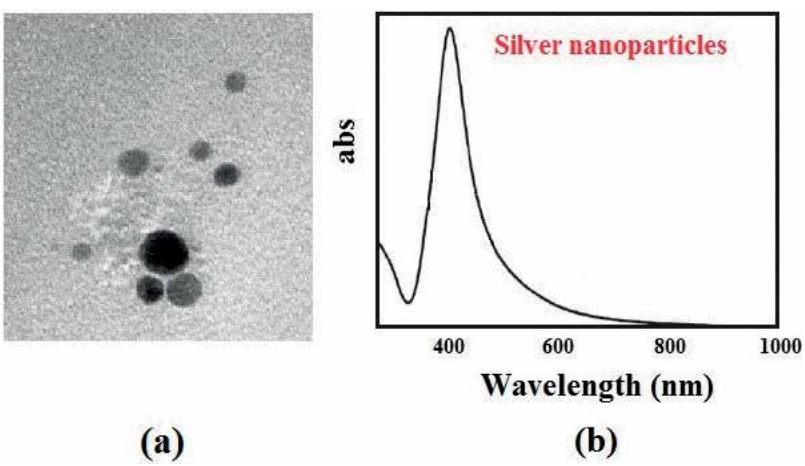

Figure 2. (a) TEM image of silver nanoparticle in oil and (b) UV-visible spectrum of silver nanoparticles produced using laser ablation.

silver nanoparticles, and nanoparticles grow in the unique form of organic and inorganic solutions without any agglomeration and collapsing. Silver nanoparticles were prepared in water, methanol, palm oil [22], coconut oil [71], pomegranate seed oil [72], polyvinyl alcohol (PVA) [28], and graphene oxide solution [73]. Silver nanoparticles were capped by chain fatty acid of oils, and the particle size was about 10 nm. When the ablation time increases, the size of particles decreases. Nanoparticles formed in the spherical shape that was obtained using transmission electron microscope image (**Figure 2a**). The efficiency of the colloidal absorption by silver nanoparticles for 355, 532, and 1064 nm laser beam depends on localized surface plasmon resonance or the plasmon band around 400 nm (**Figure 2b**). Hence, the maximum and minimum efficiency occurred in 355 and 1064 nm. Thus, the influence of the colloidal absorption was more prominent for shorter wavelength laser beam, leading to the conclusion that the formation efficiency and the size of nanoparticles decrease with decreasing laser wavelength.

9. Laser ablation of gold nanoparticles in liquid

Gold nanoparticles (Au-NPs) have more applications for electronics [74], photodynamic therapy [75], therapeutic agent delivery [76], tumor therapy [77], sensors [78], drugs carriers [79], and medical diagnoses [80]. High activity and high sensitivity of Au-NPs have been fabricated using laser ablation in water [81]. The final product was used to reclaim the area of glassy graphite electrode for detection of Hg, Pb, Cu, and Co in the low concentration [81]. Gold nanoparticles can absorb and interact with the electrical field of laser beam [79], and Au-NPs generate localized surface plasmon absorption in the range of 400–900 nm [82]. The coherent excitation of free electrons causes the surface plasmon band in a colloidal nanoparticle [83]. The response of the Au-NPs to an interaction of laser beam depends on particle size, the surrounding material, and nanoparticle concentration [84]. Hence, the investigation and consideration of green synthesis of gold nanoparticles are intense interest subject in nanomedicine and nanotechnology area. Laser ablation technique is an alternative method for preparation of gold nanoparticles in an aqueous solution. Recently, gold nanoparticles were prepared in graphene oxide and vegetable oils such as pomegranate seed oil [25]. When gold nanoparticles were fabricated using laser ablation of the gold target, the nanoparticles were formed in the spherical shape (**Figure 3a**) that was investigated using transmission electron microscopy. The particle size was in the range of 20–5 nm, and the UV-visible absorption peak appeared about 530 nm (**Figure 3b**). In accordance with Mie theory, when the particle size decreases, the blue shift ($\Delta\lambda$) occurs in the localized surface plasmon absorption peak as follows:

$$\Delta\lambda = \lambda_0 \times 0.18 \times exp\left(\frac{-s}{0.23 \times D}\right) \tag{5}$$

where λ_0, s, and D are central wavelength, interparticle gap, and particle size in the central wavelength [85, 86].

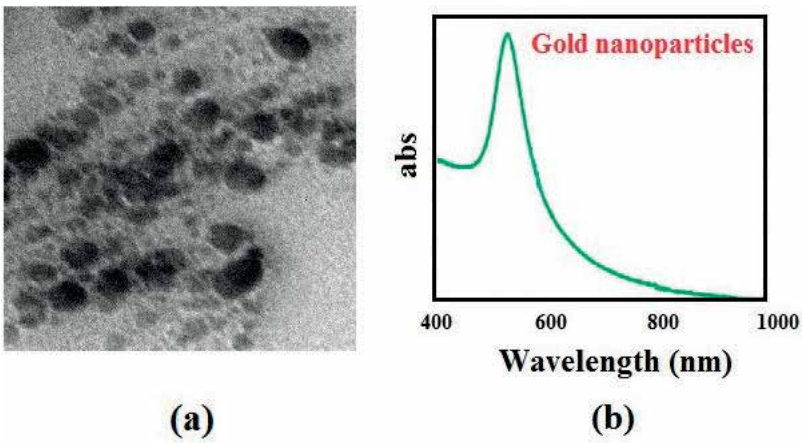

Figure 3. (a) TEM image of gold nanoparticles in oil and (b) UV-visible spectrum of gold nanoparticles produced using laser ablation.

10. Laser ablation of copper nanoparticles

Copper nanoparticles (Cu-NPs) have more application conductive coatings, lubricants, sintering additives [87], and biosensors [88]. Copper nanoparticles are anti-inflammatory [89], reduce gastrointestinal mucosa [90], antioxidative [91], anti-ulcer [92], and are useful in preventing skin photosensitivity [93]. The copper nanoparticles strongly absorb the light beams about 600 nm, arising from the localized surface plasmon resonance (LSPR).

Recently, the application of vegetable oils such as palm oil [22], coconut oil [71], walnut oil [23], and castor oil [31] for dispersing the nanoparticles was considered for the preparation of nanometals [94]. These natural compounds contain triglycerides and non-polar long carbon chains that prevent nanoparticles agglomeration through steric repulsion [71].

Many methods based on the reaction of metal ions were presented to prepare copper nanoparticles. For example, solution phase [95], photochemical [96], sonochemical [97], and electrochemical synthesis methods [14] are the famous methods that are utilized for preparation of Cu-NPs in an aqueous solution. Laser ablation [98] is a green technique for the synthesis of copper nanoparticles. In the literature, the preparation of copper nanoparticles in distilled water, acetone, and ethanol [99] was reported using laser ablation. Malyavantham et al. [100] utilized the laser ablation technique to fabricate the Au-Cu NPs alloy. Copper nanoparticles were formed in the spherical shape (**Figure 4a**) in an aqueous solution. The UV-visible peak arose the localized surface plasmon resonance about 630 nm (**Figure 4b**). The influence of the colloidal absorption on the formation efficiency of copper nanoparticles was also the significant parameter to prepare copper nanoparticles. The formation efficiencies of Cu-NPs using 532 and 1064 nm laser beam were much closer than those of silver nanoparticles because the absorption at 532 nm in copper colloids was lower than that in silver colloids.

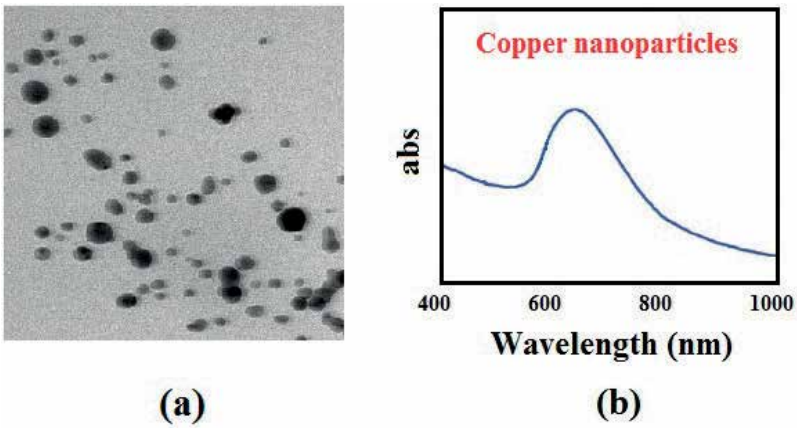

Figure 4. (a) TEM image of copper nanoparticle in oil and (b) UV-visible spectrum of copper nanoparticles produced using laser ablation.

11. Compression of silver, gold, and copper nanoparticles

The silver, gold, and copper nanoparticles formed in the liquid solution in the spherical shape using pulsed laser ablation of plate, and they have the localized surface plasmon resonance peaks in the visible range; but the copper nanoparticle has tendency to convert copper oxide sooner than gold and silver nanoparticles. According to the literature, the gold nanoparticle was formed in the liquids faster than silver and copper nanoparticles [101]. Gold, silver, and copper nanoparticles have the different biological and medical applications. Gold nanoparticles were used as an antibiotic, anti-fungal, and anti-microbial agent. Gold nanoparticles were used for drug delivery and anti-cancer. Silver and copper nanoparticles are a strong anti-bacterial and anti-inflammatory. Gold and silver nanoparticles were used as optical probes, sensor, and catalyst.

12. Conclusion

Laser ablation is a green and simple method for fabrication of the metal nanoparticles without surfactant or chemical addition, and the properties of nanoparticles are unique. The wavelength of laser and laser intensity are the significant parameters for production of metal nanoparticles; hence, the formation efficiency of nanoparticles using infrared laser was lower than that using the green laser, and the thermal effect strongly appeared in the case of laser with nanosecond pulse. The particle size was in the range of 5–20 nm, and the nanoparticles were formed in the spherical shape in an aqueous solution using laser ablation technique.

Author details

Amir Reza Sadrolhosseini[1,2]*, Mohd Adzir Mahdi[3,4], Farideh Alizadeh[5] and Suraya Abdul Rashid[2]

*Address all correspondence to: amir17984818@gmail.com

1 Functional Device Laboratory, Institute of Advanced Technology, Universiti Putra Malaysia, Serdang, Selangor, Malaysia

2 Materials Processing and Technology Laboratory (MPTL), Nanomaterials and Nanotechnology Group, Institute of Advanced Technology, Universiti Putra Malaysia, Serdang, Selangor, Malaysia

3 Wireless and PhotonicNetworks Research Centre of Excellence (WiPNET), Faculty of Engineering, Universiti Putra Malaysia, Malaysia

4 Department of Computer and Communication Systems Engineering, Faculty of Engineering, Universiti Putra Malaysia (UPM), Serdang, Malaysia

5 Drama Department, Cultural Centre, University of Malaya, Jalan Universiti, Kuala Lumpur, Malaysia

References

[1] Hahn A, Barcikowski S, Chichkov B. Influences on nanoparticle production during pulsed laser ablation. JLMN-Journal of Laser Micro/Nanoengineering. 2008;**3**:73-77

[2] Kabashin AV, Meunier M, Kingston C, Luong JHT. Fabrication and characterization of gold nanoparticles by femtosecond laser ablation in an aqueous solution of cyclodextrins. The Journal of Physical Chemistry B. 2003;**107**:4527-4531

[3] Tsuji T, Hamagami T, Kawamura T, Yamaki J, Tsuji M. Laser ablation of cobalt and cobalt oxides in liquids: Influence of solvent on composition of prepared nanoparticles. Applied Surface Science. 2005;**243**:214-219

[4] Etchegoin PG, Ru ECL. A perspective on single molecule SERS: Current status and future challenges. Physical Chemistry Chemical Physics. 2008;**10**:6079-6089

[5] Daniel MC, Astruc D. Gold nanoparticles: Assembly, supramolecular chemistry, quantum-size-related properties, and applications toward biology, catalysis, and nanotechnology. Chemical Reviews. 2004;**104**:293-346

[6] Amendola V, Meneghetti M. Laser ablation synthesis in solution and size manipulation of noble metal nanoparticles. Physical Chemistry Chemical Physics. 2009;**11**:3805-3821

[7] Xia Y, Halas NJ. Shape-controlled synthesis and surface plasmonic properties of metallic nanostructures. MRS Bulletin. 2005;**30**:338-348

[8] Murphy CJ, Gole AM, Stone JW, Sisco PN, Alkilany AM, Goldsmith EC, et al. Gold nanoparticles in biology: Beyond toxicity to cellular imaging. Accounts of Chemical Research. 2008;**41**:1721-1730

[9] Caragheorgheopol A, Chechik V. Mechanistic aspects of ligand exchange in Au nanoparticles. Physical Chemistry Chemical Physics. 2008;**10**:5029-5041

[10] Corma A, Garcia H. Supported gold nanoparticles as catalysts for organic reactions. Chemical Society Reviews. 2008;**37**:2096-2126

[11] Jiang L-P, Wang A-N, Zhao Y, Zhang J-R, Zhu J-J. A novel route for the preparation of monodisperse silver nanoparticles via a pulsed sonoelectrochemical technique. Inorganic Chemistry Communications. 2004;**7**:506-509

[12] Haas I, Shanmugam S, Gedanken A. Pulsed sonoelectrochemical synthesis of size-controlled copper nanoparticles stabilized by poly(N-vinylpyrrolidone). The Journal of Physical Chemistry B. 2006;**110**:16947-16952

[13] Alonso F, Riente P, Sirvent JA, Yus M. Nickel nanoparticles in hydrogen-transfer reductions: Characterisation and nature of the catalyst. Applied Catalysis A. 2010;**378**:42-51

[14] Remita S, Mostafavi M, Delcourt MO. Bimetallic Ag-Pt and Au-Pt aggregates synthesized by radiolysis. Radiation Physics and Chemistry. 1996;**47**:275-279

[15] Brust M, Walker M, Bethell D, Schiffrin DJ, Whyman R. Synthesis of thiol-derivatised gold nanoparticles in a two-phase liquid-liquid system. Journal of the Chemical Society, Chemical Communications. 1994;**7**:801-802

[16] Osseo-Asare K, Arriagada FJ. Synthesis of nanosize particles in reverse microemulsions. Ceramic Transactions. 1990;**12**:3-16

[17] Kurihara LK, Chow GM, Schoen PE. Nanocrystalline metallic powders and films produced by the polyol method. Nanostructured Materials. 1995;**5**:607-613

[18] Eluri R, Paul B. Microwave assisted greener synthesis of nickel nanoparticles using sodium hypophosphite. Materials Letters. 2012;**76**:36-39

[19] Al-Azawi1 MA, Bidin N. Gold nanoparticles synthesized by laser ablation in deionized water. Chinese Journal of Physics. 2105;**53**:080803-1-080803-9

[20] Barberio M, Barone P, Xu F, Bonanno A. Silver nanoparticles synthesized by laser ablation in acetone: Influence of ablation time and their reactivity with oxygen in the air. Journal of Chemistry and Chemical Engineering. 2013;**7**:1142-1148

[21] Sadrolhosseini AR, Abdul Rashid S, Zakaria A, Shameli K. Green fabrication of copper nanoparticle dispersed in walnut oil using laser ablation. Journal of Nanomaterials. 2016;**2016**:8069685

[22] Sadrolhosseini AR, Abdul Rashid S, Noor ASM, Kharazmi A, Mehdipour LA. Fabrication of silver nanoparticles in pomegranate seed oil with thermal properties by laser ablation technique. Digest Journal of Nanomaterials and Biostructures. 2015;**10**:1009-1018

[23] Sadrolhosseini AR, Noor ASM, Husin MS, Sairi NA. Green synthesis of gold nanoparticles in pomegranate seed oil stabilized using laser ablation. Journal of Inorganic and Organometallic Polymers. 2014;**24**:1009-1013

[24] Sadrolhosseini AR, Noor ASM, Shameli K, Mamdoohi G, Moksin MM, Mahdi MA. Laser ablation synthesis and optical properties of copper nanoparticles. Journal of Materials Research. 2013;**28**:2629-2636

[25] Zamiri R, Azmi BZ, Goodarz Naseri M, Abbastabar Ahangar H, Darroudi M, Kalaei Nazarpour F. Laser based fabrication of chitosan mediated silver nanoparticles. Applied Physics A: Materials Science & Processing. 2011;**105**:255-261

[26] Halimah MK, Goodarz Naseri M, Sadrolhosseini AR, Dehzangi A, Kamalianfa A, Saion E, et al. Silver nanoparticle fabrication by laser ablation in polyvinyl alcohol solutions. Chinese Physics Letters. 2014;**31**:077803

[27] Momma C, Chichkov BN, Nolte S, von Alvensleben F, Tu A, Welling H, Wellegehausen B. Short-pulse laser ablation of solid targets. Optics Communication. 1996;**129**:134-142

[28] Zhigilei LV, Kodali PBS, Garrison BJ. A microscopic view of laser ablation. The Journal of Physical Chemistry. B. 1998;**102**:2845-2853

[29] Rosi NL, Mirkin CA. Nanostructures in biodiagnostics. Chemical Reviews. 2005;**105**: 1547-1562

[30] Ferrari M. Cancer nanotechnology: Opportunities and challenges. Nature Reviews. Cancer. 2005;**5**:161-171

[31] Raveendran P, Fu J, Wallen SL. Completely 'green' synthesis and stabilization of metal nanoparticles. Journal of the American Chemical Society. 2003;**125**:13940-13941

[32] Giuffrida S, Condorelli GG, Costanzo LL, Fragala IL, Ventimiglia G, Vecchio G. Photochemical mechanism of the formation of nanometer-sized copper by UV irradiation of ethanol Bis(2,4-pentandionato) copper(II) solutions. Chemistry of Materials. 2004;**16**: 1260-1266

[33] Madhwani KP. Safe development of nanotechnology: A global challenge. Indian Journal of Occupational and Environmental Medicine. 2013;**17**:87-89

[34] Bernardi A, Becherinia F, Bassatob G, Belliob M. Condensation on ancient stained glass windows and efficiency of protective glazing systems: Two French case studies. Sainte-Chapelle (Paris) and Saint-Urbain Basilica (Troyes). 2006;**7**:71-78

[35] Wong JY, McDonald J, Taylor-Pinney M, Spivak DI, Kaplan DL, Buehler MJ. Materials by design: Merging proteins and music. Nano Today. 2012;**7**:488-495

[36] Barnes JA, Gagliardi G, Loock H-P. The photonic guitar pick-up: Fiber strain sensors find applications in music recording. IEEE Photonics Society Journal. 2013;**27**:19-23

[37] Baglioni P, Giorgi R, Chelazzi D. Nano-materials for the conservation and preservation of movable and immovable artworks. International Journal of Heritage in the Digital Era. 2012;**1**:313-318

[38] Vojtěchovský J. Surface consolidation of wall paintings using lime nano-suspensions. Acta Polytechnica. 2017;**57**:139-148

[39] Giorgi R, Baglioni M, Berti BP. New methodologies for the conservation of cultural heritage: Micellar solutions, microemulsions, and hydroxide nanoparticles. Accounts of Chemical Research. 2010;**43**:695-704

[40] Giorgi R, Bozzi C, Dei L, Gabbiani CW, Ninham B, Baglioni P. Nanoparticles of $Mg(OH)_2$: Synthesis and application to paper conservation. Langmuir. 2005;**21**:8495-8501

[41] Bartoletti A, Odlyha M, Hudziak S, Axelsson KM, de Groot J, Bozec L. Source: Insight-non-destructive testing and condition monitoring. The British Institute of Non-Destructive Testing. 2017;**59**:265-272

[42] Yang GW. Laser ablation in liquids: Applications in the synthesis of nanocrystals. Progress in Materials Science. 2007;**52**:648-698

[43] Fabbro R, Fournier J, Ballard P, Devaux D, Virmont J. Physical study of laser-produced plasma in confined geometry. Journal of Applied Physics. 1990;**68**:775-784

[44] Sakka T, Iwanaga S, Ogata YH, Matsunawa A, Takemoto T. Laser ablation at solid–liquid interfaces: An approach from optical emission spectra. The Journal of Chemical Physics. 2000;**112**:8645-8653

[45] Tsuji T, Okazaki Y, Tsuboi Y, Tsuji M. Nanosecond time-resolved observations of laser ablation of silver in water. Japanese Journal of Applied Physics. 2007;**46**:1533-1535

[46] Sylvestre JP, Kabashin AV, Sacher E, Meunier M. Femtosecond laser ablation of gold in water: Influence of the laser-produced plasma on the nanoparticle size distribution. Applied Physics A: Materials Science & Processing. 2005;**80**:753-758

[47] Nichols WT, Sasaki T, Koshizaki N. Laser ablation of a platinum target in water. I. Ablation Mechanisms. Journal of Applied Physics. 2006;**100**:114911-114917

[48] Nichols WT, Sasaki T, Koshizaki N. Laser ablation of a platinum target in water. II. Ablation rate and nanoparticle size distributions. Journal of Applied Physics. 2006;**100**:114912

[49] Knochenmuss R. Ion formation mechanisms in UV-MALDI. The Analyst. 2006l;**131**: 966-986

[50] Kabashin AV, Meunier M. Synthesis of colloidal nanoparticles during femtosecond laser ablation of gold in water. Journal of Applied Physics. 2003;**94**:7941-79413

[51] Link S, El-Sayed MA. Shape and size dependence of radiative, non-radiative and photothermal properties of gold nanocrystals. International Reviews in Physical Chemistry. 2000;**19**:409-453

[52] Mafune F, Kohno J, Takeda Y, Kondow T, Sawabe H. Formation of gold nanoparticles by laser ablation in aqueous solution of surfactant. The Journal of Physical Chemistry. B. 2001;**105**:5114-5120

[53] Mafune F, Kohno J, Takeda Y, Kondow T, Sawabe H. Formation and size control of silver nanoparticles by laser ablation in aqueous solution. The Journal of Physical Chemistry. B. 2000;**104**:9111-9117

[54] Amendola V, Polizzi S, Meneghetti M. Free silver nanoparticles synthesized by laser ablation in organic solvents and their easy functionalization. Langmuir. 2007;**23**:6766-6770

[55] Compagnini G, Scalisi AA, Puglisi O. Production of gold nanoparticles by laser ablation in liquid alkanes. Journal of Applied Physics. 2003;**94**:7874-7877

[56] Amendola V, Meneghetti M. Controlled size manipulation of free gold nanoparticles by laser irradiation and their facile bioconjugation. Journal of Materials Chemistry. 2007;**17**: 4705-4710

[57] Compagnini G, Scalisi AA, Puglisi O. Ablation of noble metals in liquids: A method to obtain nanoparticles in a thin polymeric film. Physical Chemistry Chemical Physics. 2002; **4**:2787-2791

[58] Mafuné F, Kondow T. Selective laser fabrication of small nanoparticles and nanonetworks in solution by irradiation of UV pulsed laser onto platinum nanoparticles. Chemical Physics Letters. 2004;**383**:343-347

[59] Nichols WT, Sasaki T, Koshizaki N. Laser ablation of a platinum target in water. III. Laser-induced reaction. Journal of Applied Physics. 2006;**100**:114913

[60] Tsuji T, Kakita T, Tsuji M. Preparation of nano-size particles of silver with femtosecond laser ablation in water Appl. Surface Science. 2003;**206**:314-320

[61] Amendola V, Polizzi S, Meneghetti M. Laser ablation synthesis of gold nanoparticles in organic solvents. The Journal of Physical Chemistry. B. 2006;**110**:7232-7237

[62] Saitow K, Yamamura T, Minami T. Gold nanospheres and nanonecklaces generated by laser ablation in supercritical fluid. Journal of Physical Chemistry C. 2008;**112**:18340-18349

[63] Yang G. Laser Ablation in Liquids: Principles and Applications in the Preparation of Nanomaterials. FL, USA: CRC Press; 2012

[64] Semerok A, Chaleard C, Detalle V, Lacour JL, Mauchien P, Meynadier P, et al. Experimental investigations of laser ablation efficiency of pure metals with femto, pico and nanosecond pulses. Applied Surface Science. 1999;**139**:311-314

[65] Jeon JS, Yeh CS. Studies of silver nanoparticles by laser ablation method. Journal of the Chinese Chemical Society. 1998;**45**:721-726

[66] Kamat PV, Flumiani M, Hartland GV. Picosecond dynamics of silver nanoclusters. Photoejection of electrons and fragmentation. Journal of Physical Chemistry B. 1998;**102**:3123-3128

[67] Link S, Burda C, Mohamed MB, Nikoobakht B, El-Sayed MA. Laser photothermal melting and fragmentation of gold nanorods: Energy and laser pulse-width dependence. The Journal of Physical Chemistry. A. 1999;**103**:1165-1170

[68] Prochazka M, Mojzes P, Stepanek J, Vlckova B, Turpin PY. Probing applications of laser-ablated Ag colloids in SERS spectroscopy: Improvement of ablation procedure and SERS spectral testing. Analytical Chemistry. 1997;**69**:5103-5108

[69] Zamiri R, Zakaria A, Abbastabar Ahangar A, Sadrolhosseini AR, Mahdi MA. Fabrication of silver nanoparticles dispersed in palm oil using laser ablation. International Journal of Molecular Sciences. 2010l;**11**:4764-4770

[70] Zamiri R, Azmi BZ, Sadrolhosseini AR, Abbastabar H, Zaidan AW, Mahdi MA. Preparation of silver nanoparticles in virgin coconut oil using laser ablation. International Journal of Nanomedicine. 2011;**6**:71-75

[71] Sadrolhesseini AR, Kharazmi A, Zakaria A, Huang NM, Noor ASM, Mahdi MA. Laser ablation synthesis of silver nanoparticle in graphene oxide and thermal effusivity of nanocomposite. In: Proceeding of ICP 2013; 28th–30th Oct, 2013; Kuala Lumpur

[72] Tomar A, Garg G. Short review on application of gold nanoparticles. Global Journal of Pharmacology. 2013;**7**:34-38

[73] Khaing Oo MK, Yang Y, Hu Y, Gomez M, Du H, Wang H. Gold nanoparticle-enhanced and size-dependent generation of reactive oxygen species from Protoporphyrin. ACs Nano. IX. 2012;**6**:1939-1947

[74] Vigderman L, Zubarev ER. Therapeutic platforms based on gold nanoparticles and their covalent conjugates with drug molecules. Advanced Drug Delivery Reviews. 2013;**65**:663-676

[75] Kennedy LC, Bickford LR, Lewinski NA, Coughlin AJ, Hu Y, Day ES, et al. A new era for cancer treatment: Gold-nanoparticle-mediated thermal therapies. Small. 2011;**7**:169-183

[76] Saha K, Agasti SS, Kim C, Li X, Rotello VM. Gold nanoparticles in chemical and biological sensing. Chemical Reviews. 2012;**112**:2739-2779

[77] Duncan B, Kim C, Rotello VM. Gold nanoparticle platforms as drug and biomacromolecule delivery systems. Journal of Controlled Release. 2010;**148**:122-127

[78] Cai W, Gao T, Hong H, Sun J. Applications of gold nanoparticles in cancer nanotechnology. Nanotechnology, Science and Applications. 2008;**1**:17-32

[79] Xu X, Duan G, Li Y, Liu G, Wang J, Zhang H, Dai Z, Cai Z. Fabrication of gold nanoparticles by laser ablation in liquid and their application for simultaneous electrochemical detection of Cd^{2+}, Pb^{2+}, Cu^{2+}, Hg^{2+}. ACS Applied Materials & Interfaces. 2014;**6**:65-71

[80] Halas NJ, Lal S, Chang WS, Link S, Nordlander P. Plasmons in strongly coupled metallic nanostructures. Chemical Reviews. 2011;**111**:3913-3961

[81] Jain PK, Lee KS, El-Sayed IH, El-Sayed MA. Calculated absorption and scattering properties of gold nanoparticles of different size, shape, and composition: Applications in biological imaging and biomedicine. The Journal of Physical Chemistry. B. 2006;**110**: 7238-7248

[82] Templeton AC, Pietron JJ, Murray RW, Mulvaney PJ. Solvent refractive index and core charge influences on the surface plasmon absorbance of alkanethiolate monolayer-protected gold clusters. Physical Chemistry B. 2000;**104**:564-570

[83] Jain P, Huang W, El-Sayed M. On the universal scaling behavior of the distance decay of plasmon coupling in metal nanoparticle pairs: A plasmon ruler equation. Nano Letters. 2007;**7**:2080-2088

[84] Walter JG, Petersen S, Stahl F, Scheper T, Barcikowski T. Laser ablation-based one-step generation and bio-functionalization of gold nanoparticles conjugated with aptamers. Journal of Nanobiotechnology. 2010;**8**:21-32

[85] Giuffrida S, Costanzo LL, Ventimiglia G, Bongiorno G. Photochemical synthesis of copper nanoparticles incorporated in poly(vinyl pyrrolidone). Journal of Nanoparticle Research. 2008;**10**:1183-1192

[86] Kim D, Yoo SM, Park TJ, Yoshikaw H, Tamiy E, Park JY, et al. Plasmonic properties of the multispot copper-capped nanoparticle array chip and its application to optical biosensors for pathogen detection of multiplex DNAs. Analytical Chemistry. 2011;**83**:6215-6222

[87] Jackson GE, Mkhonta-Gama L, Voye A, Kelly M. Design of copper-based anti inflammatory drugs. Journal of Inorganic Biochemistry. 2000;**79**:147-152

[88] Szymański P, Frączek T, Markowicz M, Mikiciuk-Olasik E. Development of copper based drugs, radiopharmaceuticals and medical materials. Biometals. 2012;**25**:1089-1112

[89] Deng D, Cheng Y, Jin Y, Qia T, Xiao F. Antioxidative effect of lactic acid-stabilized copper nanoparticles prepared in aqueous solution. Journal of Materials Chemistry. 2012;**22**:23989-23995

[90] Tuorkey MJ, Abdul-Aziz KK. A pioneer study on the anti-ulcer activities of copper nicotinate complex [$CuCl(HNA)_2$] in experimental gastric ulcer induced by aspirin-pylorus [corrected] ligation model (Shay model). Biomedicine & Pharmacotherapy. 2009;**63**:194-201

[91] Bilgin MD, Elçin AE, Elçin YM. Topical use of liposomal copper palmitate formulation blocks porphyrin-induced photosensitivity in rats. Journal of Photochemistry and Photobiology. B. 2005;**80**:107

[92] da Silva EC, da Silva M, Meneghetti S, Machado G, Alencar M, Hickmann J, et al. Synthesis of colloids based on gold nanoparticles dispersed in castor oil. Journal of Nanoparticle Research. 2008;**10**:201-208

[93] Wu N, Fu L, Aslam M, Wong K, Dravid V. Interaction of fatty acid monolayers with cobalt nanoparticles. Nano Letters. 2004;**4**:383-385

[94] Giuffrida S, Condorelli GG, Costanzo LL, Fragalà IL, Ventimiglia G, Vecchio G. Photochemical mechanism of the formation of nanometer-sized copper by UV irradiation of ethanol bis(2,4-pentandionato) copper(II) solutions. Chemistry of Materials. 2004;**16**: 1260-1266

[95] Jiang LP, Wang AN, Zhao Y, Zhang JR, Zhu JJ. A novel route for the preparation of monodisperse silver nanoparticles via a pulsed sono-electrochemical technique. Inorganic Chemistry Communications. 2004;**7**:506-509

[96] Takeshi T, Iryo K, Nishimura Y, Tsuji M. Preparation of metal colloids by a laser ablation technique in solution: Influence of laser wavelength on the ablation efficiency (II). Journal of Photochemistry and Photobiology A: Chemistry. 2001;**145**:201-207

[97] Aye LH, Choopun S, Chairuangsri T. Preparation of nanoparticles by laser ablation on copper target in distilled water. Advanced Materials Research. 2010;**93-94**:83-86

[98] Muniz-Miranda M, Gellini C, Giorgetti E. Surface-enhanced Raman scattering from copper nanoparticles obtained by laser ablation. Journal of Physical Chemistry C. 2011;**115**:5021-5027

[99] Kazakevich PV, Voronov VV, Simakin AV, Shafeev GA. Production of copper and brass nanoparticles upon laser ablation in liquids. Quantum Electronics. 2004;**34**:951-956

[100] Malyavantham G, O'Brien DT, Becker MF, Keto JW, Kovar D. Au–Cu nanoparticles produced by laser ablation of mixtures of Au and Cu. Microparticles. Journal of Nanoparticle Research. 2004;**6**:661-664

[101] Solati E, Dorranian D. Comparison between silver and gold nanoparticles prepared by pulsed laser ablation in distilled water. Journal of Cluster Science. 2015;**26**:727-742

Chapter 5

Quantitative Planar Laser-Induced Fluorescence Technology

Zhen Yang, Xin Yu, Jiangbo Peng and Jianlong Zhang

Additional information is available at the end of the chapter

http://dx.doi.org/10.5772/intechopen.79702

Abstract

Planar laser-induced fluorescence (PLIF) is a highly sensitive and space-time-resolved laser diagnostic technique. It is widely used in the diagnosis of combustion and flow fields to obtain the thermodynamic information of active components and interested molecules in flames. Nowadays, the PLIF technology is developing in two directions: high speed and quantification. In view of the high spatial and temporal resolution characteristics of PLIF technology that other laser diagnostics do not possess, this chapter will focus on the basic principle of laser-induced fluorescence and the current research status of quantitative PLIF technology. In addition, the advantages and disadvantages of various quantitative technologies of component concentration in flames based on laser-induced fluorescence technology are analyzed. At last, the latest works on the quantification of species concentration using planar laser-induced fluorescence in combustion are introduced.

Keywords: bidirectional planar laser-induced fluorescence, combustion diagnostics, species concentration visualization, effective absorption cross section, laminar flames

1. Introduction

The planar laser-induced fluorescence [1] is a high-sensitivity and high-resolution laser spectral diagnostic technique developed in the 1980s. The emergence of PLIF technology has made great success in the visualization of the combustion field in flames, the dynamic evolution of the combustion process [2, 3], the temperature imaging [4, 5], and the quantitative measurements of the free radical concentrations under low pressure [6, 7]. PLIF technology is a noncontact measurement technology. Compared with the traditional contact measurement technology, PLIF technology not only has the unique advantages of noncontact and noninterference

to the combustion and flow fields but also can dynamically display and image two- or three-dimensional space structure of free radicals interested in combustion fields. These merits are unattainable and difficult to achieve by the traditional contact and other laser spectral diagnostic techniques, such as coherent anti-Stokes Raman scattering (CARS), degenerate four-wave mixing technology (DFWM), cavity ring down spectroscopy technology (CRDS), tunable diode laser absorption spectroscopy (TDLAS), and direct absorption spectroscopy.

Admittedly, PLIF technology also has its own shortcomings. The biggest obstacle is that the PLIF technology is rather difficult to achieve quantitative measurement. The greatest difficulty in quantification of the PLIF lies in the fact that the electronic collisional quenching rate of the molecules to be measured is not exactly the same at the different positions of flame under the normal and high pressures. Worse still, there is a big difference for the distribution of electronic quenching rates in different types of flames. In addition, the calibration factor is also a parameter, which is easy to change with the observation conditions. In a general way, the collisional quenching rates of the molecules to be measured in flame have little effect on the fluorescence signal under the low pressure, so it can be often neglected. However, the collisional quenching rates of molecules turn out to be very sensitive to the combustion environment in flames under normal and high pressures. Therefore, the profiles of the collisional quenching rates become difficult to be measured in real time due to the diversification of the flame structure. In this case, an additional consideration is needed to accurately deduce the concentration distribution information of the molecules to be measured using the fluorescence signals.

In order to eliminate the detrimental impact of quenching effect on the quantitative measurement of species concentration, Versluis et al. [8] proposed to combine the traditional laser-induced fluorescence (LIF) with absorption spectroscopy to excite the molecules using the two opposite direction laser beams, counteracting many influencing factors, such as collisional quenching effect, pressure, and the calibration constant of the Detector and optical system, so as to deduce species concentration profiles. However, the bidirectional LIF technology is highly depending on the spatial coincidence of the beam (especially for the sheet laser beam) and the signal-to-noise ratio (SNR) of the fluorescence signal, which leads to the lack of systematic research on this technology.

2. A brief analysis of planar laser-induced fluorescence

Laser-induced fluorescence is an essentially physical process of laser resonance excitation and fluorescence generation. When the molecule is excited by laser with a specific wavelength, it will transition from a low energy state (usually ground state) to a higher energy state (the excited state). Then the molecules in the excited state will spontaneously transition from the excited energy state to the low energy state after undergoing a series of non-radiative transition energy transfer. The energy of electromagnetic radiation between the excited state and the low energy state is released in the form of fluorescence radiation.

Hydroxyl (OH radical), a very important intermediate in flames, is considered to exist in the combustion process of most hydrocarbon fuels. Quantitative measurement of OH concentration

http://dx.doi.org/10.5772/intechopen.79702

is of great significance for deep understanding, modification, and validation of reaction mechanism and chemical kinetic models. This chapter takes OH as an example to explain. Similar conclusions exist for other combustion intermediates or radicals.

The energy-level structure consists of the electronic, vibrational, and rotational energy levels. When numerous OH radicals in the flame absorb a certain wavelength laser from the ground state to the excited state, one part of molecules will shift to other vibrational or rotational energy levels due to the effect of vibrational energy transfer (VET) and rotational energy transfer (RET), one part of which will be transferred to the pre-dissociated state, and some of which will be quenched due to the collision of atoms and molecules in the surrounding environment. After above three physical processes, in fact, the OH radicals no longer involve the process of fluorescence radiation. Therefore, only a fairly small number of OH radicals can emit fluorescence from the excited state to the ground state. The physical process is shown in **Figure 1**.

The main purpose of the LIF technology is to determine the total number density of OH radicals by using the observable intensity of the OH fluorescence signal and then to obtain the local physical properties of the measured molecules. However, there are many physical processes difficult to observe directly in the LIF process, such as VET, RET, collisional quenching, and predissociation, which will greatly affect the intensity of the OH fluorescence signal. Therefore, if the concentration of fluorescence signal is directly obtained by observation, one will cause great deviation. Generally, the time scales of VET, RET, and collisional quenching effects are much less than the lifetime of OH fluorescence. Therefore, it is rather difficult to directly measure these physical processes on the OH fluorescence signal.

Under the linear excitation, the LIF signal intensity of the excited molecule in position x at atmospheric pressure can be expressed as follows [9]:

$$I_{\mathrm{LIF}}(x,\omega,T,N_c) = \hbar\omega C_{exp} B_{mn} N_m^0 f_B(x,T) \frac{A_{nm}}{A_{nm}+Q(x,T,N_c)} \int_{\omega} \frac{I(x,\omega)}{c} g(x,\omega,T,N_c) d\omega \qquad (1)$$

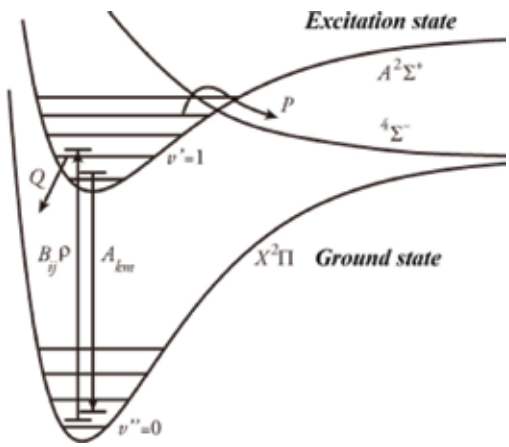

Figure 1. The LIF process of hydroxyl radical [9].

where $\hbar$ is the Planck reduced constant; ω is the angular frequency related to the energy interval between the selected excited levels; $C_{\exp}$ is an experimental constant influenced by the quantum efficiency of detector, the filter function, and the solid angle of optical system; B_{mn} is the Einstein stimulated absorption coefficient from low energy state (m state) to high energy state (n state); N_m^0 is the molecular number density in m state; $f_B(x,T)$ is the Boltzmann Fraction in position x; T is the temperature; A_{nm} is the spontaneous emission rate of excited molecules transitioning from n state to m state; $Q(x,T,N_c)$ is the collisional quenching rate related to the temperature and the total number N_c around the collisional molecules; $I(x,\omega)$ is the intensity of excited laser in position x; and $g(x, \omega, T, N_c)$ is the molecular integrated absorption line-shape in position x. In Eq. (1), the factor of $A_{nm}/(A_{nm} + Q(x,T,N_c))$ represents the fluorescence quantum efficiency used to describe the percentage of fluorescence radiation energy in the total absorbed laser energy.

The actual OH energy-level structure is fairly sophisticated, so an approximate model of two energy levels is often used. Under the two energy-level approximation, the average collisional quenching rate Q is expressed as [9]

$$Q = \sum_i k_{Q_i} N_i \tag{2}$$

where N_i is the number density of the colliding particle ith and k_{Q_i} is the quenching rate coefficient of the colliding molecule ith, which can be expressed as

$$k_{Q_i} = \sigma_{Q_i} \langle v_i \rangle \tag{3}$$

where σ_{Q_i} is the collisional quenching cross section of the molecule ith and $\langle v_i \rangle$ is the average heat collisional speed of the colliding species ith, expressed as

$$\langle v_i \rangle = \sqrt{\frac{8k_B T}{\pi \mu_i}} \tag{4}$$

where k_B is the Boltzmann constant and μ_i is the reduced mass of the colliding molecule ith.

As can be seen from Eq. (1), in order to determine the OH number density using observed LIF signals, it is necessary to exactly know all the factors impacting on the LIF signal, especially for the collisional quenching rate. For the premixed methane/air flame, the estimated average quantum yield is approximately 1/1000. This result shows that the effect of collisional quenching in flame is fairly strong and most of the OH radicals excited to the high energy state dissipate the absorbed laser energy in the form of non-radiative transition, such as collisional electronic quenching and VET. As a result, only a few OH radicals will release the absorbed energy to radiate fluorescence.

However, there are too many factors difficult to measure in the collisional quenching rate of OH radical in flames, including the quenching cross sections of colliding pairs, the average

heating collisional speed, and the number density of the collisional particles. It also can be seen from Eqs. (2)–(4) that it is rather difficult to determine the concentration, quenching section, and heating collisional speed of each collisional molecule accurately, because there are hundreds of species in the actual flame. Worse still, some colliding particles have the shorter life than OH radical, which leads to almost impossible to accurately determine the distributions of OH concentration in the observed location. In addition, the collisional environment of different flames varies also greatly. Even for only one kind of flame, the different working conditions will lead to a great change to the physical quantities affecting the rate of collisional quenching. Since there is little understanding about the non-radiative energy transfer processes of OH radical at present stage, it is almost impossible to measure the physical quantities, which can greatly affect the collisional quenching rate of OH radical by using the current experimental technique.

With the increasing demand for the spatial resolution of the internal structure of flame in the fields of combustion and aerodynamics, it is urgent to obtain the spatial distribution information for the combustion/flow fields, so as to further understand the basic characteristics of the chemical reaction in flames. PLIF is a laser diagnostic technique developed under this requirement, which is the expansion of LIF technology in two-dimensional space.

The physical process of PLIF is exactly the same as the LIF technology. The difference between PLIF and LIF is that the PLIF technique uses a special sheet-forming optics to replace the "line beam" used in the LIF by a "sheet beam." And the photomultiplier tube commonly used in LIF technology is replaced by an intensified charge-coupled device (ICCD) camera, which can make two-dimensional imaging for the weak fluorescence signal. The typical PLIF measuring system consists of five parts: the laser, the sheet-forming optics, the imaging acquisition and data storage, the digital delay control, and combustion systems, as shown in **Figure 2**.

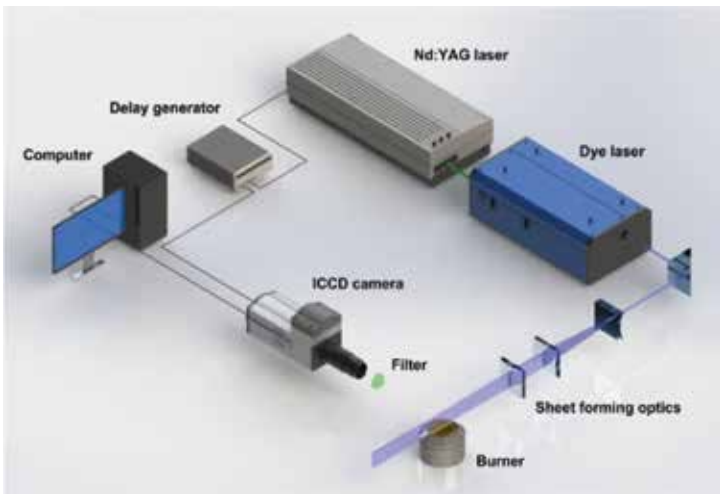

Figure 2. Typical PLIF experimental setup.

The laser source is usually composed of pump laser and dye laser to obtain a laser beam with different excitation wavelengths. The sheet-forming optics mainly consists of one cylindrical concave lens and other two vertical cylindrical convex lenses, achieving the transformation from line beam to sheet beam. The imaging acquisition and data storage system is mainly composed of ICCD camera and data storage module to acquire the weak fluorescence signals in a real time. The digital delay control system is used to control the synchronization between the laser and the ICCD camera. The burner is used to produce an objective flame to be researched. According to the characteristics of the actual research, the PLIF system will be slightly different, but the main assembly is still composed of the above five parts.

3. Review on the developments of the quantitative LIF

From the view of using purposes, LIF technology can be briefly divided into two categories: qualitative and quantitative. In this section, the current research status of quantitative LIF will be reviewed.

3.1. Calibration LIF

From Eq. (1), it is known that the following parameters should be measured accurately when using the PLIF image to deduce the concentration field of the species: the excitation laser wavelength, the experimental calibration constant, the Einstein stimulated absorption coefficient, the Boltzmann fraction, the fluorescence quantum yield (especially for the collisional quenching rate Q), and the convolution of the laser line shape and the molecular absorption line shape. However, it is difficult to obtain the exact values of the temperature, the fluorescence quantum yield, and other parameters at the same time in flames. Therefore, the quantification of the molecular concentration field is thought to be fairly difficult. In order to simplify the difficulty of quantification, calibrating these parameters with a standard flame, named calibration LIF, has been first proposed.

Using the calibration method to determine the species concentration field, the following simplification is needed: under the condition of linear excitation, it is considered that the concentration of the molecules to be measured is only related to the LIF signal intensity, calibration constant, flame temperature, and environmental pressure but independent of other factors. To further reduce the dependence of the Boltzmann fraction on temperature, it is always necessary to select an excited line, which is not sensitive to the changes of temperature. After the above simplification, it can be considered that the species concentration has a direct proportional relationship with the LIF signal intensity.

At present, extensive research for the measurements of the OH concentration spatial distribution has been studied by using the calibration LIF/PLIF. The typical research work is introduced as follows.

Arnold et al. [10] measured the OH concentration distributions in the premixed methane/air flame at pressures of 1, 5, and 20 bar by using the calibration LIF. The calibration factor was

obtained by ultraviolet (UV) absorption spectroscopy. Jalbert [11] researched the variations of OH concentration with the flame heights in the premixed methane/air and hydrogen/air flames. And the influences of the equivalent ratio and flow rate on the OH concentration have also been investigated by using the calibration LIF.

Although the calibration LIF has ability to measure the species concentration profiles to a certain extent, there is more serious problem that should not be neglected: the calibration LIF ignores the fact that the collisional quenching rates vary with the spatial position in the flame. Therefore, the calibration LIF cannot be considered as a real quantitative LIF strictly. It can only be regarded as a semiquantitative LIF technology.

3.2. Saturated LIF

When the excited energy density is higher than the threshold energy density of saturation excitation, the intensity of fluorescence signal is only related to the molecular number density, stimulated absorption, stimulated radiation, and spontaneous radiation but independent with excitation energy and the electronic quenching rate. This case is known as the saturated LIF.

In the saturated LIF, the measured fluorescence signal can directly reflect the number density of the stimulated molecules. The main drawback of the saturated LIF is that the output laser pulse is difficult to reach the required saturated excitation energy density. Therefore, it is difficult to achieve the planar concentration measurement for the species. In addition, because the laser pulse has a certain energy profile in time and space, it is easy to arise the so-called wing effect at the edge of energy profile. In other words, the laser energy density at the edge is less than the threshold energy density. Therefore, the excitation in this location still belongs to the linear excitation, leading to the fact that fluorescence signal is still affected by the collisional quenching effect. The researches on quantitative measurement of species concentration using saturated LIF mainly include:

Carter et al. [12] used saturated LIF to measure the OH concentration distributions in $C_2H_6/O_2/N_2$ flames under the high pressure. The experimental results indicate that the maximum OH concentration measured by saturated LIF is 1.10×10^{16}, 1.05×10^{16}, 1.18×10^{16} and 0.98×10^{16} molecules/cm^3, respectively, under the pressure of 0.98, 6.1, 9.2, and 12.3 atm.

Kohse-Höinghaus et al. [13] measured the concentrations of CH and OH radicals in a premixed C_2H_2/O_2 flames under the low pressure using saturation LIF. The experimental results show that the concentration of CH and OH radicals in acetylene/oxygen flame is 1.1×10^{13} cm^{-3} ($T = 1750 \pm 80$ K, height at 2.6 mm) and 8.9×10^{14} cm^{-3} ($T = 2000 \pm 100$ K, height at 7.5 mm), respectively, under the pressure of 13 mbar and the equivalence ratio of 1.2.

3.3. Laser-induced pre-dissociative fluorescence (LIPF)

LIPF has also been recognized a kind of quantitative LIF, which is proposed to solve the problem that the fluorescence signal is susceptible to collisional quenching effect in linear LIF. In the LIPF, the fluorescence quantum efficiency can be written as

$$\varphi = \frac{A_{nm}}{A_{nm} + Q(T, N_c) + P} \tag{5}$$

where P represents the pre-dissociative rates of the molecules in the excited state.

Generally speaking, if the ground state molecules can be excited to a suitable upper level, then there is a relationship of $Q \ll P$. Taking the vibrational band (3,0) excitation of OH radical as an example, the typical spontaneous emission rate A in the upper level is approximately 1.6×10^4 s^{-1}, the collision quenching rate is about 10^9 s^{-1}, and the pre-dissociative rate is around at 1×10^{10} s^{-1}. Therefore, the effects of A and Q on the fluorescence quantum efficiency can be neglected. In the LIPF, it can be considered that the fluorescence quantum efficiency is only affected by the pre-dissociative effect, but has no obvious relevance with the spontaneous emission and the collisional quenching effects. If the calibration factor of LIF signal would be obtained by other methods (calibration or direct measurement), the measured molecular concentration in flames can be obtained by using this quantitative relationship.

Using LIPF to measure the concentration fields of the stimulated molecules can immunize the LIF signal from the interference of collision quenching effect and thus reduce the difficulty for the quantitative measurements. However, it will bring in another trouble that the higher dissociative rate will lead to the decrease of fluorescence quantum efficiency, which makes the fluorescence signal further weakened and difficult to capture. In addition, compared with the traditional linear LIF excitation wavelength, LIPF usually needs to excite the measured species to a higher excitation level. At the same time, the energy density of excitation laser should also be increased as high as possible, so as to meet a higher SNR requirement. These experimental conditions are rather incompetent for the common lasers. The researches on the quantitative concentration measurements using LIPF mainly include:

Yuan et al. [14] quantitatively measured the variations of the OH concentrations with the axial heights in a premixed methane/air and propane/air flat flames at the range of 1–5 atm and the equivalence ratio of 0.7–1.3. The experimental results indicate that the OH concentration in the methane/air flame reaches the peak at around 2 mm from the burner surface, with a numerical value of about 1.1×10^{16} molecules/cm^3. For propane/air flame, the peak OH concentration on the same conditions is much smaller than that of methane/air flames, with a value of about 1.5×10^{15} molecules/cm^3.

Brown et al. [15] measured the OH concentration profiles in a hydrogen/air diffusion flame using the LIPF and compared the experimental results with the numerical simulations. The experimental results show that the peak concentration of OH radical is 9.3×10^{16} molecules/cm^3 approximately in this flame.

3.4. Short-duration pulsed LIF

In the linear LIF, the duration of the excitation laser pulse (pulse width) is at the order of nanosecond, and the collision quenching rate is commonly 10^9–10^{10} s^{-1}, slightly less than the excited laser pulse width, while the fluorescence lifetime of the excited state molecules is around at a few nanoseconds. Therefore, if the nanosecond laser pulse is used to excite the molecules, and then the fluorescence emitted from excited molecules is collected by an ICCD camera with a

gate width of nanosecond, the detected fluorescence signals are bound to be seriously affected by the influence of electronic quenching effect. Nevertheless, if the picosecond or a shorter laser pulse is considered to use, the molecules will be distributed in the upper energy state before the collisional quenching occurs. In this moment, if the picosecond detector can be employed to collect the fluorescence emitting from the molecule, the fluorescence signal will no longer be influenced by the collisional quenching effect. This is known as the short-duration pulsed LIF.

Thus, the short-duration pulsed LIF is also a kind of quantitative LIF, which is independent of the collisional quenching effect. The shortcoming of short-duration pulsed LIF lies in the fact that it is difficult to output a laser beam with a pulse width of picosecond, and the gate width of ICCD camera is not easy to reach at the order of picosecond. Furthermore, as the laser pulse width and the gate width of the detector are all at the order of picosecond, the collected fluorescence signals will be relatively weak, and its SNR is extraordinary low, which are not convenient for practical engineering applications. The researches on quantitative measurements of species concentration using short-duration pulsed LIF mainly include:

Bormann et al. [16] used the single-pulse picosecond LIF to obtain the relative OH concentration profiles in a premixed stoichiometric CH_4/O_2 flame under the normal pressure. The experimental results indicate that the number of OH is exceedingly few in the preheating zone above the burner outlet. Most of the OH radicals are distributed near the flame front and the edge of the flame.

Brockhinke et al. [17] measured the OH concentration distributions in the hydrogen/air opposed diffusion flame using picosecond LIF and determined the concentration distributions of H atoms by three-photon LIF in the same flame. The experimental results suggest that the peak OH concentration is about 2.5×10^{16} molecules/cm^3 and the peak concentration of the H atom is around at 2.1×10^{16} molecules/cm^3 in the stagnation surface of diffusion flame.

3.5. Bidirectional LIF

Bidirectional LIF has been recognized as a non-calibration linear LIF, which is independent of the collisional quenching effect. In the bidirectional LIF, the number density of the stimulated molecules is only related to the effective peak absorption cross section of the measured molecules and the forward and backward fluorescence signals. It has no relevance with the collisional quenching effect, the calibration constant of the detection system, and the energy density of the excited laser. Using bidirectional LIF/PLIF to map the concentration distributions, the two laser beams (or sheet beams) propagating through flame in the opposite direction are required to excite the molecules in the flame, so as to obtain the forward and backward LIF/PLIF signals. With combining the effective peak absorption cross sections of the molecules by other measurement methods, the number density of the excited molecules can then be obtained.

The available literature shows that the embryonic form of the bidirectional LIF is first proposed by the Stepowski [18]. After that, Versluis et al. [8] have further developed it and given a more concise and explicit expression for the concentration measurements in the high absorptive flames. The first application of bidirectional LIF/PLIF to the quantification of the two-dimensional OH concentration distributions in a methane/oxygen torch flame is investigated by Versluis et al. Besides that, Brackmann et al. [19] also employed bidirectional LIF to achieve

the quantitative measurements of OH concentration distributions in an opposed diffusion flame. Because the opposed diffusion flame belongs to a kind of symmetrical flame, they used only one beam to excite the OH radicals and combined the mirror symmetry method to achieve the quantitative measurements of one-dimensional OH concentration distributions. Their experimental results indicate that the OH concentration is about 7.8×10^{15} molecules/cm^3 at the height of 1.8 mm from the burner nozzle. In addition, Tian et al. [20] also used bidirectional LIF to quantitatively measure the concentration of iron atoms in a premixed laminar propylene/oxygen/argon flat flames. However, the two opposite directional beams have not been employed in their experiments. Instead, the mirror symmetry method has been used to obtain the variations of the iron atom concentration with the axial heights.

Judging from the existing literature statistics, the current species concentration measurements based on bidirectional LIF/PLIF technology are still fairly scarce. Although the bidirectional LIF/PLIF has great advantages beyond other quantitative LIF/PLIF technologies, such as no collisional quenching effect, no special excitation conditions (e.g., large energy, short pulses, etc.) and no additional calibration, it has a high requirement for the spatial coincidence of the beams and the SNR of the fluorescence signal. In addition, the experimental expression of effective peak absorption cross section provided by Versluis et al. has a limitation, which is not applicable to the case of weak absorption. In view of this problem, we have supplemented and corrected the experimental measurement equation in this chapter. These difficulties have resulted in the fact that the research of species concentration measurement based on the bidirectional PLIF is almost at a standstill. Therefore, it is necessary to conduct the in-depth research in order to promote the further development of the bidirectional LIF/PLIF.

4. The fundamental theory of bidirectional LIF

4.1. Measurement equation of the species concentration profiles

A schematic of one-dimensional bidirectional LIF for molecular concentration measurement is shown in **Figure 3**. First we give a definition as described in the following. With ICCD camera for reference, the direction in which the laser beam traverses the flame from left to right is the backward direction, instead of reverse for the forward direction. The points $x = 0$ and $x = L$ denote the boundaries for the concentration calculation.

The laser-induced fluorescence signal intensity at the point x is given by the following expression:

$$F_b(x) = CS(x)\sigma_0 N(x) I_b(x) \tag{6}$$

where C is a constant depending on the collection angle of fluorescence signal and the detector sensitivity, $S(x)$ denotes the fluorescent quantum yield which is only dependent on the spontaneous emission rate and the collisional quenching rate $Q(x)$, σ_0 is the effective peak absorption cross section of molecules to be measured, and $N(x)$ represents the particle number density at point x. Consider a laser beam propagating through the flame at a fixed height from left to right along the x-axis in **Figure 1**. The beam will be attenuated according to the Lambert-Beer law, and the intensity is given by the following equation:

http://dx.doi.org/10.5772/intechopen.79702

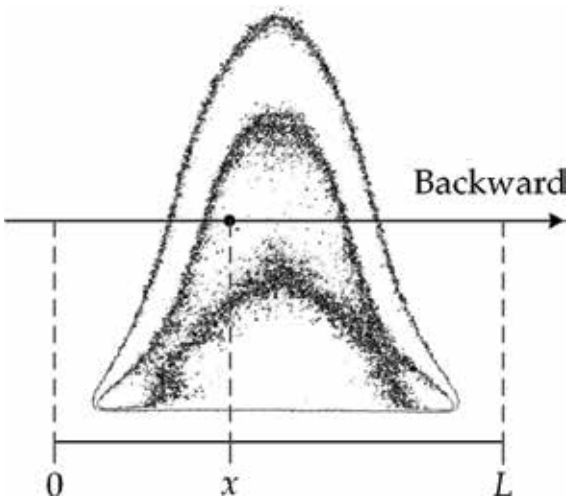

Figure 3. Schematic diagram for one-dimensional bidirectional LIF method.

$$I_b(x) = I_{b,0} e^{-\int_0^x \sigma_0 N(x) dy} \tag{7}$$

Eq. (7) is established in the unsaturated condition. In Eq. (7), $I_b(x)$ is the laser intensity in the backward direction at point x, and $I_{b,0}$ is the initial laser intensity of the backward beam at point $x = 0$. Similarly, if the laser propagates in the opposite direction from right to left, at the same height, the forward equation of the laser beam is given as

$$F_f(x) = CS(x)\sigma_0 N(x) I_f(x) \tag{8}$$

$$I_f(x) = I_{f,0} e^{-\int_0^x \sigma_0 N(x) dy} \tag{9}$$

where $I_f(x)$ is the laser intensity in the forward direction at point x and $I_{f,0}$ is the initial laser intensity of the forward beam. Note that the incident point of the forward beam is located at $x = L$. The ratio of fluorescence signals, $R(x)$, is equal to the ratio between the laser intensities because the factors of C, i.e., $S(x)$, σ_0, and $N(x)$, are canceled in the division expressed as

$$R(x) = \frac{F_f(x)}{F_b(x)} = \frac{I_f(x)}{I_b(x)} \tag{10}$$

Take the logarithm of the fluorescence ratio $R(x)$; then one will obtain the following equation:

$$\begin{aligned} \ln[R(x)] &= \ln\left[\frac{I_f(x)}{I_b(x)}\right] \\ &= \ln\frac{I_{f,0}}{I_{b,0}} + \int_0^x \sigma_0 N(y) dy - \int_x^L \sigma_0 N(y) dy \\ &= \ln\frac{I_{f,0}}{I_{b,0}} + 2\int_0^x \sigma_0 N(y) dy - \int_0^L \sigma_0 N(y) dy \end{aligned} \tag{11}$$

Finally taking the differential operation on Eq. (11), one can obtain

$$\mathrm{N}(x) = \frac{1}{2\sigma_0}\frac{\mathrm{d}}{\mathrm{d}x}\ln\left[\frac{F_f(x)}{F_b(x)}\right] \tag{12}$$

which is a measurement equation of the species concentration profiles, representing the quantitative functional relationship between particle number density and LIF fluorescence intensity. Eq. (12) clearly shows that the particle number density is only associated with the forward and backward fluorescence intensities and the effective peak absorption cross section of particles under the linear excitation, independent of the temperature, pressure, quenching rate, laser energy, etc. It also suggests that the derivative of the fluorescence ratio $R(x)$ is very sensitive to noise in the LIF signal.

It is important to note that the $N(x)$ in Eq. (12) refers to the molecular number density in the excited level for the low rotational level J''. However, the total number density of the molecules to be measured N_0 is often concerned in the experiments. Therefore, it needs to be converted to N_0 after obtaining the experimental value of $N(x)$. In the state of thermal equilibrium, the relationship between the number density $N(v, J'', T)$ in the excited molecule and the total number density N_0 of the molecules is linked by the Boltzmann fraction $f_B(v, J'', T)$, and the mathematical expression is given as follows:

$$f_B(v, J'', T) = \frac{N(v, J'', T)}{N_0} = \frac{(2J''+1)}{Q_{vib}Q_{rot}Q_{elec}}e^{-(E_{vib}+E_{rot})/k_BT} \tag{13}$$

where k_B is the Boltzmann constant; T is the temperature; the vibrational quantum number J'' represents the rotational quantum number at the low energy level; E_vib and E_rot are vibrational and rotational energies, respectively; and Q_vib, Q_rot, and Q_elec are vibrational, rotational, and electronic partition functions, respectively.

Overall, the bidirectional LIF/PLIF is thought to be a no-calibration and no quenching effect LIF/PLIF technique, based on the combination of the traditional linear LIF/PLIF and absorption spectroscopy. It not only preserves the advantages of high spatial resolution of traditional LIF/PLIF but also absorbs the superiority of no quenching effect from absorption spectroscopy. It is of great significance to solve the problem of traditional quantitative LIF/PLIF technology.

4.2. Effective peak absorption cross section

From the view of the quantum mechanics, the absorption cross section describes the probability that the incident photon is absorbed by the target nucleus, and its unit usually has the dimension of area (cm^2). When the laser propagating along the x direction passes through the medium, the molecules will be attenuated by absorption, following the Lambert Bill absorption law. The differential form is expressed as

$$\frac{1}{I_{\overline{\nu}}(x)}\frac{dI_{\overline{\nu}}(x)}{dx} = -N(x)\sigma(\overline{\nu})P \tag{14}$$

where $I\overline{v}(x)$ is the intensity of laser at x point, ν represents the wave number (cm^{-1}), P is the pressure (atm), $N(x)$ denotes the number density (cm^{-3}) of the excited molecules at the point x, and $\sigma(\overline{v})$ is the absorption cross section (cm^2) of the molecules. Eq. (14) is thought to be the phenomenological physical definition of the absorption cross section.

As long as the laser energy is not too high and the molecular number density is not too large, the absorption cross section can be considered directly proportional to the linear absorption function (cm) [21]:

$$\sigma(\overline{\nu}) = \sigma_{tot} g(\overline{\nu}) \tag{15}$$

where σ_{tot} is the integral absorption cross section (cm) and the line-shape function satisfies the normalization condition:

$$\int_{-\infty}^{\infty} g(\overline{\nu}) d\overline{\nu} = 1 \tag{16}$$

To integrate Eq. (15), one can obtain

$$\sigma_{tot} = \int_{-\infty}^{\infty} \sigma(\overline{\nu}) d\overline{\nu} \tag{17}$$

It can be seen that σ_{tot} is only related to the nature of the molecule but has no relationship with external environmental conditions. The integral absorption cross section is directly related to the oscillator strength of the molecule, with the expression of [22]

$$\sigma_{tot} = \frac{\pi e^2}{m_e c^2} f_{v'v''J'J''} \tag{18}$$

where e is the electronic charge (esu), m_e is the mass of electron (g), c is the speed of light (cm/s), and $f_{v'v''J'J''}$ is the molecular oscillator strength in the given oscillator transition, expressing as [23]

$$f_{v'v''J'J''} = \frac{f_{v'v''}(v', v'')}{4} \frac{S_{J'J''}}{2J'' + 1} T_{J'J''} \tag{19}$$

where v'' is the vibrational quantum number in the upper vibrational energy level; J'' is the vibrational quantum number in the lower vibrational level; is the vibrator strength, $S_{J'J''}$ is the rotational transition probability, that is, the Honl-London factor; and $T_{J'J''}$ represents the vibrational and rotational correction factor. The detailed values of $f_{v'v''J'J''}$, $S_{J'J''}$ and $T_{J'J''}$ can be found in the LIFBASE software.

In the actual experiment, the measured absorption line shape is not normalized, and thus

$$\int_{-\infty}^{\infty} \phi(\overline{\nu}) d\overline{\nu} \neq 1 \tag{20}$$

For this reason, it is necessary to normalize it for obtaining the experimental expression of the effective peak absorption cross section.

The integral on the left side of Eq. (15) is defined as the relative integral absorption area *Int*. Normalizing above integral, one will obtain

$$\int_{-\infty}^{\infty} \frac{\phi(\overline{\nu})}{Int} d\overline{\nu} = \int_{-\infty}^{\infty} g(\overline{\nu}) d\overline{\nu} = 1 \tag{21}$$

Meanwhile, it is noted that if the first-term integral of Eq. (21) is multiplied on the left side of Eq. (17), one will get

$$\int_{-\infty}^{\infty} \sigma(\overline{\nu}) d\overline{\nu} = \sigma_{\text{tot}} \int_{-\infty}^{\infty} \frac{\phi(\overline{\nu})}{Int} d\overline{\nu} \tag{22}$$

That is

$$\sigma(\overline{\nu}) = \frac{\sigma_{\text{tot}} \phi(\overline{\nu})}{Int} \tag{23}$$

Eq. (23) is the relationship between the absorption cross section and the molecular absorption line profile measured experimentally.

In particular, if $\overline{\nu} = \overline{\nu}_0$, then

$$\sigma_0 = \sigma(\overline{\nu}_0) = \frac{\sigma_{\text{tot}} \phi(\overline{\nu}_0)}{Int} \tag{24}$$

where σ_0 is the effective peak absorption cross section; the numerical value of σ_{tot} can be calculated by Eq. (18). Eq. (24) is thought to be the experimental expression for measuring the effective peak absorption cross section of the molecule. Eq. (24) indicates that the effective peak absorption cross section of the molecule is related to the molecular absorption line shape and the relative integral absorption area.

As Versluis et al. have not clearly pointed out that the effective peak absorption cross section associates with the peak value $\phi(\overline{\nu}_0)$ of absorption line-shape, there is a difference between the effective peak absorption cross section and the actual value, if using the measurement equation given by Versluis et al. The difference is not obvious for the absorption band (0,0) of OH radical. However, this discrepancy will manifest significantly for the weak absorption band of (1,0). Therefore, the measurement equation of effective peak absorption cross section given by Versluis et al. is not applicable to the condition of weak absorption. To solve this problem, we revised the experimental equation. The corrected effective peak absorption cross section measurement equation is shown in Eq. (24). To confirm the validity of the modified measurement equation, the effective peak absorption cross section of the band (0,0) and band (1,0) within the $Q_1(8)$ line for the OH radical is measured, respectively. The experimental results show that the OH effective peak absorption cross section of the $Q_1(8)$ line for band (0,0) turns out to be about 5.5 times higher than that of band (1,0), while the theoretical calculation given by the LIFBASE simulation is about 6 times. The experimental result has been proven to be in good agreement with the simulation results.

5. Concentration profiles in a laminar flame by bidirectional PLIF

5.1. Measurements for the absolute OH concentration profiles in a partially premixed methane/air flat flame

The temperature distribution of $CH_4/O_2/N_2$ partially premixed flame is first measured by UV absorption spectrometry. The average temperature of the premixed flame of methane/air is 1772 K, with the statistical uncertainty of ±10.4%. Then, the axial distributions of OH effective peak absorption cross section for $Q_1(8)$ line (the corresponding wavelength of 309.240 nm) in the band (0,0) are determined by using the wavelength scanning method. The statistical average of the OH effective peak absorption cross section on the axial direction is 1.10×10^{-15} cm^2 with the relative statistical uncertainty, which is ±9.9%. The standard flat flame burner, designed by Hartung et al. [24], in the experiments is employed. More detailed experimental parameters can be found in the literature [25]. The variations of two-dimensional OH concentration fields with the equivalence ratios Φ (from 0.7 to 1.4) have been obtained in $CH_4/O_2/N_2$ partially premixed flat flame by using bidirectional PLIF, as shown in **Figures 4** and **5**.

Figures 4 and **5** show the two-dimensional spatial distributions of OH concentration in the methane/air partially premixed flame and its variations with the equivalence ratios, respectively. The actual size of each image is 15 mm × 46 mm, and the spatial resolution is 87.6 μm.

As can be seen from **Figure 4**, when the flame is burned in the lean-burn condition, the OH radicals are mainly distributed in a narrow band above the burner surface. With the increase of the axial distance, the OH concentration will decrease rapidly. On the other hand, the OH

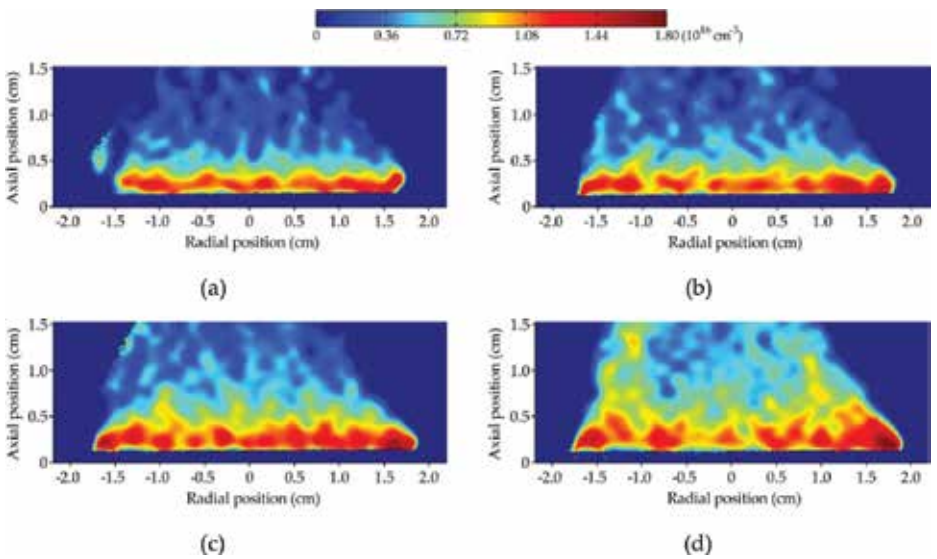

Figure 4. Variations of two-dimensional OH concentrations with equivalence ratios (Φ = 0.7–1.0). (a) Φ = 0.7, (b) Φ = 0.8, (c) Φ = 0.9, (d) Φ = 1.0.

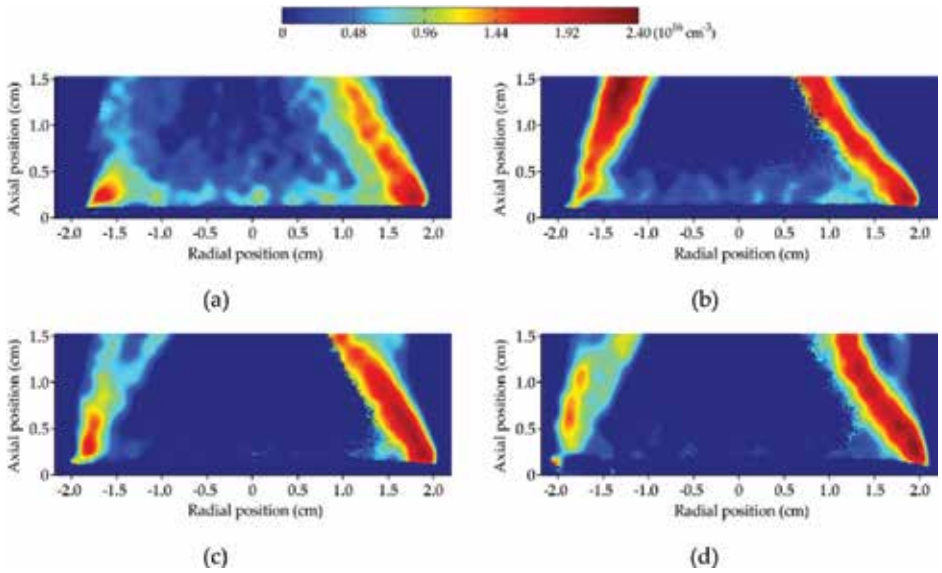

Figure 5. Variations of two-dimensional OH concentrations with equivalence ratios (Φ = 1.1–1.4). (a) Φ = 1.1, (b) Φ = 1.2, (c) Φ = 1.3, (d) Φ = 1.4.

radical group gradually moves toward both sides of the flame, and the amount of OH radicals in the middle region is decreasing gradually with the increase of the equivalence ratio from 0.7 to 1. When the flame is burning at the rich-burn condition, as shown in **Figure 5**, the OH concentration profiles have changed greatly. That is, as the equivalence ratio continues to increase from 1.1 to 1.4, the two strong OH radical bands are formed on both sides of the flame. Meanwhile, the OH radical density in the middle region of flame decreases sharply.

5.2. Comparison between numerical simulation and experimental results

The comparison between the numerical simulations and the experimental results in the methane/air laminar partially premixed flame under different equivalence ratios is shown in **Figure 6**. The values of red translucency are the total uncertainties of the corresponding measured points.

From **Figure 6**, we can draw the following three conclusions:

1. In the range of equivalence ratio 0.7–1.2, the calculated results and the experimental values have the same variation trend with increasing the axial distance above the burner. The OH concentration increases rapidly to the maximum and then gradually decreases with the increase of axial distance, remaining unchanged at last. However, the experimental OH concentrations in the burnout zone decrease faster than the calculated results under certain equivalence ratios (e.g., equivalence ratios 0.8 and 0.9). The reason for this phenomenon mainly lies in the fact that the temperature results given by the GRI-Mech 3.0 mechanism are basically kept unchanged in this region, while the experimental temperature will decrease with increasing the axial distance.

http://dx.doi.org/10.5772/intechopen.79702

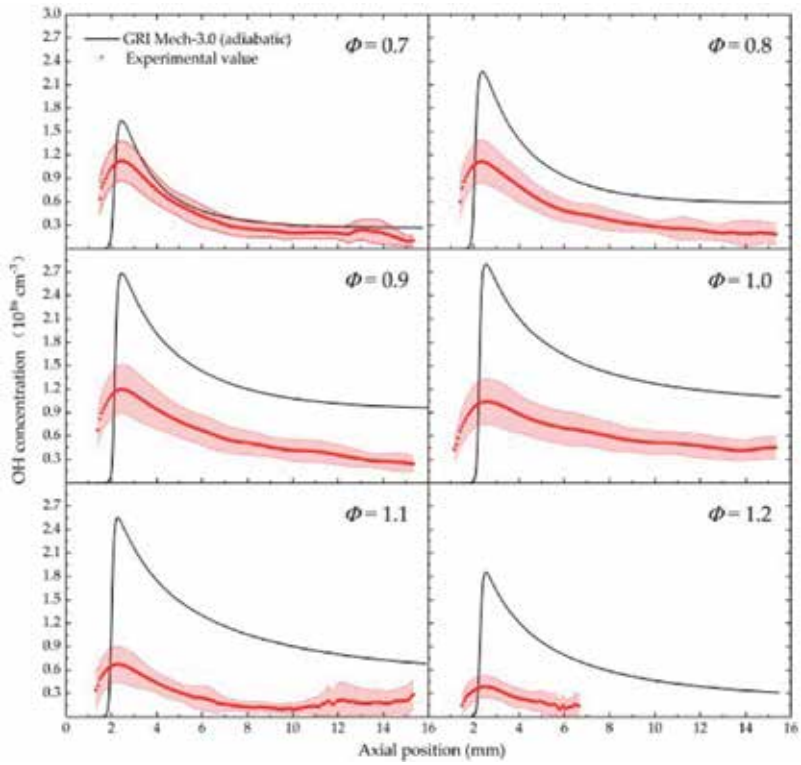

Figure 6. Comparison between experimental and numerical results of OH concentration in the central axis.

2. In the range of equivalence ratio 0.7–1.2, the calculated OH concentration is generally higher than the experimental values. It is not difficult to find that the OH concentration profiles based on the GRI-Mech 3.0 mechanism is in good agreement with the experimental variation trend only when the equivalent ratio equals to 0.7. The reason for the above difference may lie in the fact that the simulation gives the OH concentration distribution in the adiabatic state, but the actual flame is in a nonadiabatic state, and it is unavoidable to have some radiation loss. Therefore, the experimental measurement results of the OH concentrations are found to be always smaller than the corresponding calculation results. A rough calculation shows that the calculated temperature considering the radiation loss is about 150–250 K lower than that without taking into account the thermal radiation loss.

3. In the range of equivalence ratio 0.7–1.2, it is found that the OH concentration increases rapidly from zero to the maximum value. The experimental results indicate that the change speed of OH concentration is not as large as the calculated result and the measured OH concentrations are higher than the calculation results at the same axial position. It is presumed that the main reason for this phenomenon lies in the following: the width of the chemical reaction zone is rather narrow (about 1–2 mm) in the methane/air flat flame. When the flame reaches the stable combustion state, a large amount of heat will flow toward the burner surface and thus increase the flame temperature. Therefore, the temperature of the premixed gas inside the burner will be increased accordingly. As a consequence, the temperature of the

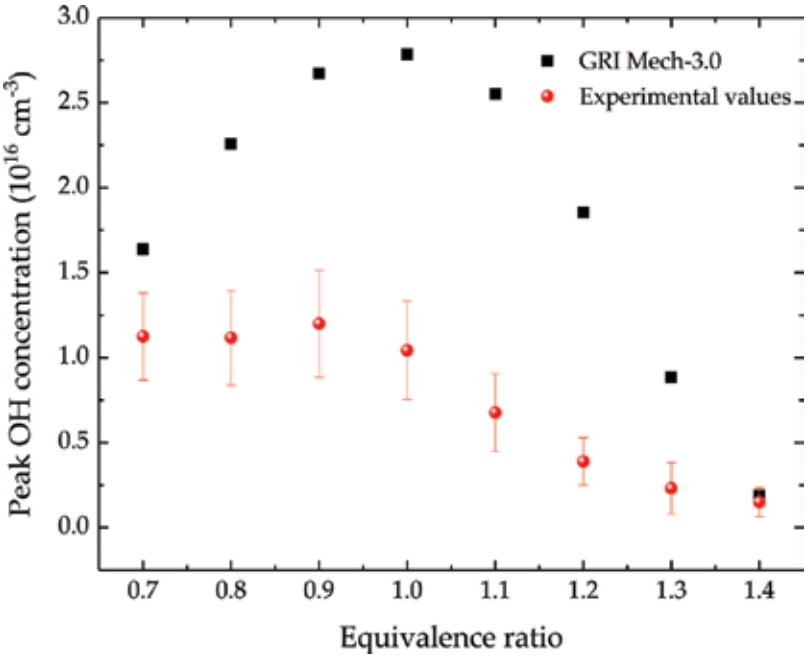

Figure 7. Comparison between experimental data and numerical simulation of peak OH concentration.

premixed gas will rise rapidly after flowing out from the burner and produce the chemical reaction, resulting in generating a large number of OH radicals. However, the temperature rising process of the premixed gas has not been taken into account in the numerical simulation. On the contrary, it is considered that the gas temperature near the outlet of burner is still in an ideal unheated state. Therefore, the measured OH concentrations are higher than the calculation results in the upstream of reaction zone.

The comparison results for the peak concentration under the conditions of different equivalence ratios have also been made, as shown in **Figure 7**. It can be clearly seen that the experimental results are smaller than the calculated values. The reason has already been analyzed before, so it is no longer mentioned here. Another notable phenomenon is that the measured OH concentration has not reached the maximum under the equivalent ratio of 1.0, but the peak OH concentration occurs in the lean-burn zone under the equivalence ratio of 0.9. The above experimental result indicates that even if the equivalence ratio of the premixed gas is set to 1.0, the fuel molecules still cannot be completely consumed in the actual combustion process. Therefore, we speculate that the OH reaction rate predicted by the simulation may be higher than the experimental value under the condition of stoichiometric ratio.

6. Conclusions

In conclusion, this chapter first reviews the developments of planar laser-induced fluorescence and briefly analyzes the existing problems of quantitative PLIF technology. Then, the advantages

and disadvantages of current quantitative PLIF technologies for species concentration measurements in flames are reviewed. And the latest works on the quantification of species concentration using PLIF in combustion are introduced. Thirdly, a non-calibration quantitative PLIF technology, named bidirectional PLIF, which is independent of collisional quenching effect, has been introduced in detail. As the current measurement equation of effective peak absorption cross section provided by Versluis et al. is found to be not applicable to the case of weak absorption, the revised experimental equation has been proposed in this chapter. At last, the two-dimensional spatial distributions of OH concentration and its variations with the equivalence ratios have been investigated in the methane/air partially premixed flame. The comparison between the experimental OH concentrations and the numerical simulation results has also been made under the equivalence ratios of 0.7–1.4. The result indicates that the OH concentration profiles measured by bidirectional PLIF are in good agreement with the predictive values performed by GRI-Mech 3.0 mechanism.

Acknowledgements

This research is financially supported by the National Key Scientific Instrument and Equipment Development Projects of China (No. 2012YQ040164) and the National Natural Science Foundation of China (Grant Nos. 61275127 and 91441130). The author would like to thank Prof. Xin Yu, Dr. Jiangbo Peng, and A/Prof. Jianlong Zhang et al. for providing many valuable insights and numerous help.

Author details

Zhen Yang[1,2,3]*, Xin Yu[1,2], Jiangbo Peng[1,2] and Jianlong Zhang[3]

*Address all correspondence to: sailoryz@163.com

1 National Key Laboratory of Science and Technology on Tunable Laser, Harbin Institute of Technology, Harbin, China

2 Institute of Opto-Electronics, Harbin Institute of Technology, Harbin, China

3 Institute of Optical Target Simulation and Test Technology, Harbin Institute of Technology, Harbin, China

References

[1] Hanson RK. Planar laser-induced fluorescence imaging. Journal of Quantitative Spectroscopy and Radiative Transfer. 1988;**40**(3):343-362. DOI: 10.1016/0022-4073(88)90125-2

[2] Xavier P, Vandel A, Godard G, et al. Investigation of combustion dynamics in a cavity-based combustor with high-speed laser diagnostics. Experiments in Fluids. 2016;**57**:50. DOI: 10.1007/s00348-016-2135-7

[3] Elbaz AM, Roberts WL. Experimental study of the inverse diffusion flame using high repetition rate OH/acetone PLIF and PIV. Fuel. 2016;**165**:447-461. DOI: 10.1007/s00348-016-2135-7

[4] Giezendanner-Thoben R, Meier U, Meier W, et al. Phase-locked two-line OH planar laser-induced fluorescence thermometry in a pulsating gas turbine model combustor at atmospheric pressure. Applied Optics. 2005;**44**(31):6565-6577. DOI: 10.1364/AO.44.006565

[5] Seitzman JM, Hanson RK, DeBarber PA, et al. Application of quantitative two-line OH planar laser-induced fluorescence for temporally resolved planar thermometry in reacting flows. Applied Optics. 1994;**33**(18):4000-4012. DOI: 10.1364/AO.33.004000

[6] Luque J, Jeffries JB, Smith GP, et al. Quasi-simultaneous detection of CH_2O and CH by cavity ring-down absorption and laser-induced fluorescence in a methane/air low-pressure flame. Applied Physics B. 2001;**73**(7):731-738. DOI: 10.1007/s003400100649

[7] Luque J, Berg PA, Jeffries JB, et al. Cavity ring-down absorption and laser-induced fluorescence for quantitative measurements of CH radicals in low-pressure flames. Applied Physics B. 2004;**78**(1):93-102. DOI: 10.1007/s00340-003-1331-3

[8] Versluis M, Georgiev N, Martinsson L, et al. 2-D absolute OH concentration profiles in atmospheric flames using planar LIF in a bi-directional laser beam configuration. Applied Physics B. 1997;**65**(3):411-417. DOI: 10.1007/s003400050289

[9] Ehn A. Towards quantitative diagnostics using short-pulse laser techniques [thesis]. Lund: Lund University; 2012

[10] Arnold A, Bombach R, Käppeli B, et al. Quantitative measurements of OH concentration fields by two-dimensional laser-induced fluorescence. Applied Physics B. 1997;**64**(5):579-583. DOI: 10.1007/s003400050218

[11] Jalbert AM. A study of quantitative concentrations of hydroxyl (OH) in laminar flat flames using planar laser induced fluorescence (PLIF) [thesis]. Boston: Northeastern University; 2011

[12] Carter CD, King GB, Laurendeau NM. Saturated fluorescence measurements of the hydroxyl radical in laminar high-pressure $C_2H_6/O_2/N_2$ flames. Applied Optics. 1992; **31**(10):1511-1522. DOI: 10.1364/AO.31.001511

[13] Kohse-Höinghaus K, Heidenreich R, Just T. Determination of absolute OH and CH concentrations in a low pressure flame by laser-induced saturated fluorescence. Symposium on Combustion. 1985;**20**(1):1177-1185. DOI: 10.1016/S0082-0784(85)80606-8

[14] Yuan TH, Lai YH, Lu CJ, et al. Universal calibration of quantitative OH-LIPF measurements in hydrocarbon flames at elevated pressures. Combustion, Explosion, and Shock Waves. 2009;**45**(4):404-412. DOI: 10.1007/s10573-009-0050-4

[15] Brown TM, Tanoff MA, Osborne RJ, et al. Experimental and numerical investigation of laminar hydrogen-air counterflow diffusion flames. Combustion Science and Technology. 1997;**129**(1-6):71-88. DOI: 10.1080/00102209708935720

[16] Bormann F, Nielsen T, Burrows M, et al. Single-pulse collision-insensitive picosecond planar laser-induced fluorescence of OH $A^2\Sigma^+$ (v'=2) in atmospheric-pressure flames. Applied Physics B. 1996;**62**(6):601-607. DOI: 10.1007/BF01081698

[17] Brockhinke A, Bülter A, Rolon JC, et al. Ps-LIF measurements of minor species concentration in a counterflow diffusion flame interacting with a vortex. Applied Physics B. 2001; **72**(4):491-496. DOI: 10.1007/s003400100535

[18] Stepowski D. Local absorption measurement by laser-induced fluorescence. Applied Optics. 1987;**26**(9):1631-1635. DOI: 10.1364/AO.26.001631

[19] Brackmann C, Bood J, Aldén M, et al. Quantitative measurements of species and temperature in a DME-air counterflow diffusion flame using laser diagnostic methods. Combustion Science and Technology. 2006;**178**(6):1165-1184. DOI: 10.1080/00102200600582376

[20] Tian K, Li ZS, Staude S, et al. Influence of ferrocene dddition to a laminar premixed propene flame: Laser diagnostics, mass spectrometry and numerical simulations. Proceedings of the Combustion Institute. 2009;**32**(1):445-452. DOI: 10.1016/j.proci.2008.05.056

[21] Hilborn RC. Einstein coefficients, cross sections, *f* values, dipole moments, and all that. American Journal of Physics. 2002;**50**(11):982-986. DOI: 10.1119/1.12937

[22] McGee TJ, Mcilrath TJ. Absolute OH absorption cross sections (for lidar measurements). Journal of Quantitative Spectroscopy and Radiative Transfer. 1984;**32**(2):179-184. DOI: 10.1016/0022-4073(84)90082-7

[23] Anketell J, Pery-Thorne A. Oscillator strengths in the $^2\Sigma^+ \rightarrow 2\Pi$ dand system of OH by the hook method. Proceedings of the Royal Society A. 1967;**301**(1466):343-353. DOI: 10.1098/rspa.1967.0212

[24] Hartung G, Hult J, Kaminski CF. A flat flame burner for the calibration of laser thermometry techniques. Measurement Science and Technology. 2006;**17**(9):2485-2493. DOI: 10.1088/0957-0233/17/9/016

[25] Zhen Y, Xin Y, Peng J, et al. Quantitative measurements of one-dimensional OH absolute concentration profiles in a methane/air flat flame by bi-directional laser-induced fluorescence. Chinese Physics B. 2015;**24**(11):114204. DOI: 10.1088/1674-1056/24/11/114204

Chapter 6

Indirect Diode Laser in the Treatment of Retinopathy of Prematurity

Simona Delia Nicoară

Additional information is available at the end of the chapter

http://dx.doi.org/10.5772/intechopen.79828

Abstract

Retinopathy of prematurity (ROP) is a largely preventable cause of visual impairment in children. The golden standard of treatment in ROP is the laser photocoagulation of the non-vascularized retina. The most vulnerable period when ROP is at high risk of rapid progression is comprised between 34 and 35 weeks postconceptional age (PCA) and 36–37 weeks PCA. We carried out a retrospective study in which we included all the ROP cases treated by indirect diode laser photocoagulation between January 1, 2006, and December 31, 2017, totalizing 110 premature infants of which, 60 were males (54.54%) and 50, females (45.45%). Mean gestational age (GA) was 28.30 weeks and mean birth weight (BW) was 1121 grams in our series. Of the 110 preterm infants, 74 were the result of single pregnancies (67.27%) and 36 of multiple pregnancies (32.72%). At the moment of treatment, the mean postnatal age (PNA) was 8.38 weeks and the mean PCA, 37.02 weeks. ROP regressed after laser treatment in 185 eyes (88.09%). Statistical tests proved that regression rate was significantly worse in aggressive posterior ROP as compared with stage 3 zone 2 and stage 3 zone 1 ROP (odds ratio = 13.53, relative risk = 7.79, $P < .001$).

Keywords: retinopathy of prematurity, pediatric blindness, indirect diode laser, ROP treatment, ROP outcome

1. Introduction

Retinopathy of prematurity (ROP) can be a major cause of pediatric blindness worldwide if not diagnosed and treated promptly [1]. Visual loss in ROP is due to the complications related to retinal ischemia: retinal neovascularization, vitreous hemorrhage and finally total retinal detachment. Fortunately, ROP is a largely preventable cause of visual impairment in children. Despite the fact that in recent years, intravitreal anti-VEGF agents proved their efficacy and safety in the

management of ROP, the golden standard of treatment in ROP remains the laser photocoagulation of the non-vascularized retina [1].

2. Indirect diode laser photocoagulation in the treatment of ROP

In order to understand the rationale of laser treatment in ROP and its mechanism of action, the pathogenesis of ROP is summarized, as well as its classification and indications for treatment. Practical considerations on indirect diode laser photocoagulation for ROP are presented subsequently.

2.1. Pathogenesis of ROP

Vasculogenesis and *angiogenesis* are two distinct terms that need to be explained. In the vasculogenesis process, the origin of blood vessels is represented by the endothelial progenitor cells that coalesce and form lumen and vasculogenic networks. In the angiogenesis process, the new vessels form from the existing ones by vascular sprouting [2].

ROP is a biphasic disease directly related to the saturation of oxygen, which is administered in order to maintain the prematurely born vital functions. Phase 1 (between 22 and 30 weeks PCA) is characterized by relative hyperoxia and decreased vascular endothelial growth factors (VEGF) levels. The consequence of this situation is delayed vessel formation. Phase 2 (between 31 and 44 weeks PCA) is defined by relative hypoxia and increased VEGF levels, having as consequence uncontrolled vessel growth.

The cause of ROP is the non-development of retinal vessels with subsequent retinal ischemia and new vessel proliferation [2].

2.2. ROP classification

Screening for ROP is essential for reducing the blindness rate related to this disease [3]. It should be made by indirect ophthalmoscopy by specially trained ophthalmologists according to criteria which are specific to each country/region.

In classifying ROP, the following criteria are used: zone, stage and the presence/absence of "plus" disease. The retina is divided into three zones and 12 clock hours. Zone 1 corresponds to a circle having the radius equal to the double distance between the optic disc and the fovea. Zone 2 describes a circle with the radius that equals the distance between the optic disc and the nasal ora serrata. Zone 3 is the remaining "crescent" of retina in the temporal area [3, 4].

Stages are defined according to the modifications at the limit between the vascularized and non-vascularized retina. Stage 0 reflects no modification at this level, but the retinal vascularization is not yet completed. In stage 1, a demarcation line (within the retinal plane) is identified at this site. In stage 2, there is a non-vascularized, white ridge (elevated from the retinal plane) at the limit between the two retinal regions, and in stage 3, the ridge is vascularized, red. Stage 4a corresponds to peripheral retinal detachment. In stage 4b, the fovea is also detached, and in stage 5, there is total retinal detachment in an open or closed funnel [3, 4].

"Plus" disease includes retinal vessel dilation and tortuosity, retinal hemorrhages and pupil rigidity [3, 4].

Separately from the features of the "classic" ROP described above, aggressive posterior ROP (AP-ROP) has been described with the following aspects: very severe "plus" disease, posterior location (most commonly zone 1, but also posterior zone 2), ill-defined or no ridge, rapid progression to stage 5 ROP [3, 4].

Also, there are two important terms that have to be defined: threshold and pre-threshold ROP. Threshold ROP includes: stage 3, zone 1 or 2, with "plus" disease, with a ridge extending on more than five contiguous or eight cumulative clock hours. Pre-threshold ROP includes the following situations: less than threshold ROP in zone 1/stage 2, zone 2 with "plus"/stage 3, zone 2, without "plus"/stage 3 with "plus," less extended than threshold ROP [3, 4].

2.3. Laser effect

Understanding laser technology starts from the translation of the word LASER: light amplification by the stimulated emission of radiation.

Atoms occupy various energetic levels. Lower energetic levels are associated with higher stability. If the atom absorbs energy under the shape of a photon, it "jumps" on a higher energetic level in a state of excitation. The excited atom can "fall" back spontaneously on the lower energetic level by emitting a photon. The excited atom can be "forced" to fall from the higher on the lower energetic level if it meets a photon carrying the energy equal to the difference between the two levels. This process is called stimulated emission: a photon stimulates the emission of another photon [5].

If we would be able to bring the majority of atoms on the superior energetic level, the incident radiation will induce the emission of a more intense beam than the incident one. This is called radiation amplifying. The key problem is to obtain a state with more atoms on the superior energetic level, which is called population inversion and is reached by pumping. In order to amplify the light, the system is closed between two parallel mirrors forming a cavity. The mirrors allow photons to jump back and forth by continuously reflecting between them, thus producing stimulated emissions. When the radiation flux becomes extremely intense, it is allowed to get out of the cavity as laser beam [5].

The abovementioned principles explain the key properties of the laser radiation:

1. Because the photons are emitted through energies that are liberated between two well-defined energetic levels, the radiation is *monochromatic.*
2. Because the two mirrors are parallel, the laser beam is composed of highly parallel rays: *limited divergence.*
3. The emitted and the "disruptive" radiations are always in the same phase; therefore, the laser radiation is *coherent.*

These properties offer theoretical advantages to the laser radiation over the white light that are translated by its clinical applications in various ocular diseases [5].

Monochromatic laser light allows the specific selection of a wavelength that is going to be absorbed by a specific pigment in the eye according to the ocular condition.

Also there is no chromatic aberration allowing the obtainment of a small retinal impact.

Laser light is much more intense, which makes it possible to use low energies to obtain a clinical effect with a significantly lower risk for complications.

Parallelism allows the obtainment of small retinal lesions in the periphery.

Therapeutic energy can be pre-selected by the ophthalmologist according to the effect on the retina: lower energies are used initially which are progressively increased, up to the moment where the desired effect is obtained [5].

2.4. Laser retinal photocoagulation

Clinical effects of laser photocoagulation are obtained by thermal reaction. When the temperature in the tissue reaches a critical level, proteins are denatured and coagulation occurs. The factors that influence the results of coagulation for a certain power are: the energy of a specified wavelength, the spot size and the exposure time. According to the degree of coagulation, ocular reaction manifests by cell proliferation, cell migration, and scar formation [5].

Tissue effects of lasers depend upon the interaction between the laser wavelength and ocular pigments: melanin, hemoglobin and xanthophyll.

Melanin is found in the RPE as melanosomes and in the choroid as granules. The maximum absorption of melanin is for wavelengths of 400–600 nm, followed by blue, green, red and infrared. Subsequently, shorter wavelengths are better absorbed by melanin as compared to longer ones. When it comes to the penetration through tissues of the laser radiation, longer wavelengths will manifest their effect deep in the choroid. Because the quantity of melanin varies between individuals and from one region to another of the fundus, the coagulation effect of longer wavelengths is unequal. Longer wavelengths require higher energies to obtain similar effects with the shorter ones.

Hemoglobin is more selective in terms of absorption. Its maximum absorption is for blue, green and yellow wavelengths, whereas for red and infrared, there is no absorption.

Xanthophyll pigment is located exclusively in the fovea, and it absorbs the blue and blue-green laser radiations. Because of the damaging effects on the central vision of these radiations, they are no longer used in the clinical practice [5].

Lasers that create thermal reactions have direct and indirect effects on the ocular tissues.

In ischemic retinopathies, such as ROP, the indirect effect is used to induce the regression of new vessels that appear due to retinal ischemia.

Several mechanisms of action have been described. It is postulated that tissue destruction by laser photocoagulation decreases the need for oxygen of the tissues, and in the same time, it lowers the stimulus for the production of angiogenic factor.

http://dx.doi.org/10.5772/intechopen.79828

Photocoagulation also eliminates the photoreceptor cells, which are high oxygen consumers, allowing the use of available oxygen by the viable cells.

A tight adhesion between the retina and choriocapillaris is created following laser photocoagulation, increasing oxygen flow to the retina.

The pigmented cells destroyed by laser liberate a substance that inhibits angiogenesis [5].

2.5. Technical characteristics of the indirect diode laser

Diode laser has an infrared emission (810 nm), and it cools in the environment and has a life span of 30,000 h. The transmission optic system is very simple: it is constituted by mirrors leading the laser beam from the slit lamp to the patient's retina. When attached to the indirect ophthalmoscope, such as in the ROP treatment, this role is taken by a system of fiber optics.

The laser fiber is connected from the laser to the indirect ophthalmoscope, and the laser impacts are delivered by acting on a pedal, which is also connected to the laser. The console allows the operator to choose the adequate parameters of the laser impact: dimension, exposure time and power. The operator wears the helmet throughout the treatment and moves his head in order to deliver the light from the indirect ophthalmoscope and the laser beam into the infant's eye (**Figure 1**).

Figure 1. Indirect diode laser.

Figure 2. Delivery of the laser treatment.

The delivery mode is chosen: repeat at various intervals/single impact and the number of impacts is counted. The repeat mode is preferred because when pressing the pedal once, a series of impacts is delivered on the retina, at time intervals that are selected by the operator. However, this more rapid modality of treatment is chosen by the experienced surgeons. The retina is visualized with a +20 or +28 diopter lens and the peripheral retina is reached by the help of a scleral indentor (**Figure 2**).

2.6. Parameters used during the laser retinal photocoagulation

The clinical effect of laser photocoagulation on the retina depends on two main parameters: power and exposure time. If low power is used, higher exposure time is required. On the contrary, at high power, a low exposure time is sufficient to obtain a significant retinal reaction [5].

2.6.1. Power

Power is the parameter that influences the most the photocoagulation effect. Selecting a certain power is relative, as it depends on individual factors: retinal pigmentation, edema, pre-retinal fibrosis, the presence of vitreous hemorrhage. Therefore, the key element in choosing a certain laser power is clinical (retinal reaction), not technical (mW). Usually, treatment is initiated with low powers (150–200 mW) in order to test retinal reaction, never on pigmented retina. If there is no visible mark, power is increased with 20–50 mW, until the obtainment of the desired effect: whitish lesion. When high powers are used, the lesion appears gray with well-defined margins and sometimes in its center a vapor stream is emitted. This effect can be identified when passing from a thicker to a thinner retina, for example from the posterior pole toward the periphery, without reducing the power accordingly. During retinal photocoagulation, power must be varied in order to obtain the appropriate tissue reaction [5].

2.6.2. Exposure time

Exposure time can vary between 50 ms and 1 s. At low exposure times, the effect in the tissue is cylindrical: the area of the lesion is the same at the superficial (RPE) and deep (choroid) levels.

However, at low exposure times, high powers are required in order to obtain a clinical effect. This is associated with the risk of explosive effects. Usually, exposure times between 200 and 500 ms are preferred [5].

2.6.3. Dimension of the laser spot

When laser energy is delivered through the indirect ophthalmoscope, the dimension of the laser spot effectively arriving on the retina is the result of the distance between the helmet (the site where the laser fiber is fixed) and the retina [5].

2.6.4. Number of the laser spots

The number of laser spots is correlated with the area of nonvascular retina. Practically, all the surface of non-vascular retina should be destroyed by laser. By consequence, more the disease is posterior, more laser spots are needed. ROP represents an instance in which all photocoagulation must be completed in one session due to its rapid progression. The number of laser spots may vary between 1000 and 5000/eye [5].

2.6.5. Evolution of laser impacts

At the moment of application, the laser marks should be whitish. During the next days, they become less net because of the inflammatory reaction, which is proportional to the extension of treatment. Within 1–2 weeks, the impacts develop pigment in the central area surrounded by atrophy. The extension of scars at the fovea in posterior ROP may induce significant loss of vision [5].

2.7. Rationale for laser use in the treatment of ROP

The premature retina is incompletely developed and when exposed to high levels of oxygen which is necessary for life support, a relative hyperoxic environment is created, leading to the decrease of VEGF and subsequent delay or even cessation in the development of retinal vessels. By consequence, the retinal tissue does not get enough oxygen (relative hypoxia) and synthesizes angiogenic factor with the development of new vessels at the limit between the vascular and nonvascular retina.

The rationale of laser use in ROP is to destroy the nonvascular retina, which is the source of new vessels, thus interrupting the pathogenic chain ultimately leading to vision loss.

Cryotherapy was used before laser to destroy the nonvascular retina, and its results were first published in 1988 by the Cryo-ROP Study proving its efficacy in preventing ROP-related blindness [6].

A few years later, in 1994, the Laser Study Group demonstrated the laser was as effective as cryotherapy in preventing blindness produced by ROP and with less severe side effects. Besides the fact that it causes less trauma and manipulation on the globe as compared to cryotherapy, laser was more effective in zone 1 and zone 2 disease [2, 7].

2.8. Indications for laser treatment in ROP

The indications for ROP treatment were formulated for the first time by the Multicenter Trial of Cryotherapy for ROP, as a threshold disease [6].

The Early Treatment for ROP Randomized Trial Study affirmed that the criteria for treatment defined as "threshold" may no longer be the ideal indication for treatment. Therefore, the criteria for "pre-threshold" ROP were defined with the recommendation to initiate treatment also in these circumstances. The results of treatment in the pre-threshold ROP were significantly better than the threshold ones [2, 8, 9].

2.9. Timing of laser treatment for ROP

ROP is a model of acute retinal ischemia that is self-limiting, but if not addressed urgently, it may lead rapidly to retinal detachment and loss of vision. Because the window of opportunity during which laser treatment is likely to have a positive result is very short, timely recognition is crucial for a good outcome [7, 8]. Therefore, active screening should be carried out according to very precise criteria [3].

Basically, treatment should be performed at the point in the natural history of the disease when neovascularization can be reversed because once vitreo-retinal traction is initiated, the disease can no longer be controlled [2]. Therefore, knowing the correlation between the evolution of ROP and time is crucial for a correct screening.

The most vulnerable period, when ROP is at high risk of rapid progression starts at 34–35 weeks PCA up to 36–37 weeks PCA [8]. Usually, ROP does not develop during the first 2 weeks of life. The median age for the detection of stage 1 ROP is 34 weeks PCA, pre-threshold ROP appears around 36 weeks PCA and threshold ROP at about 37 weeks PCA. The vascularization of the retina is completed by 40–44 weeks PCA.

In conclusion, the interval for ROP detection is between 32 and 40 weeks PCA, but the critical phase, during which ROP may progress rapidly and has to be treated, is between 34 and 37 weeks PCA [7].

2.10. Indirect diode laser photocoagulation for ROP

Laser therapies are carried out in the Neonatology Units, under sedation. Prior laser treatment, pupil dilation is achieved with a mixture of tropicamide 0.5% and phenylephrine 2.5%. The eyes are maintained open with a lid speculum throughout the procedure, the retina is visualized with a +20 or +28 diopter lens and the peripheral retina is accessed with a scleral indentor.

Diode laser has an infrared emission of 810 nm, which is delivered transpupillary. Usually, the following laser parameters are used: 200 microns laser spot, with 200 ms duration and power between 100 and 300 mW, according to the retinal reaction. Laser spots are applied on all the surface of the non-vascular retina, from the anterior margin of the ridge to the ora serrata, in a confluent manner, with no space between them.

Adverse events related to laser treatment were cited in the literature: anterior uveitis, cataract, vitreous hemorrhage, retinal detachment [7]. Anterior uveitis was rarely identified in cases that required extensive laser photocoagulation, such as aggressive posterior-ROP [2]. The risk of cataract development is very low, especially when using the infrared laser which is absorbed deep into the choroid and not in the crystalline lens [2, 7]. Vitreous hemorrhage and retinal detachment represent rather a failure of laser to stop ROP progression than a complication by itself [2].

2.11. Advantages of indirect laser photocoagulation over cryotherapy for ROP treatment

Cryotherapy was the first method that stopped the progression of ROP toward blindness [6]. The rationale was to destroy the non-vascular retina by applications of cryo on the sclera.

Indirect laser photocoagulation of the retina proved to be as effective as cryo in preventing ROP-related blindness, but with significantly fewer side effects. The pressure exerted by the cryoprobe on the infants' sclera was associated with high risk of myopia. Cryotherapy itself is more laborious than laser and requires more time and general anesthesia. By consequence, more anesthesia-related incidents were reported during cryo as compared to laser. In posterior ROP, it is very difficult (sometimes impossible) to reach the retina in the posterior pole with the cryoprobe. Therefore, posterior non-vascular retina may remain untreated with a high risk of ROP progression.

For all these reasons, currently indirect laser photocoagulation replaced cryotherapy in the treatment of ROP in most of settings.

ROP offers an eloquent example in which laser energy has revolutionized the treatment of an extremely serious disease, with significant socioeconomic and life quality positive impact.

3. Personal experience in the treatment of ROP with indirect diode laser

3.1. Setting

This study was carried out at the "Iuliu Hatieganu" University of Medicine and Pharmacy (Cluj-Napoca, Romania) in the Ophthalmology and Neonatology Departments. All laser therapies were performed by two ophthalmologists in the Neonatology Department. Before enrollment in the study, informed consent was obtained from the parents/tutors. The study is approved by the Ethical Committee of "Iuliu Hatieganu" University of Medicine and Pharmacy.

3.2. Study sample

This study includes all the consecutive premature infants with ROP who required laser photocoagulation between January 1, 2006 and December 31, 2017. The screening protocol was based on the following criteria: GA less or equal to 33 weeks and, BW less or equal to 1500 g.

Premature infants beyond these criteria were also included in the screening if other risk factors were associated: prolonged oxygen administration with saturation over 93%, repeated transfusions, sepsis and the need of more than 6 days of mechanical ventilation for cardiorespiratory support. Eyes with stage 2 zone 2, stage 4a, 4b and 5 were not treated by laser and were therefore not included in the study sample.

3.3. Medical intervention

We performed laser therapy in the following situations: stage 3 zone 1 ROP, stage 3 zone 2 ROP, stage 2 zone 1 ROP and AP-ROP. Infants with AP-ROP were treated within 24 h from diagnosis and the rest of them within 48 h from diagnosis.

All laser therapies were carried out under sedation in the Neonatology Unit. We used a portable indirect diode laser, with an emission of 810 nm, and laser energy was delivered transpupillary (**Figure 1**).

A mixture of tropicamide 0.5% and phenylephrine 2.5% was instilled preoperatively, in order to dilate the pupils. In order to gain access to the retina, a lid speculum, a sclera indentor and a + 28 diopter lens were used (**Figure 2**).

Indirect diode laser photocoagulation was performed with the following parameters: 200 microns laser spot, 200 ms duration and 150–300 mW power, according to the retinal reaction. The obtaining of a whitish retinal spot was aimed. Laser spots were applied in a confluent manner, with no space between impacts, to cover all the surface of the non-vascular retina, up to ora serrata. The number of impacts varied between 1500 and 4000/eye.

The first postlaser review took place 7 days after treatment. In case of regression, examinations continued every 5–6 days, until there was clear evidence of ROP regression. In case of regression failure, laser was completed immediately. The treated eyes were monitored with a frequency dictated by the clinical course of the disease, in order to address any risk of sequel.

3.4. Statistical analysis

Epi Info 7 software (Centers for Disease Control and Prevention, Atlanta, GA) was used for the statistical analysis of the data. Frequencies for the following independent variables concerning the premature infant were calculated: gender, GA, BW, type of pregnancy (unique or multiple), PCA and PNA at treatment, ROP classification.

Odds ratio was used to interpret the results, and statistical significance was evaluated according to P value calculated with t test. Chi-square test was used if values over 5 were expected in 80% of the table cells, and Fisher exact test was used if values under 5 were expected in more than 20% of the table cells. P values less than .05 were considered statistically significant.

3.5. Results

In the previously mentioned period, we treated by indirect diode laser photocoagulation 110 premature infants of which, 60 were males (54.54%) and 50 were females (45.45%).

Of these, 35 were from Cluj (31.81%) and 75 came from neighboring departments where laser was unavailable (68.18%).

GA was between 24 and 33 weeks (mean ± standard deviation: 28.30 ± 2.87 weeks) and BW was between 500 and 1700 g (mean ± standard deviation: 1121 ± 280.45 g).

Of the 110 preterm infants, 74 were the result of single pregnancies (67.27%) and 36 of multiple pregnancies (32.72%).

PNA at treatment was between 5 and 13 weeks (mean: 8.38 ± 1.93 weeks) and PCA at treatment was between 32 and 41 weeks (mean: 37.02 ± 1.65 weeks).

The data are summarized in **Table 1**.

Retinal laser photocoagulation was bilateral in 100 cases and unilateral in 10 cases, which makes for 210 lasered eyes. The 10 eyes in which laser photocoagulation was not performed fall into one of the following categories: stage 1 zone 2 ROP (four eyes), stage 2 zone 2 ROP (three eyes), stage 4a ROP (one eye), stage 5 ROP (one eye) and congenital atrophy (one eye). The three eyes with stage 2 zone 2 ROP were followed up closely, every 3 days and they regressed spontaneously with no need for laser therapy. ROP classification of the lasered eyes is as follows: stage 3 zone 2 ROP—167 eyes (79.52%), stage 3 zone 1 ROP—30 eyes (14.28%), AP-ROP—13 eyes (6.19%).

ROP regressed after laser treatment in 185 eyes (88.09%). Of the 185 eyes, regression was achieved after one laser session in 175 eyes (94.59%) and after two laser sessions in 10 eyes (5.40%). In all ROP cases with stage 3 zone 2 disease, regression was obtained after one laser

Characteristic	No
Gender	
Male	60 (54.54%)
Female	50 (45.45%)
City of origin	
Cluj	35 (31.81%)
Outside Cluj	75 (68.18%)
Type of pregnancy	
Single	74 (67.27%)
Multiple	36 (32.72%)
Mean ± SD gestational age (wk)	28.30 ± 2.87
Mean ± birth weight (g)	1121 ± 280.45
Mean ± SD PNA at treatment (wk)	8.38 ± 1.93
Mean ± SD PCA at treatment (wk)	37.02 ± 1

SD, standard deviation; PNA, postnatal age; PCA, postconceptional age.

Table 1. Premature infants treated by indirect diode laser photocoagulation for ROP.

session. In stage 3 zone 1 ROP cases, regression was achieved after one laser session in 26 eyes, whereas in four eyes, two laser sessions were required to stabilize the disease. In AP-ROP cases, two laser sessions were necessary in 6 of the 13 eyes. Statistical tests proved that regression rate was significantly worse in AP-ROP eyes as compared with stage 3 zone 2 and stage 3 zone 1 ROP (odds ratio = 13.53, relative risk = 7.79, $P < .001$).

Within the group of 25 eyes in which ROP failed to regress, 14 belonged to the male gender (56%) and 11 to the female gender (44%). The difference is not statistically significant.

The type of pregnancy (single or multiple) did not influence the outcome: ROP regressed in 132 of the 149 treated eyes coming from single pregnancies (88.59%) and in 53 of the 61 eyes coming from multiple pregnancies (86.88%).

Macular dragging was identified in three eyes, all from the AP-ROP group. Complications related to laser treatment were represented by two cases of mild anterior uveitis that responded promptly to mydriatic and anti-inflammatory eye drops.

We evaluated the timing of the laser treatment according to two parameters: PNA and PCA at treatment. Treatment was performed at PNA of 8 weeks or less in 118 eyes (56.19%) and at PNA of more than 8 weeks in 92 eyes (43.80%). Within the first group, ROP regressed in 101 eyes (85.59%), and within the second group, ROP regressed in 84 eyes (91.30%). According to the chi-square test, the difference is not statistically significant. PCA at treatment was equal or less than 37 weeks in 123 eyes (58.57%) and more than 37 weeks in 87 eyes (41.42%). Within the first group, ROP regressed in 112 eyes (91.05%), and within the second group, ROP regressed in 78 eyes (89.65%). This difference is not statistically significant, according to the chi-square test.

Within the group of 210 treated eyes, 84 belonged to premature infants with BW equal to or less than 1000 g (40%) and 126 eyes (60%), to premature infants with BW of more than 1000 g. ROP failed to regress in nine eyes from the first group (10.71%) and in 16 eyes from the second group (12.69%). The statistical tests proved that the difference is not significant.

GA was 28 weeks or less in 116 eyes (55.23%) and more than 28 weeks in 94 eyes (44.76%). Within the first group, ROP regressed after laser treatment in 104 eyes (89.65%) and in the second group ROP regressed in 81 eyes (86.17%). The difference is not statistically significant.

3.6. Discussion

The premature infants in our series who needed laser for the treatment of ROP had higher BW (1121 g) and older gestational ages (28 weeks) than their counterparts in the United States (830 g BW average and 26 weeks GA average). The oldest treated infant was born at 33 weeks PCA and the heaviest treated infant was 1700 g, both beyond the screening criteria in the United States. The practical impact of this observation is that each country/region has to apply its own screening criteria for ROP. If criteria from the USA or from Western Europe had been applied, many ROP cases had been lost with subsequent visual loss.

Because of the short window of opportunity during which the laser is effective, timely recognition of the disease is crucial for the positive result of the treatment. In our series, PCA and

PNA at treatment were not statistically significantly different between the favorable outcome and unfavorable outcome groups.

Indirect diode laser photocoagulation proved its efficacy in ROP treatment. Our ROP regression rate is comparable to the ones cited in the literature [7]. The laser spots were applied on all the surface of the nonvascular retina, from the anterior margin of the ridge (when identifiable) up to ora serrata. In six eyes, we also placed laser posterior to the ridge for two reasons: to limit the extension of traction toward the posterior pole and to destroy an area, which is known to provide high levels of vasoproliferative factors because it is ischemic. We used this approach only in situations with advanced stage 3 disease in which we identified traction on the retina. All the six eyes had a good outcome (ROP regressed with no anatomical sequelae). Not all authors approve this strategy, arguing that it destroys more of the peripheral visual field with no proven benefit [2].

We delivered laser energy transpupillary in all cases. Laser can also be delivered through the sclera. In terms of efficacy, the two delivery methods are similar, but the transscleral approach is more traumatic. According to some authors, the transscleral approach carries no risk of cataract formation. However, in our series, we identified no case of cataract after laser delivered transpupillary. This is logic, taking into account that the absorption site of the infrared radiation is deep into the choroid, passing through the crystalline lens without being absorbed.

Literature shows that lower GA and BW are associated with poorer outcomes of ROP [6]. These observations could not be verified in our series in which statistical tests proved no significant difference in terms of outcome according to GA and BW.

Our study proves that the only factor with significant impact on ROP prognosis following laser was the ROP type. As such, AP-ROP cases had a significantly worse outcome as compared to the so-called classic ROP ones, which is in agreement with results cited in the literature [10]. The disappointing results that we obtained in AP-ROP cases with laser photocoagulation motivated us to start treatment in these cases with intravitreal Bevacizumab. This attitude significantly improved our results.

4. Conclusion

Indirect diode laser photocoagulation of the non-vascular retina is a major tool in preventing ROP-related blindness. In order for the laser treatment to be effective, proper screening and timely recognition of ROP are crucial. Intravitreal anti-VEGF injections improved the outcome of laser treatment in severe forms of the disease, but laser remains the golden standard in the treatment of ROP.

Acknowledgements

This study was funded by grant number PED 156, Executive Agency for Higher Education, Research, Development and Innovation Funding, Romania.

Conflict of interest

The author declares no conflict of interest related to the publication of this chapter.

Author details

Simona Delia Nicoară

Address all correspondence to: simonanicoara1@gmail.com

Faculty of Medicine, Department of Ophthalmology, "Iuliu Haţieganu" University of Medicine and Pharmacy, Cluj-Napoca, Romania

References

[1] Nicoară SD, Ştefănuţ AC, Nascutzy C, Zaharie GC, Toader LE, Drugan TC. Regression rates following the treatment of aggressive posterior retinopathy of prematurity with bevacizumab versus laser: 8-year retrospective analysis. Medical Science Monitor. 2016;**22**:1192-1209. DOI: 10;22:1192-209

[2] Nicoara SD, Cristian C, Irimescu I, Stefanut AC, Zaharie G. Diode laser photocoagulation for retinopathy of prematurity: Outcomes after 7 years of treatment. Journal of Pediatric Ophthalmology and Strabismus. 2014;**51**(1):39-45. DOI: 10.3928/01913913-20131112-02

[3] O'Keefe M, Kirwan C. Screening for retinopathy of prematurity. Early Human Development. 2008;**84**(2):89-94. DOI: 10.1016/j.earlhumdev.2007.11.006

[4] International Committee for the Classification of Retinopathy of Prematurity. The international classification of retinopathy of prematurity revisited. Archives of Ophthalmology. 2005;**123**(7):991-999. DOI: 10.1001/archopht.123.7.991

[5] Nicoara SD. Laser treatment in ocular diseases. In: Dumitrache M, editor. Surgical and laser treatment of ocular diseases. Bucharest: "Carol Davila" Universitary Medical Publishing House; 2014. pp. 419-486. ISBN: 978-973-708-741-6

[6] Cryotherapy for Retinopathy of Prematurity Cooperative Group. Multicenter trial of cryotherapy for retinopathy of prematurity: Preliminary results. Archives of Ophthalmology. 1988;**106**(4):471-479. DOI: 10.1001/archopht.1988.01060130517027

[7] Kieselbach GF, Ramharter A, Baldissera I, Kralinger MT. Laser photocoagulation for retinopathy of prematurity: Structural and functional outcome. Acta Ophthalmologica Scandinavica. 2006;**84**(1):21-26. DOI: 10.1111/j.1600-0420.2005.00548.x

[8] Soh Y, Fujino T, Hatsukawa Y. Progression and timing of treatment of zone in retinopathy of prematurity. American Journal of Ophthalmology. 2008;**146**(3):369-374. DOI: 10.1016/j.ajo.2008.05.010

[9] Shah PK, Prabhu V, Karandikar SS, Ranjan R, Narendran V, Kalpana N. Retinopathy of prematurity: Past, present and future. World Journal of Clinical Pediatrics. 2016;**5**(1):35-46. DOI: 10.5409/wjcp.v5.i1.35

[10] Drenser KA, Trese MT, Capone A Jr. Aggressive posterior retinopathy of prematurity. Retina. 2010;**30**(suppl):S37-S40. DOI: 10.1097/IAE.0b013e3181cb6151

Edited by Yufei Ma

The laser has become more and more important in scientific research and industrial applications. Now, the laser wavelength can cover the range from ultraviolet to terahertz and output laser performance has significantly progressed in recent years. This book is focused on the advanced diode laser, fiber laser, and their applications in laser ablation, laser-introduced fluorescence, and laser treatment. The advantages of laser technology are shown comprehensively.

Published in London, UK

IntechOpen

ISBN 978-1-83881-817-3
9 781838 818173